THE MOLECULAR DETERMINANTS OF SYNAPTIC CURRENT KINETICS AT ZEBRAFISH NEUROMUSCULAR JUNCTIONS

By

Rebecca A. Mongeon

A Dissertation

Presented to

the Program in Neuroscience

and

Oregon Health and Science University
School of Medicine

in partial fulfillment of the requirements for the degree of

Doctor of Philosophy

November 2010

School of Medicine

Oregon Health and Science University

We, the dissertation committee, hereby certify that the Ph.D. dissertation of

Rebecca A. Mongeon

has been approved

_____

Gail Mandel, Ph.D., Senior Scientist, Dissertation Advisor
Vollum Institute for Advanced Biomedical Research

_____

John Adelman, Ph.D., Senior Scientist, Dissertation Chairman
Vollum Institute for Advanced Biomedical Research

_____

Paul Brehm, Ph.D., Senior Scientist
Vollum Institute for Advanced Biomedical Research

_____

David Dawson, Ph.D., Professor and Chair
Department of Physiology and Pharmacology

_____

Claudio Grosman, Ph.D., Associate Professor
Department of Molecular and Integrative Physiology
University of Illinois at Urbana-Champaign

To Andrea

TABLE OF CONTENTS

ABSTRACT

All vertebrates share the two fundamental skeletal muscle types, termed fast and slow muscle, which have evolved distinct functions to meet different motor demands. Fast muscle generates an action potential in response to neural input and contracts rapidly. Slow tonic muscle is inexcitable, and depends on the depolarization derived from synaptic input for contraction. For more than 50 years it has been known that slow muscle exhibits synaptic currents that decay 5-fold slower than currents in fast muscle, but the mechanism responsible for this difference is not known. Two hypotheses have been proposed that could account for the difference in current decay; differences in acetylcholine clearance rate in the synaptic cleft, or differences in acetylcholine receptor kinetics. Zebrafish provides a tractable model system in which to test both hypotheses and resolve this long-standing question.

Synaptic current recordings from an acetylcholinesterase mutant null line of zebrafish established that transmitter clearance is not the mechanism by which differences in current decay are conferred. Fast muscle currents are prolonged in mutant fish, but not converted to resemble the kinetics of slow muscle. Instead, single-channel recordings from both types of muscle indicated that the difference in synaptic decay is established at the level of the acetylcholine receptor. Slow muscle expresses a receptor type that exhibits a mean burst duration 6-fold greater than that of fast muscle. To identify the structural correlates of fast and slow muscle receptors, each zebrafish

nicotinic acetylcholine receptor subunit gene was cloned and combinations of subunits were heterologously expressed for functional analysis.

Comparison of the single-channel mean burst duration, conductance and voltage-dependence of the burst duration indicated that the subunit combination αβδε could account for the native receptor found on fast muscle. The only other type of acetylcholine receptor known to express in muscle, the αβδγ isoform, was incompatible in all aspects with the characteristics of the receptor type found on slow muscle. However, the αβδ receptor isoform was similar to the slow muscle receptor in single-channel mean burst duration, voltage-dependence of the burst duration and conductance. The αβδ receptor was the only channel isoform to exhibit the inward rectification of slow muscle single-channel currents and synaptic currents. These results suggested that incorporation of the ε subunit represents the fundamental difference between the receptor isoforms of fast and slow tonic muscle, and confers the functional distinctions between them. Consistent with this idea, knockdown of the ε subunit *in vivo* was sufficient to convert the kinetics of fast muscle to resemble those of slow muscle, and resulted in compromised motility in larval fish. This is the first report to identify a physiological role for a muscle acetylcholine receptor lacking the γ and ε subunits, and a muscle channel type that has functional characteristics similar to those of neuronal nicotinic receptor types.

ACKNOWLEDGEMENTS

First, I want to express my gratitude to Paul and Gail for providing mentorship in the many different aspects of becoming a scientist. They are both excellent investigators in their respective fields and their training has provided me with an outstanding foundation in experimental biology. However, I have probably benefited most from their talent to promote the qualities in their students that will prepare them for a lifetime of success in research. I will always appreciate their openness and hard work that was required to help shape me in this way. I want to especially thank Gail for her continuous enthusiasm and support of my research interests which often took me outside of her area of expertise. I especially want to thank Paul for his patience in working with me side by side through the years and I will never forget the fun that we have had.

I'm very grateful for the friendship found with the lab members both at the Vollum Institute and Stony Brook University, who have felt more like family than co-workers. I have benefited so much from being surrounded by such a capable community of people on whom I relied continuously for advice and experimental support.

None of this work would have been possible without the support provided by my amazing family members who have always expressed their delight and encouragement in this pursuit.

Lastly, I am greatly indebted to Michael who, although always selfless, has lately given up so much to ensure that this became the document that I hoped it would be. Any success that I find in life will be his as well.

LIST OF FIGURES

PAGE

CHAPTER 1

Introduction

Voluntary movements in all vertebrates are executed by the release of acetylcholine from spinal motor neurons, leading to activation of cholinergic receptors on skeletal muscle. The evolutionary pressure to excel at a variety of complex motor tasks has brought about unique adaptations of the properties of skeletal muscle cells. The two major categories of vertebrate skeletal muscle fibers are generally referred to as tonic and twitch (for review see Hess, 1970, and Morgan and Proske, 1984). Twitch muscle cells generate tension quickly in response to neuronal activity, but are unable to maintain contraction for extended periods of time, and so relax even if neuronal activity persists. Also referred to as fast muscle in zebrafish, the twitch type represents the majority of vertebrate muscle and is responsible for movements requiring speed or force. Refinement of twitch muscle function has produced subtypes based on the rate and force of contraction that are broadly termed fast-twitch and slow-twitch. These subtypes are familiarly known as those responsible for sprinting or long-distance type running, respectively, and most muscle groups are comprised of mixtures of twitch subtypes.

Tonic muscle, also referred to as slow muscle, represents a fundamentally different type of skeletal muscle that generates tension slowly in response to neuronal activity, but is able to sustain contraction over long time periods. These muscles were

first described and remain best characterized in non-mammalian vertebrates, such as the frog, where they are involved in maintenance of posture, such as back or leg position. Mammalian tonic muscles have been primarily studied in the extraocular muscles responsible for maintenance of eye position. Otherwise only identified in the ear, the esophagus, and the larynx, the prevalence of tonic muscle is considered to be limited in mammals compared to other vertebrates. Except in fish where the two muscle types are segregated, tonic muscle cells are typically intermingled with twitch muscle cells throughout vertebrate muscle groups (Hess, 1970, Morgan and Proske, 1984).

The first study of the electrical properties of individual twitch and tonic muscle fibers was published by Kuffler and Vaughn Williams in 1953. They were following up on a report that two distinct muscle contraction types were observed in response to acetylcholine; sustained tension or rapid and reversible twitches (Sommerkamp, 1928*). Similarly, other reports indicated there were two distinct types of end-plate structures in frog skeletal muscle, (Kruger, 1949*; Hess, 1960), but there was not direct evidence linking these morphological and functional differences. Kuffler and Vaughn Williams used the newly improved microelectrode technique (Ling and Gerard, 1949) to record from individual muscle cells of both types. They determined that tonic muscle cells were distinct from twitch cells, and that the motor neurons innervating each type were also unique. Importantly, tonic muscle cells were unable to generate action potentials, and so are also distinct from fast muscle cells on the basis of membrane excitability. Finally, the

*Although these articles were originally published in German, the key results relevant to their use here have been reported by numerous citing articles in English, and I have cited them in accordance with the common interpretation.

synaptic potentials generated in tonic muscle by nerve stimulation were longer decaying than those in twitch muscle (Kuffler and Vaughn Williams, 1953a,b).

The successful implementation of voltage-clamp technique (Hodgkin et al, 1952), combined with the microelectrode recording setup, provided direct recordings of synaptic currents from twitch skeletal muscle (Takeuchi and Takeuchi, 1958, 1959). Soon after, currents were also recorded from tonic muscle (Oomura and Tomita, 1960), confirming that tonic muscle currents were more slowly decaying than those of twitch muscle.

Relationship between synaptic current and muscle function

The differences in synaptic transmission between fast and slow muscle likely aids each cell type in meeting its particular functional requirements. Fast muscle generally obtains sufficient synaptic depolarization to bring the cell membrane potential to threshold for firing an action potential. The action potential is responsible for inducing release of the intracellular calcium needed for contraction, and thus coordinates the twitch-like response to a single neuronal input. By contrast, slow muscle relies directly on the depolarization generated by the synaptic current for contraction. In this way, the degree and duration of slow muscle tension is in direct proportion to the intensity of the synaptic drive from the motor neuron (Hess, 1970, Morgan and Proske, 1984). Where examined, the synaptic events in slow muscle are more prolonged compared to those of fast muscle (Dionne and Parsons, 1978, 1981; Chiarandini and Stefani, 1979; Miledi and Uchitel, 1981; Fedorov et al, 1982; Fedorov, 1987; Uchitel and Miledi, 1987). Prolonged synaptic currents are able to discharge the membrane capacitance to a greater extent than brief currents, and therefore generate more depolarization. At developing fast muscle

synapses, prolonged synaptic currents are necessary to depolarize to levels sufficient to generate action potentials, and this activity underlies the spontaneous contraction essential for muscle maturation (Jaramillo et al, 1988). It has been proposed that the prolonged currents of slow muscle synapses are able to efficiently promote depolarization for longer periods of time and facilitate sustained contraction (Ruff and Spiegel, 1990).

Determinants of synaptic current kinetics

The electrophysiological studies of the neuromuscular synapse of fast muscle have provided a paradigm for synaptic transmission throughout the nervous system. The kinetics of synaptic currents had long been proposed to reflect the lifetime of the elementary events of which it was formed (Katz and Miledi, 1972, Anderson and Stevens, 1973). Analysis of the current fluctuations produced by application of ACh ("noise" analysis) indicated the elementary events had a discrete lifetime that was similar in duration to the decay of the synaptic current (Katz and Miledi, 1972). Of particular interest was elucidating how the kinetics of synaptic currents of fast muscle were regulated during development, where noise analysis indicated changes in the AChR event lifetime were responsible (Sakman and Brenner, 1978; Fischbach and Scheutze, 1980). With the development of the patch-clamp technique and single-channel recordings, it was possible to directly observe the lifetime of a single acetylcholine receptor (AChR) on muscle (Neher and Sakmann, 1976). Single-channel kinetics of developing muscle indicated a change in open time that corresponded to the developmental alteration in synaptic kinetics (Siegelbaum et al, 1984; Brehm et al, 1984a). The mechanism driving the change in open time was suggested to be either post-transcriptional conversion of a

single AChR type (Sakmann and Brenner, 1978, Michler and Sakmann, 1980), or expression of a new AChR type altogether (Brehm et al, 1984b).

The molecular nature of the nicotinic AChR was initially examined in channels purified from the torpedo electric organ, where it was determined that each AChR was composed of four distinct subunits termed α, β, δ and γ in the stoichiometry $\alpha_2\beta\delta\gamma$ (Karlin, 2002). Cloning of the skeletal muscle AChR subunits revealed another subunit, termed ε, and study of the reconstituted AChR channels in heterologous expression systems indicated that the basis for the changes in native AChR open time seen in developing muscle corresponded to expression of two different types of AChRs (Mishina et al, 1986). Early in development AChRs are composed of the $\alpha_2\beta\delta\gamma$ isoform whose long open duration confer the course of synaptic current decay measured in developing muscle. Later in development the γ subunit is replaced by the ε subunit, and this switch in molecular composition underlies the decrease in open time of the channel, and the results in a faster synaptic decay at mature neuromuscular junctions.

The developmental change in subunit composition was shown to be regulated at the level of transcription, where increased electrical activity resulted in expression of only the fast form of the receptor (Witzemann et al, 1987; Gu and Hall, 1988; Martinou and Merlie, 1991; Missias et al, 1996). Together, these discoveries revealed a fundamental mechanism by which cells alter synaptic transmission in response to activity. Control of synaptic kinetics by changes in expression of channel subunits is now an established theme in synaptic transmission throughout the central nervous system.

Although much was gained from our understanding of the mechanisms underlying fast muscle synaptic currents, comparatively less is understood about the nature of the

slow muscle synaptic currents. In particular, the basis of the prolonged synaptic current kinetics of slow muscle remains speculative. Some reports indicate that longer lifetime channels may exist in slow muscle (Hendersen and Brehm, 1989; Dionne, 1989). However, other evidence suggests that extrinsic factors, such as synaptic input and transmitter clearance mechanisms, account for the prolonged decay in zebrafish muscle (Nguyen et al, 1999). In my dissertation work, I have sought to understand the determinants of synaptic current kinetics that might distinguish zebrafish slow muscle from fast muscle types.

Zebrafish as a model system to examine fast and slow muscle

There are several reasons zebrafish present an excellent opportunity to examine the synaptic properties of tonic and twitch muscle. First, unlike most vertebrates, slow muscle fibers in teleost fish, such as the zebrafish, comprise layers distinct from fast muscle cells (reviewed in Sanger and Stoiber, 2001). Slow muscle is segregated from fast muscle even as early as 24 hours post fertilization (hpf), and forms a superficial monolayer of cells along the entire length of the tail musculature. All deeper muscle layers are comprised of fast muscle cells, excluding the layer of muscle precursor cells lying just adjacent to the notochord (van Raamsdonk et al, 1978,1982).

The rapid development and transparency of embryos have made zebrafish a tractable system in which to study early development. Neuromuscular contacts are formed very early in development (Liu and Westerfield, 1992), and by 72 hpf, neuromuscular junctions have morphological characteristics similar to those of mature synapses (Mos et al, 1983; Westerfield et al, 1990; Drapeau et al, 2001). Immunological

studies of larval and adult neuromuscular junctions suggest the pattern of synaptic protein localization established by 72 hpf is similar to that of mature synapses (Panzer et al, 2005), and also to that of other vertebrate synapses (Kummer et al, 2006). Zebrafish lacking essential vertebrate neuromuscular synaptic components are structurally or functionally compromised by 72 hpf (Sepich et al, 1998; Ono et al, 2001,2002; Downes and Granato, 2004; Kim et al, 2007).

Recordings from embryonic zebrafish indicate that both slow and fast muscle already exhibit the characteristic electrophysiological differences found between adult muscle types. Fast muscle is able to generate propagated action potentials while slow muscle is inexcitable (Buckingham and Ali, 2004). Additionally, spontaneous synaptic currents in slow muscle exhibit prolonged current decay compared to synaptic currents of fast muscle (Luna and Brehm, 2006). A technical advantage of working with zebrafish embryonic muscle cells is that they are relatively small and electrically compact compared to muscle fibers in other preparations; it has been possible to examine synaptic currents with the voltage-clamp technique using a single patch electrode (Nguyen et al, 1999; Wen and Brehm, 2005).

Finally, RNA knockdown is a molecular technique used extensively in embryonic zebrafish to examine the role of proteins throughout development. The synaptic characteristics of slow and fast muscle cells are established early enough in development to provide excellent temporal overlap with RNA knockdown strategies (Sumanas and Larson, 2002). Additionally, because zebrafish embryos are able to survive several days without muscle function, they are well suited for experiments designed to reduce or alter neuromuscular transmission (Westerfield et al, 1990; Ono et al, 2001). The combination

of these advantages provides an excellent opportunity to resolve the long-standing question of what underlies the difference in synaptic current kinetics in slow and fast muscle.

Significance

Although all vertebrates use both muscle types, mammalian slow muscle is best characterized in the extraocular muscles that maintain eye position. The precocious loss of extraocular slow muscle function in diseases such as myasthenia gravis has generated much interest, but how this sensitivity is conferred remains unclear. It has been proposed that differences in the acetylcholine receptor population of slow muscle cells may render them more sensitive to autoimmune forms of myasthenia gravis, but functional evidence supporting this hypothesis is lacking. Understanding the molecular nature of the functional distinctions between these two muscle synapses may provide insight into the mechanism underlying their different responses in the disease state and may ultimately guide therapeutic design.

CHAPTER 2

Materials and Methods

Zebrafish animal care

All of the experiments utilized zebrafish (Danio rerio) as the animal model system. The wild type (WT), and mutant lines were all maintained as adults in an OHSU approved facility. The methods used were consistent with the Panel on Euthanasia of the American Veterinary Medical Association, and were approved by the Institutional Animal Care and Use Committee.

Whole-cell recordings from zebrafish muscle

Preparation

Zebrafish embryos between the ages of 72 and 80 hours post fertilization (hpf) were prepared for all whole-cell voltage-clamp recording from muscle cells. Embryos were decapitated just rostral to the pec-fin segment, and the tail portion was pinned to a recording chamber with fine tungsten wire directly through the notochord. The skin on the topside of the tail was removed between the two pins using fine forceps. To inhibit muscle contraction, preparations were immersed in 1:10 V/V formamide in bath recording solution for ~ 2 mins, and then rinsed extensively. Bath recording solution contained, in mM: 135 NaCl, 10 mM Na-HEPES, 3 mM KCl, 2 mM CaCl2 and 1 mM

MgCl2, pH 7.4 and 278 mOsm. Unless otherwise noted, chemicals were purchased from Sigma-Aldrich.

Recording and data acquisition

Glass recording pipettes (World Precision Instruments, 1.5 mm) were pulled to a short taper and a tip inner diameter measuring approximately 3-4 um. For whole-cell recordings, pipettes were filled with a solution containing in mM: 120 KCl, 10 KHEPES, and 5 BAPTA, pH 7.4 and osmolarity was increased to ~278 mOsm with sorbitol. Electrodes generally had tip resistances between 1.8-2.5 MOhms.

Whole-cell recordings were obtained using an EPC-10 patch-clamp amplifier, and Pulse acquisition software (Heka Electronik). Data was acquired at 100 kHz, and initially filtered at 8.3 kHz with an analog Bessel filter. Once in the whole-cell configuration, series resistance estimates were generally between 3-6 MOhms. Series resistance was not compensated, because the voltage error (estimated by $I*R_s$) was ≤ 5%.

Muscle cells recordings usually lasted 3-4 minutes after entering the whole-cell configuration. As the recordings continued, both slow and fast muscle cell membranes demonstrated a tendency to seal-over the tip of the patch pipette. This manifested as a time dependent decrease in miniature amplitude, concurrent with a slowing of both rise and decay times. Only synaptic events exhibiting stable and fast rise times were considered for analysis, and recordings exhibiting time-dependent changes were not included.

Synaptic event analysis

Raw data was exported from Pulse and individual spontaneous synaptic currents were detected using the Mini Analysis software (Synaptosoft). After event detection,

current kinetics were extracted by fitting using either Mini Analysis software, or IGOR software (Wavemetrics). In Mini Analysis, the rise time is estimated as 10-90% of the time from baseline to peak amplitude, and the decay constant is determined by the exponential fit over 10-90% of the total decay amplitude. In IGOR, decay constants were determined by the exponential fit over the entire decay amplitude (peak to end fitting). Data was reported as mean ± standard deviation, and data sets were compared using a two-tailed Student's t-test to determine significance.

On-cell single-channel recordings from zebrafish muscle

Preparation

Preparation of the embryonic fish for on-cell muscle recordings was similar as described for whole-cell recordings. Sometimes, when muscle cells failed to provide high quality seals, tails were treated with 1X trypsin EDTA for ~1 min, to help clean the muscle cell surface. This treatment helped produce high resistance seal formation. For recordings from fast muscle, fish were prepared similarly, and then individual slow muscle cells were removed from entire segments using a large bore pipette (~10 to 20 μm) under gentle suction.

Recording and data acquisition

Single-channel recording electrodes were pulled to a tip diameter of ~1-3 μm, coated with Sylgard elastomer (Dow Corning), and lightly fire polished. Pipettes were filled with bath solution and different concentrations of ACh as indicated. The Axopatch 200B amplifier (Molecular Devices;Axon Instruments) and Pulse software was used for all single-channel data acquisition at a sampling rate of 100 kHz, and low-pass filtered at

10 kHz with a Bessel analog filter. Single-channel recordings were generally acquired in thirty-second segments at every 10 mV over a range of applied potential between +150 and -100 mV.

Single-channel event analysis

Raw data were imported into TAC software (Bruxton) for event detection, and digitally filtered at 5 kHz. Event detection was undertaken separately for each membrane potential. Recordings often contained more than one amplitude class, but in all cases event duration was measured at half amplitude. Detected events were exported to TACFIT software for analysis.

The minimum resolvable event duration cutoff was determined empirically by inspecting the relationship between event amplitude and duration. The amplitude of events with durations below ~150 μs was decreased, reflecting the limitations of the equipment in fully resolving the amplitude of very brief events. The value of 200 μs was used as the lower duration limit for all single channel analysis, representing the minimum duration for which the event amplitude was fully resolved in all recordings. The event amplitude was determined by the difference between the baseline (closed) and first level (open) values, and multi-level events were not included in analysis. Amplitude histograms were constructed and fit with a Gaussian function to determine the mean amplitude of the events. Each amplitude class was fit individually with a single Gaussian function.

The burst duration histograms were constructed and fit in TAC by the method described in Sigworth and Sine, 1987. The burst duration histogram for each amplitude class was analyzed separately by first separating the individual amplitude classes. The

peak of the transformed exponential fit of each duration histogram provided the mean as determined by the method of maximum likelihood.

Analysis values determined by TACFIT were exported, and data plots were constructed using either IGOR or Microsoft Excel software. Data plots were fit by regression analysis in Excel or IGOR, and R^2 values were reported. Data values were reported as mean ± standard deviation, and data sets were compared using a two-tailed Student's t-test to determine significance.

Heterologous expression of reconstituted AChRs

Identification of zebrafish AChR subunit complementary DNA (cDNA)

In collaboration with Dr. Fumihito Ono (NIAAA), zebrafish subunit cDNA were identified by searching zebrafish sequence databases with murine subunit sequence. Primer sequences were used based on database sequence, or in cases where putative zebrafish subunits were not identified, murine sequences were used to design degenerate primer sequences. PCR fragments representing full length cDNA sequences for each subunit were identified from zebrafish embryo (3dpf) cDNA libraries. PCR fragments representing full length cDNA sequences of each subunit were cloned into pTNT vectors (Promega) for expression of the corresponding synthetic RNAs in Xenopus oocytes.

Zebrafish subunit sequences and alignments

The predicted primary protein sequence identified for each zebrafish AChR subunit is indicated in the sequence alignments of Figures 5.1-5.8. Non-zebrafish protein sequences used for the alignments, and for the phylogenetic tree shown in Figure 5.8, were identified in the NCBI database and correspond to the indicated accession numbers:

Frog (Xenopus laevis): α P05377, β P49579, γ NP_0011080915, ε NP_001080916, δ NP_001095267. Mouse (Mus musculus):α NP_031415, β NP_033731, γ NP_033734, ε NP_033733, δ NP_067611. Chicken (Gallus gallus): α NP_990147, δ NP_001026488, γ NP_001026739. Pufferfish (Takifugu rubripes): α AAP51163, β AAP58383, β1a AAP58382, γ AAP49541, δ AAP43507, ε AAP49540. Human (Homo sapiens): α NP_000070, β NP_000738, γ NP_005190, δ NP_000742, ε NP_000071. Cow (Bos taurus): α NP_788837, β NP_776941, δ NP_776696, γ NP_776698, ε NP_776697

RNA preparation and injection

Stock of 1 μg/uL RNA were generated for each subunit (mMESSAGE machine, Invitrogen). RNA stock aliquots were mixed in the combinations indicated for each experiment just prior to injection. The Xenopus laevis oocytes were generously provided by Dr. David Dawson. Oocytes were stored in OR3 solution (50% Leibowitz media, 15 mM Na-Hepes, 1 mg/mL gentamycin, pH 7.6) and stage VI and V oocytes were prepared for injection by manual removal of the follicle cell layers. Finely tapered glass injection pipettes were broken to a tip outer diameter of ~10-15 μm, and filled with RNA combinations. Individual oocytes were injected (Drummond Nanoject) with ~36 ng of total RNA.

Two-electrode voltage clamp current analysis

Two to five days after RNA injection, oocytes were tested for responsiveness to ACh using two-electrode voltage clamp measurements. Finely tapered glass recording electrodes were filled with 3 M KCl, and current responses were obtained using the TEV200 amplifier (Dagan Instruments) and recorded with Pulse acquisition software. A

specially designed chamber allowed measurements of ACh-activated current by switching perfusion between bath solution and bath solution containing 30 μM ACh. Three consecutive applications of ACh were examined to determine the amplitude of the maximum current response.

Single-channel recordings from oocytes

Oocytes were prepared as described for macroscopic recordings, except that just before use the vitelline membrane was removed manually in the manner described by Mishina et al, 1986. A specially designed apparatus allowed the oocyte to rest in one well, while a newly formed outside-out patch was brought to a separate well for perfusion with bath solution containing different concentrations of ACh, as indicated.

Single-channel event acquisition and analysis

Single-channel data was acquired using an Axopatch 200B amplifier, and Pulse software. Data analysis methods were the same as described for the on-cell single channel recordings of muscle.

Quantitative real-time polymerase chain reaction (qPCR)

Whole-fish qPCR

Total RNA was extracted from pools of 20 zebrafish embryos/larvae (for each time point, 1, 2, 3, 8, and 21 dpf) using RNeasy mini kit (Qiagen). Total RNA was DNAse treated with TURBO DNAse (Ambion). Treated RNA was then reverse transcribed using High Capacity cDNA Reverse Transcription kit (ABI). First strand was used as a template for subsequent qPCR.

Transcript quantity was measured using the StepOnePlus system (ABI). Amplification of transcripts was detected by the fluorescence of sequence-specific probes (Taqman technology). The sequences of the primers and probes used for each transcript are as follows:

SUBUNIT	SENSE PRIMER	PROBE	ANTISENSE PRIMER
β	ttcgtgcggagtgaaggtgacata	agaagtggatcttcaacatgccctgg	actctcgctaaagcctgtgtccaa
β1a	aacttactgcctcgctacttgggt	aggaaccagtggaggaagagccaaa	acagtgctctcgttatggcttcct
δ	Dr03075552_g1	ggaaaacaacaatgatgcccagttt	
γ	agtggcgctctatgctaacacact	aagctcctgcgccatcaaagtcaact	tgctgcaattctgccagtcaaagg
ε	Dr03115283_g1	gcacactggtcttcaggtctcagac	
elf1a	ttgatgcccttgatgccattctgc	attggaactgtacctgtgggtcgtgt	acaaccataccaggcttgaggaca

Whole Fish qPCR transcript quantification

Absolute transcript copy numbers were determined using the standard curve method. Quantification of known amounts of target DNA was used to establish a comparative for unknown transcript levels of specific subunits at various developmental stages (1, 2, 3, 8, and 21 dpf). From the standard curve quantification of the transcript number was determined. Numbers were normalized to the endogenous control elongation factor1 1-alpha (elf1-a) to account for variations in concentration (quantity) of starting template. E1f1-a has been previously characterized as a transcript expressed at constant levels throughout the developing zebrafish embryos (Tang et al, 2007). Normalized absolute numbers from multiple runs were plotted with SD.

Fast and slow muscle qPCR

Fish were prepared as described for single channel recordings in muscle. Under 400X magnification (Axioskop FS2, Carl Zeiss), small numbers (~10) of slow or fast muscle cells were individually suctioned into large diameter (~15 μm) patch pipettes, and the contents of the pipette dispelled into RNAlater storage buffer (Ambion) until total

RNA extraction. RNA was extracted from samples using RNeasy mini kit (Qiagen). RNA samples were then treated with TurboDNAse (Ambion). Total RNA was reverse transcribed using iScript cDNA Synthesis Kit (Bio-Rad).

QPCR was carried out using an ABI StepOnePlus (ABI) system. Amplification of transcripts was detected by the fluorescence of sequence-specific probes (Taqman technology). The sequences of the primers and probes used for each transcript were as indicated for whole-fish qPCR.

Fast and Slow qPCR comparative analysis

In this analysis, each transcript was normalized to the measured levels of the endogenous control e1f1-a. This normalization generates a ΔCt value ($Ct_{Experimental}$-Ct_{e1f1a}) and controls for variations in quantity of input material. After normalization, transcript levels were found using the following equation; copy number = $2^{(-\Delta Ct)}$. Experimental variation was measured by calculating the standard deviation (SD) of copy number: SD = $(\ln 2)(stdev_{\Delta Ct})(2^{(-\Delta Ct)})$. To adjust for the variability in overall signal between cell collections, the copy number for each target was normalized to the total copy number of all targets in each experiment and the relative copy number was reported.

Morpholino RNA knock-down in vivo

Morpholino preparation and design

Morpholinos (GeneTools) are modified antisense oligonucleotides designed to anneal to mRNA and interfere with protein synthesis either by directly hindering translation initiation or by causing splicing errors. Morpholinos (MOs) were designed for each target in accordance with the manufacturer's suggestions. The sequences of each

MO used are indicated in Table 7.1. MOs were resuspended in 1 mM stock solutions in water, and 0.5 to 1.5 nL volume droplets were pressure injected into newly fertilized zebrafish eggs at the one-cell stage. Each MO resulted in slightly different morphological or motility effects, and so the final amount injected (in ng) was empirically determined for each MO as the maximum amount that still rendered fast and slow muscle amenable for recordings. Final amounts ranged between 1 and 12 ng of MO per embryo, for all MOs tested.

For knockdown experiments using splice MOs, it was possible to measure the target transcript splicing errors using PCR. For these experiments, cDNA was prepared from embryos injected with splice MO as previously described for qPCR analysis. The target sequence was examined by end-point PCR over the region predicted to contain splice errors (see Figure 7.5). PCR products excised and sequenced to verify they represented the predicted splice error products.

Whole-cell recordings from MO injected fish

Fish were prepared for whole-cell muscle recordings as specified for WT fish. Unless otherwise indicated, whole-cell recordings were performed on the fast and slow muscle of fish between 72 and 80 hours post injection. Recording setup, acquisition parameters and data analysis were all as previously described for WT whole-cell recordings.

CHAPTER 3

Synaptic physiology of fast and slow muscle in zebrafish

A key advantage of the zebrafish system for the comparison of fast and slow skeletal muscle function is the anatomical segregation of the two cell types. Zebrafish embryos require little manipulation to prepare them for slow muscle recordings; the skin is simply peeled away, exposing the slow muscle cells. Fast and slow muscle cells are easy to distinguish using differential-interference contrast (DIC) optics, based on differences in location and orientation. Figure 3.1A shows a fish prepared for recordings from slow muscle. The slow muscle cells form the most superficial layer and are oriented parallel to the rostrocaudal axis of the fish.

Synaptic current properties of zebrafish slow muscle cells

Slow muscle cells can be effectively voltage-clamped using the whole-cell mode of patch clamp. Two types of events are seen throughout a recording from slow muscle cells; large amplitude events with a fast rise and decay (Figure 3.1B, arrowhead "a"), and smaller events with a slow rise and decay (Figure 3.1B, arrowhead "b"). The smaller and slower class of events are electrotonic reflections of synaptic events generated in neighboring slow muscle cells (Luna and Brehm, 2006). The larger and faster class of events represents miniature synaptic currents originating in the voltage-clamped cell.

Figure 3.1: Properties of zebrafish slow muscle synaptic currents. A) Live image of the superficial slow muscle layer viewed with DIC illumination and 400X magnification. The dashed line indicates the boundaries of a single slow muscle cell, and the scale bar indicates 10 μm. B) Example recording of synaptic currents from a slow muscle cell voltage-clamped at -90 mV. Arrowhead "a" indicates synaptic event, arrowhead "b" indicates electrotonic current originating in neighboring cell. C) The decay of a slow muscle synaptic current is exponential (red overlay), and the peak-to-end fit indicates a τ_{decay} was 2.9 ms, at -90 mV. D) Left: Example synaptic current from slow muscle fit poorly by a single exponential fit (red) at -90 mV. Right: Same synaptic current fit peak-to-end with two exponents. The fast component is indicated by the green fit, and corresponds to a τ_{decay} of 0.36 ms, and 24% of the overall amplitude. The slower component is indicated in red, and corresponds to a τ_{decay} of 3.4 ms. E) Scatter plot of the average τ_{decay} values for all 15 slow muscle cells fit 10-90% with a single exponent (filled circles), alongside the overall mean τ_{decay} ± SD (open circle). F) Frequency histogram of the τ_{decay} values for all synaptic currents from slow muscle recorded at -90 mV. The Gaussian fit (black) indicates a distribution mean of 3.1 ms.

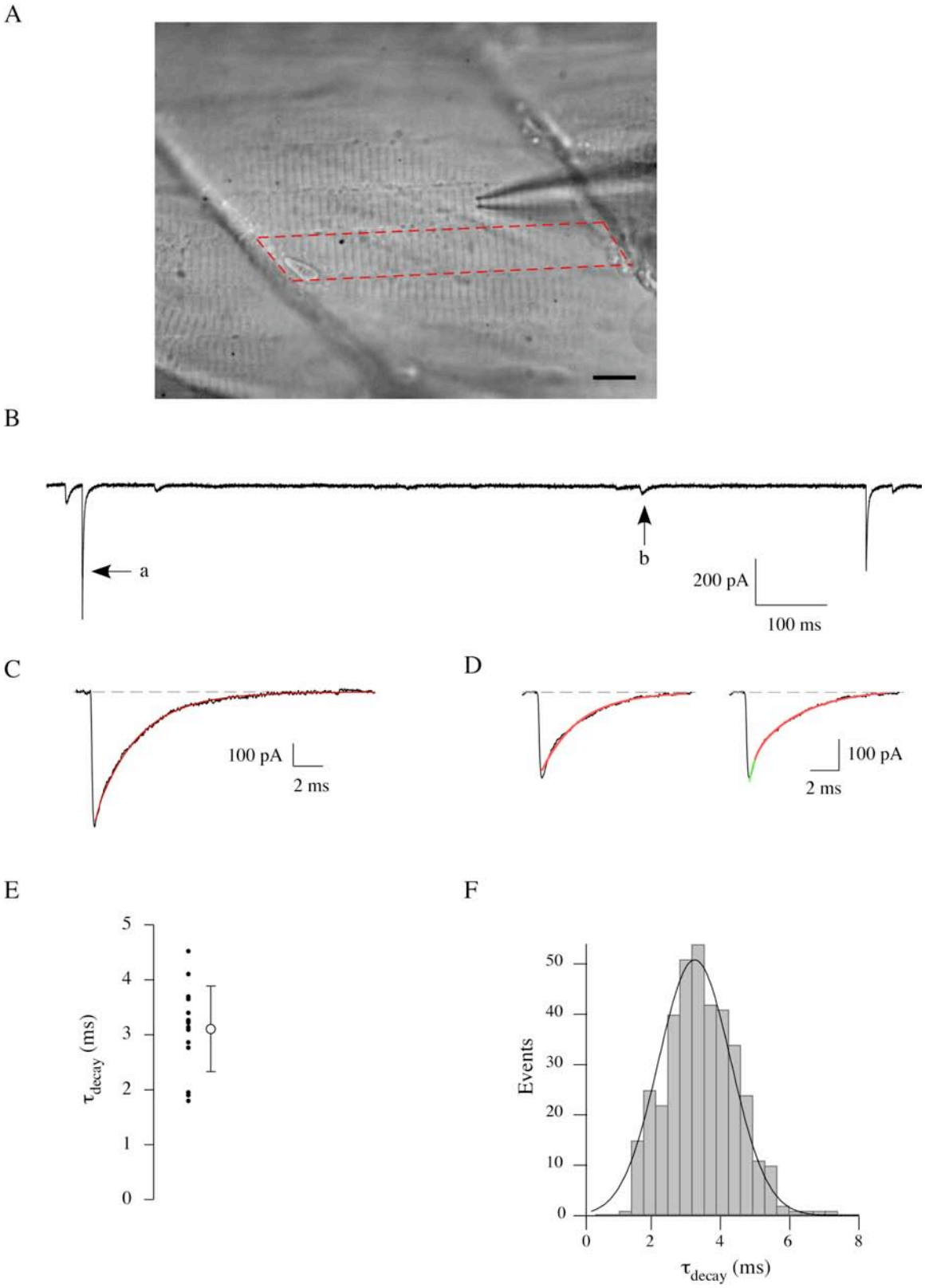
A
B
a
b
200 pA
100 ms
C
100 pA
2 ms
D
100 pA
2 ms
E
τ_{decay} (ms)
0
1
2
3
4
5
F
Events
0
10
20
30
40
50
0
2
4
6
8
τ_{decay} (ms)

The difference in amplitude of these gap-junction currents makes them easy to separate from synaptic events, and events smaller than 100 pA were excluded from analysis.

The time-course of the peak-to-end amplitude decay of an individual synaptic event in slow muscle was generally well fit by a single exponential function, and the average time constant of decay (τ_{decay}) was approximately 3.0 ms at -90 mV (Figure 3.1C). However, a single exponential fit did not fully describe the peak-to-end decay of every event, and 65 of the 376 events (17%) from 15 slow muscle cells required two exponential components to fully describe their decay (Figure 3.1D). The majority of the current decay is still attributed to the slow component seen in all synaptic currents, but these events also had a faster component (τ_{decay}= 0.43 ± 0.1 ms) that contributed an average of 20% to the total amplitude. Because at least 80% of the decay is still represented by the slow component for all events examined, I fit all slow muscle synaptic currents with a single exponential over 10-90% of the total decay amplitude to estimate the overall decay time constant. For consistency, decay fitting was done over 10-90% amplitude for all synaptic currents examined in both slow and fast muscle.

I estimated the overall average τ_{decay} in slow muscle cells by two methods. First, I fit the events from a single cell, and determined the average τ_{decay}. Then, I determined the mean τ_{decay} of all cells, yielding an overall τ_{decay} of 3.0 ± 0.7 ms (n=15 cells). The individual cell averages, and the overall average are shown in the scatter plot of Figure 3.1E. As a second means to determine the overall τ_{decay}, I plotted the τ_{decay} of each synaptic event from all cells (376 events) as a frequency distribution (Figure 3.1F). The distribution was fit with a Gaussian function, and exhibited a mean τ_{decay} of 3.1 ± 1 ms. Good agreement was found with both methods of estimation.

Synaptic current properties of zebrafish fast muscle

The preparation for fast muscle recordings followed the same initial steps as the preparation for slow muscle. Often, I first recorded from a few slow muscle cells in a fish, and then prepared the fish for fast muscle recordings. To reveal the fast muscle, the slow muscle cells were removed individually using a large diameter glass pipette under gentle suction. With care, every slow muscle cell in several segments was suctioned away, without damaging the underlying fast cells. In Figure 3.2A, the first layer of cells has been removed by suction pipette, and the remaining cells are fast muscle cells.

The spontaneous miniature synaptic currents in fast muscle (Figure 3.2B) differ in several ways from those of slow muscle. First, the small and slowly decaying event class reflecting gap-junction currents was seen far less frequently. In the example trace of Figure 3.2B, no currents arising from neighboring cells are present. This is thought to reflect the limited electrical coupling of fast muscle cells (Luna and Brehm, 2006). Second, the synaptic events in fast muscle were more frequent, and larger in amplitude than in those of slow muscle. Finally, synaptic current decays were much briefer in fast muscle.

Close inspection of an individual event shows that the peak-to-end amplitude decay of synaptic events in fast muscle was exponential (Figure 3.2 C). For comparison with slow muscle, the τ_{decay} values were also determined by fitting 10-90% of the decay, and the average τ_{decay} for fast muscle events was approximately 0.5 ms at -90 mV. The average τ_{decay} was determined in two ways, as previously described for slow muscle events. The average τ_{decay} of each cell (n=14 cells) is shown as a scatter plot in Figure

Figure 3.2: Properties of zebrafish fast muscle synaptic currents. A) Live image of the fast muscle cell layers zebrafish tail, viewed with DIC illumination at 400X magnification. The dashed line indicates the boundaries of a single fast muscle cell, and the scale bar indicates 10 μm. B) Example recording of synaptic currents from a fast muscle cell voltage-clamped at -90 mV. C) The decay of a fast muscle current is exponential, and the fit (red overlay) indicates a τ_{decay} of 0.51 ms, at -90 mV. D) Scatter plot of the average τ_{decay} values for 14 fast muscle cells (filled circles), alongside the mean τ_{decay} ± SD (open circle). E) Frequency histogram of the τ_{decay} values for all synaptic currents in fast muscle recorded at -90 mV. The Gaussian fit (black) indicates a distribution mean of 0.54 ms.

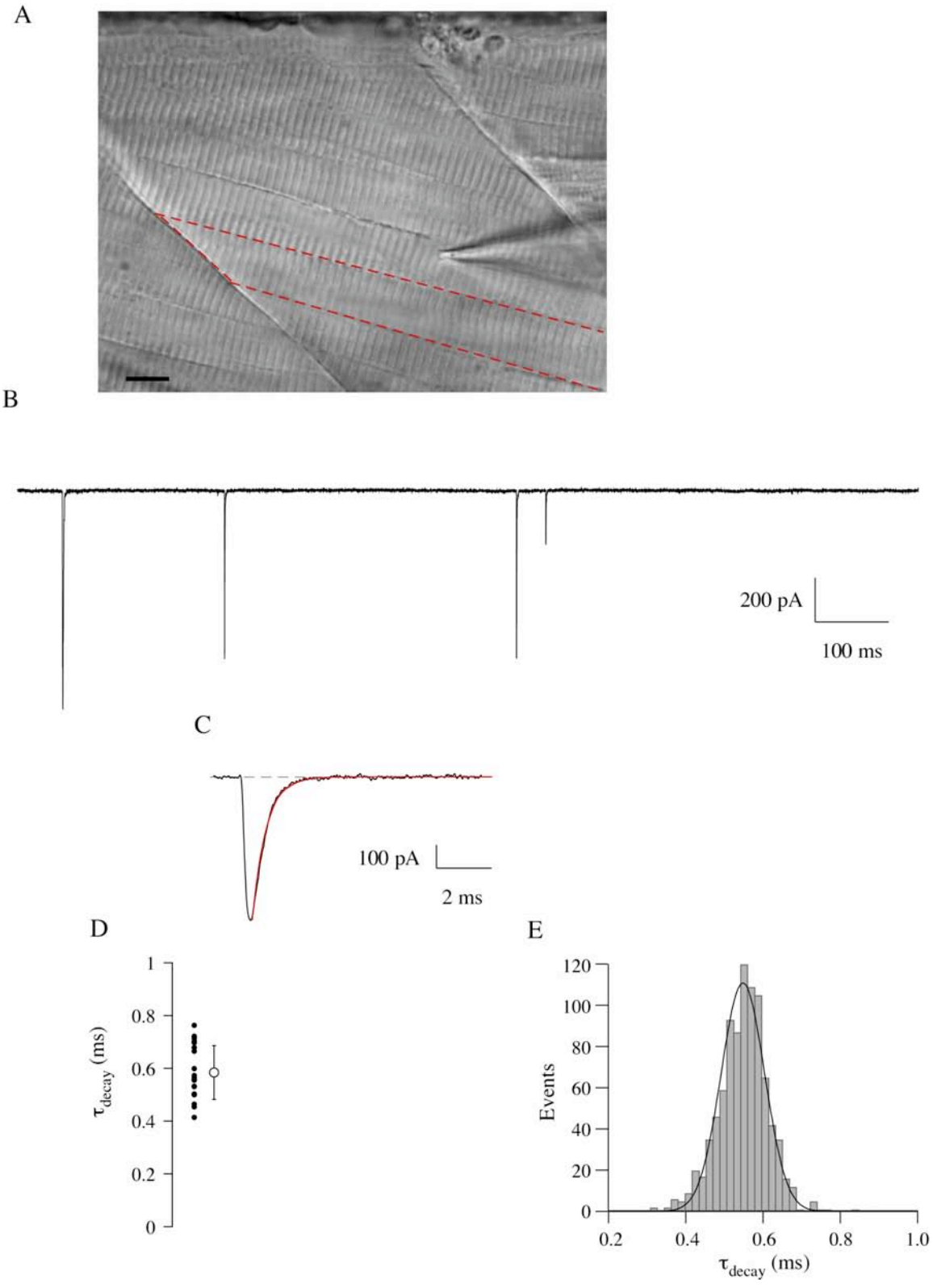
A
B
200 pA
100 ms
C
100 pA
2 ms
D
τ_{decay} (ms)
1
0.8
0.6
0.4
0.2
0
E
Events
120
100
80
60
40
20
0
0.2
0.4
0.6
0.8
1.0
τ_{decay} (ms)

3.2D, and the overall average corresponded to 0.58 ± 0.1 ms. The frequency distribution of τ_{decay} for the individual synaptic events (894) is shown in Figure 3.2E. The Gaussian fit to the distribution indicates a mean τ_{decay} of 0.54 ms ± 0.08 ms. Once again, the two methods of estimation showed good agreement.

Comparison of the average τ_{decay} between fast and slow muscle indicated the 5-fold difference at -90 mV noted by Luna and Brehm, 2006. In that study, the difference in decay was confirmed by paired extracellular and whole-cell recordings of synaptic events.

The role of transmitter clearance in synaptic decay kinetics

Generally, the time course of muscle synaptic currents has been assigned to the intrinsic closing rate of the AChR (Katz and Miledi, 1971, 1972; Andersen and Stevens, 1973). However, altering transmitter clearance rate by inhibiting the enzyme acetylcholinesterase (AChE) has been shown to prolong current decay (Takeuchi and Takeuchi 1959, Kordas 1969). This prolongation was thought to reflect AChRs re-binding ligand and re-opening multiple times (Katz and Miledi 1972, 1973). During early development of Xenopus myocytes, acceleration of the synaptic current decay was due, in part, to the onset of AChE activity (Kullberg et al, 1980). Furthermore, the extent of AChE effect on decay also differed between muscle types during development (Kullberg and Owens, 1986).

The extent to which AChE activity influences fast and slow synaptic decay in the developing zebrafish embryo is not known. Therefore, it remained possible that differences in AChE activity were responsible for the 5-fold difference in τ_{decay} between

fast and slow muscle synaptic currents. For example, if AChE was not active at slow muscle synapses, then AChRs at slow muscle synapses would re-open multiple times in response to transmitter release, resulting in prolonged synaptic current decays. Conversely, if AChE activity was high at fast muscle synapses, re-opening would be minimal resulting in a current decay that converged on the mean burst duration of the AChRs (Colquhoun and Sakmann, 1981; Grosman and Auerbach, 2001). If AChE was responsible for the difference in τ_{decay} between fast and slow muscle, then inhibiting AChE would be predicted to lengthen the synaptic duration in fast muscle to the extent observed for slow muscle. Using a recently identified AChE null line of zebrafish, I was able to directly test this hypothesis.

Fast muscle synaptic current decay in a zebrafish AChE null

The zebrafish mutant zieharmonika (zim^{tm205}) was established as an AChE null (Downes and Granato, 2004). The zim^{tm205} line was previously generated in a mutagenesis screen (Granato et al, 1996), and the line carried a recessive point mutation that encodes a premature stop codon. This premature stop codon resulted in loss of the catalytic domain of AChE (Figure 3.3A, left). Staining for AChE activity in zim^{tm205} mutants ($zim^{-/-}$) indicated complete loss of esterase activity in muscle (Figure 3.3A, right). In zebrafish, AChE was shown to be the only esterase active at the neuromuscular junction (Bertrand et al, 2001). Therefore, the $zim^{-/-}$ mutants provided an opportunity to determine decay times of fast and slow muscle, in the absence of AChE. These experiments were undertaken in collaboration with a fellow lab member, Michael Walogorsky, who was recording from these mutants in a separate set of studies.

Figure 3.3: Properties of synaptic currents in $zim^{-/-}$ fast muscle. A) Left: Identification (top) and location (bottom, transcript represented) of the of the zim^{tm205} point mutation. Right: Stain of cholinesterase activity in the tail musculature of WT (left) and $zim^{-/-}$ (right) embryos (Taken from Granato and Downes, 2004). Scale bar indicates 20 μm. B) Representative $zim^{-/-}$ synaptic current (red), and WT synaptic current (black), recorded in fast muscle cells voltage-clamped at -90 mV. The τ_{decay} corresponds to 0.95 ms for $zim^{-/-}$ and 0.54 ms for WT. C) Scatter plot indicating the average τ_{decay} values for all 28 $zim^{-/-}$ fast muscle cells (red filled circles), and the mean τ_{decay} value ± SD (red open circle). WT τ_{decay} values are included in black, for comparison. D) Frequency histogram of τ_{decay} values for all $zim^{-/-}$ synaptic currents in fast muscle, at -90 mV. The Gaussian fit (black) indicates an average τ_{decay} of 0.90 ms for the distribution. E) Frequency histogram of τ_{decay} values for $zim^{-/-}$ (no fill) and WT (grey fill) fast muscle cells.

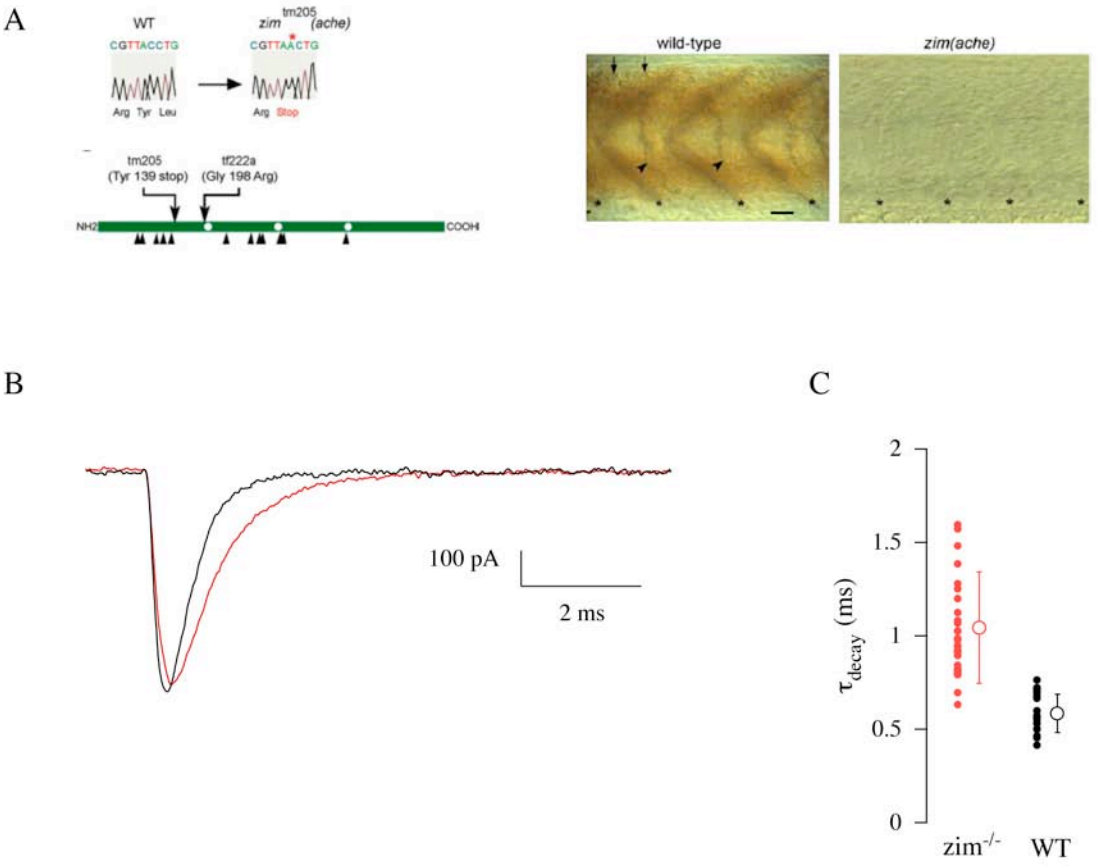
A
WT
zim tm205 (ache)
CGTTACCTG
CGTTAACTG
Arg Tyr Leu
Arg Stop
tm205
(Tyr 139 stop)
tf222a
(Gly 198 Arg)
NH2
COOH
wild-type
zim(ache)
B
100 pA
2 ms
C
τdecay (ms)
zim-/-
WT
D
Events
τdecay (ms)
E
Events
τdecay (ms)

Synaptic currents were first examined in fast muscle (Figure 3.3B). The τ_{decay} of the example trace is 0.95 ms for zim$^{-/-}$, and 0.51 ms for WT. The average τ_{decay} of all the events from a single fast muscle cell from zim$^{-/-}$ (n=28 cells) and WT is shown in Figure 3.3C. The overall average τ_{decay} of zim$^{-/-}$ fast muscle currents, determined as previously described for WT synaptic currents, was 1.0 ± 0.3 ms. This indicated an average 1.7-fold increase in the τ_{decay} at fast muscle synapses lacking AChE activity.

The overall τ_{decay} was also determined by fitting a cumulative frequency histogram constructed from the τ_{decay} of each synaptic event (Figure 3.3D, 1608 events). The Gaussian fit to the cumulative distribution indicated an average τ_{decay} of 0.9 ± 0.25 ms for zim$^{-/-}$ fast muscle cells. For comparison, the cumulative distributions of zim$^{-/-}$ and WT fast muscles τ_{decay} are shown together, in Figure 3.3E. The cumulative data indicated fast muscle synaptic current decays were approximately 1.7-fold prolonged at synapses lacking AChE, in good agreement with the estimate determined by cell averages.

Slow muscle synaptic current decay in an AChE null

A representative synaptic current from zim$^{-/-}$ and WT slow muscle is shown in Figure 3.4A. The τ_{decay} of the example current was 3.7 ms for zim$^{-/-}$ and 2.9 ms for WT. The average τ_{decay} determined for each zim$^{-/-}$ slow muscle cell (n=15) is shown in Figure 3.4B. The overall average τ_{decay} of zim$^{-/-}$ slow muscle cells was 3.7 ± 0.6 ms. There was a 1.2-fold prolongation of synaptic current decay in the absence of AChE.

The overall τ_{decay} was also estimated by fitting a cumulative frequency histogram constructed from the τ_{decay} of each slow muscle event in zim$^{-/-}$ (Figure 3.4C, 440 events). The Gaussian fit to the cumulative distribution indicated an average τ_{decay} of 3.4 ± 1 ms.

Figure 3.4: Properties of synaptic currents in $zim^{-/-}$ slow muscle. A) Representative $zim^{-/-}$ slow muscle synaptic current (red), and WT synaptic event (black) recorded from slow muscle cells voltage-clamped at -90 mV. The τ_{decay} corresponds to 3.7 ms for $zim^{-/-}$, and 2.9 ms for WT. B) Scatter plot indicating the average τ_{decay} values for all 14 $zim^{-/-}$ slow muscle cells (red filled circles), and the mean τ_{decay} value ± SD (red open circle). WT τ_{decay} values are included in black, for comparison. C) Frequency histogram of τ_{decay} values for all $zim^{-/-}$ synaptic currents in slow muscle, at -90 mV. The Gaussian fit (black) indicates an average τ_{decay} of 3.4 ms for the distribution. D) Frequency histogram of τ_{decay} values for $zim^{-/-}$ (no fill) and WT (grey fill) slow muscle cells.

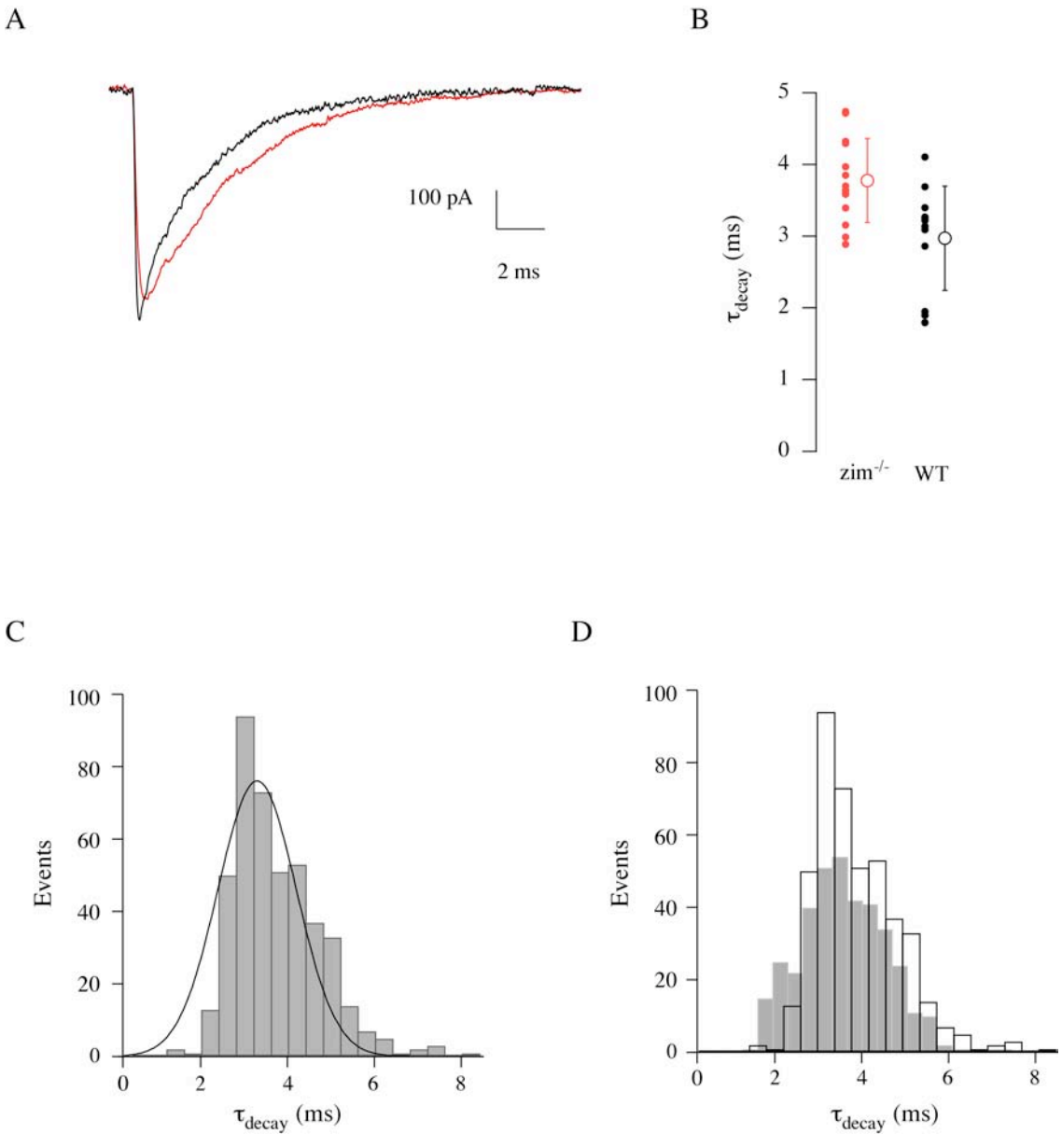
A
100 pA
2 ms
B
τ_{decay} (ms)
zim$^{-/-}$
WT
C
Events
τ_{decay} (ms)
D
Events
τ_{decay} (ms)

The cumulative distributions of both zim-/- and WT slow muscle τ_{decay} are shown in Figure 3.4D, for comparison. The cumulative data estimated that slow muscle τ_{decay} was increased by 1.1-fold, in the absence of AChE.

A summary of τ_{decay} values for WT and $zim^{-/-}$ is shown in Figure 3.5A. If the lack of AChE activity alone was sufficient to explain the τ_{decay} of slow muscle, then $zim^{-/-}$ fast τ_{decay} should have become indistinguishable from WT slow muscle τ_{decay}. Comparison of the cell averages indicated that without AChE activity, the average τ_{decay} in $zim^{-/-}$ fast muscle was still 3-fold faster than that of WT slow muscle. A similar result was obtained by comparison of the cumulative τ_{decay} distributions of WT slow muscle, and $zim^{-/-}$ fast muscle (Figure 3.5B). Gaussian fits to the cumulative data indicated the average $zim^{-/-}$ fast muscle τ_{decay} remained 3.7-fold faster than the average WT slow muscle τ_{decay}.

Figure 3.5: Summary of synaptic current properties in $zim^{-/-}$ and WT muscle. A) Scatter plot of average τ_{decay} for individual cells (filled circles) and corresponding mean τ_{decay} ± SD (open circles). B) Frequency histogram of τ_{decay} values for all synaptic currents in $zim^{-/-}$ fast muscle (grey fill) and WT slow muscle (no fill), recorded at -90 mV.

A

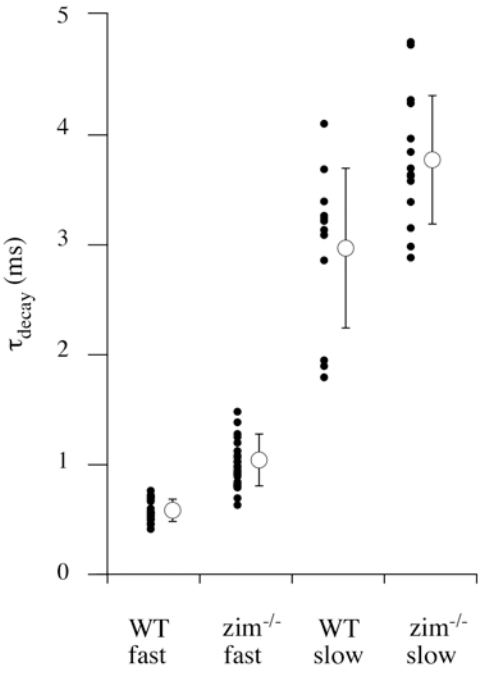
5
4
3
2
1
0
τ_{decay} (ms)
WT fast
zim$^{-/-}$ fast
WT slow
zim$^{-/-}$ slow

B

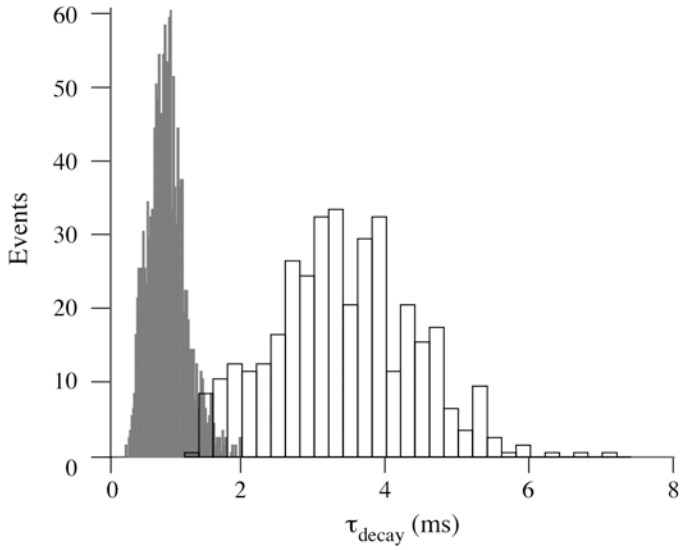
60
50
40
30
20
10
0
Events
0
2
4
6
8
τ_{decay} (ms)

CHAPTER 4

Fast and slow muscle single-channel AChR characteristics

In Chapter 3, I presented evidence that transmitter clearance rate cannot explain the difference between the τ_{decay} of fast and slow muscle synaptic events. Even in the absence of active clearance, there still remains an unaccounted for 3-4 fold difference. As mentioned previously, many studies have shown synaptic decay time course depends on the receptor burst duration. Therefore, I tested whether intrinsic differences in the mean burst duration between AChRs on fast and slow muscle could account for the differences in synaptic decay.

To determine the single channel characteristics of the native AChRs, I recorded on-cell ACh-activated currents from both slow and fast muscle cells in the intact fish. Typically, cells used for single-channel analysis have been dissociated to obtain high-quality recordings with low noise. However, dissociated slow and fast muscle cells would have lost the positional landmarks and orientation needed to discriminate between them. I therefore prepared fish for either slow (skin removed) or fast muscle (skin and slow muscle removed), in order to record using the on-cell configuration.

The on-cell configuration was the only mode in which I was able to record single-channel currents from muscle. Attempts to record from the outside-out configuration resulted in patches that required large holding currents and were very noisy, reflecting

either a leaky membrane seal, or a very large patch. I also attempted to record from inside-out patches, but they were unstable and noisy.

Characterization of the primary ACh-activated event class of fast muscle

Representative on-cell single-channel recordings from fast muscle are shown in the top trace in Figure 4.1A. These ACh activated channel currents were elicited in response to low concentrations of ACh (300 nM) in the recording electrode, representing the foot of the dose response curve for muscle nicotinic AChRs. This minimized the complications associated with both overlapping events and receptor desensitization. Receptors seemed to be present at all positions along the cell surface, and no effort was made to localize recordings to a specific region of the cell.

The single-channel events all represented openings of AChRs as evidenced by their dependence upon ACh. With a low concentration of ACh, events occurred at a low frequency throughout the recording (Figure 4.1A). These events reflect the transition of a single AChR between single transition between the shut and open state. Occasionally, the openings are interrupted by extremely brief closures termed 'nachschlags' (Colquhoun and Sakmann, 1981; 1985). Due to the frequency response of these recordings, extremely brief closures ($\leq$ 80 μs) were not resolved, and so two transitions separated by nachschlags were counted as one. Because of this limitation, the measurement of event duration represents the burst duration, rather than open duration. When the concentration of ACh was raised to 10 μM, events occurred in extended periods of bursting wherein channels transitioned repeatedly between open and shut states. Each extended burst was separated by long quiescent periods. This prolonged

bursting was a characteristic behavior of desensitized AChRs (Sakmann et al., 1980; Sine and Steinbach, 1984; Auerbach and Lingle, 1986) and represented repeated openings by a single AChR. Burst onset reflected the recovery of a single AChR from the desensitized state, and then termination reflected re-entry into the desensitized shut state. Although this behavior provides much kinetic information for AChRs, I was unable to use high concentrations of ACh for single channel analysis of zebrafish AChRs. First, desensitized channels remained silent for long periods of time and re-opened infrequently, rendering bursts rare. Secondly, even at 10 μM ACh, it appeared that ACh functioned as an open-channel blocker of the receptor. The mean burst duration of all receptor types consistently decreased at 10 μM ACh (~1.5-fold), compared to 300 nM (Appendix 1). At 100 μM ACh, the open-channel block became obvious as both the mean burst duration and the amplitude of events decreased (Appendix 2). To avoid possible errors in kinetic measurements due to block, I restricted single-channel analysis to the data collected at low concentrations of ACh (≤300 nM).

Single-channel events on fast muscle were consistent in amplitude throughout a recording at a given applied potential, and most openings fell into a single amplitude distribution (Figure 4.1B). However, in 7 of 12 recordings there was an additional class of smaller amplitude events that contributed an average of 7% to the total number of events. The properties of the secondary class will be considered following the characterization of the primary amplitude class.

The amplitude distribution of the primary class was fit with a Gaussian function to determine the mean amplitude at each applied potential. The example patch shown has a mean amplitude of 8.7 pA at +40 mV applied potential (Figure 4.1B). To estimate the

Figure 4.1: Properties of ACh-activated single-channel events of fast muscle. A) Sample events from an on-cell recording at an applied potential of +40 mV. B) Amplitude distribution for single-channel currents at an applied potential of +40 mV, fit by a Gaussian function (black). C) Current-voltage relationship for the patch recording from B. The linear fit to the data corresponds to a slope conductance of 70 pS. Dashed line indicates zero-current level. D) Current-voltage relations for all 12 recordings are fit by linear regression (black lines). E) On the left, a scatter plot indicates the conductance determined for each recording, (filled circles), along with the mean ± SD for all recordings (open circle). On the right, a scatter plot of estimated resting potential for each recording (filled circles) with outlier cells indicated in red. The mean ± SD (open circle) estimated resting potential for all recordings indicated by black circles. F) Cumulative current-voltage plot for all recordings, fit by linear regression. The slope conductance corresponds to 67 pS.

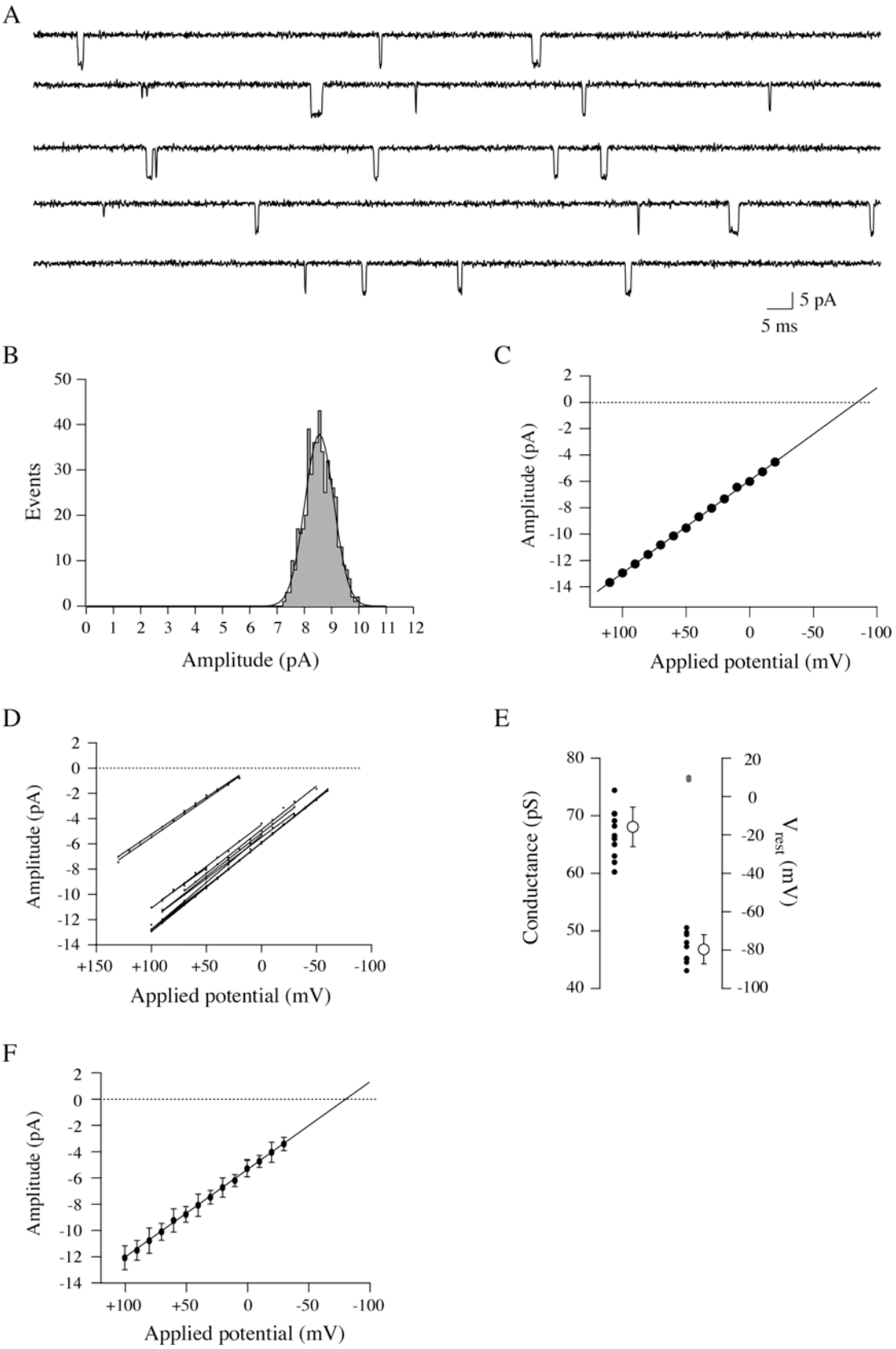
A
5 pA
5 ms
B
Events
Amplitude (pA)
C
Amplitude (pA)
Applied potential (mV)
D
Amplitude (pA)
Applied potential (mV)
E
Conductance (pS)
V rest (mV)
F
Amplitude (pA)
Applied potential (mV)

single-channel conductance, the mean amplitude was determined over a range of applied potentials between +130 and -30 mV, in 10 mV increments. A current-voltage plot was constructed from the mean amplitude at each applied potential (Figure 4.1C), and fit by linear regression to determine the slope of the fitted line. The example plot in Figure 4.1C corresponds to a 70 pS single-channel conductance.

The linear fit to the current-voltage data also provided an estimate of the resting membrane potential (V_{rest}) of the cell. Because the AChR passes a mixed cation current, the reversal potential of the channel is ~0 mV. Therefore, at the zero current level for ACh-activated channels, the applied potential is equal to the membrane potential inside the cell (0 mV net transmembrane potential). For the data in Figure 4.1C, the extrapolated zero current point corresponded to an estimated V_{rest} of -83 mV. The current-voltage relationship for each recording are shown in Figure 4.1D. The slope values for all 12 recordings are shown in Figure 4.1E, in addition to the mean slope conductance of 68 ± 3.5 pS.

The x-intercept values, representing the estimated V_{rest}, are shown in Figure 4.1E. Although most of the values centered around -80 mV, two cells indicated resting potentials around 0 mV. These two cells are the two outliers seen in the current-voltage plot in Figure 4.1D. It is possible that these two cells were damaged, obliterating the resting potential. Alternatively, it is possible that I dislodged the patch and was recording in the inside-out configuration. Regardless, the slope of the fit was similar to the other 10 cells shown (63 and 67 pS), indicating that conductance is independent of resting potential. Excluding the two outlier cells, the average resting potentials for the remaining 10 fast muscle cells was -80 ± 7.6 mV (Figure 4.1E).

Additionally, I estimated the single-channel conductance by constructing a cumulative current-voltage plot corresponding to the average amplitude of all recordings at each potential. Excluding the two outliers, the average amplitude at a single applied potential ranged between 7.9 and 9.4 pA at the applied potential of +50 mV. The cumulative current-voltage plot (Figure 4.1F), was also well fit by linear regression, and indicated an average single-channel conductance of 67 pS. The x-intercept corresponded to an estimated V_{rest}, of -82 mV. The cumulative data analysis agreed well with the averages of the individual recordings.

Of paramount interest were the kinetics of the primary AChR class on fast muscle. Visual inspection of the example events from native fast muscle (Figure 4.1A) revealed brief openings upon activation by ACh. To determine the mean burst time, a frequency histogram of the burst duration was plotted at a given applied potential. On a linear scale, the burst duration frequency histogram was distributed exponentially (Figure 4.2A). Fitting the distribution of burst durations for the sample recording shown in Figure 4.1A yielded a mean burst duration of 0.52 ms (Figure 4.2A). Alternatively, the burst duration histogram was plotted using a semi-logarithmic scale and fit with a transformed exponential function (Sigworth and Sine, 1987). The peak of the fitted curve corresponded to the mean of the distribution. Fitting the same event distribution in this manner also yielded an average burst duration of 0.52 ms (Figure 4.2B). All single channel data burst duration histograms were presented on a semi-log plot, and distribution means were determined by fitting with the transformed exponential function.

The average burst duration of the primary AChR class on fast muscle was determined at +50 mV applied potential for each recording. Five of 10 recordings

Figure 4.2: Burst duration of the primary class of ACh-activated channels of fast muscle. A) Burst duration distribution for events >200 μs fit to a single exponential function. The mean burst duration (τ) corresponds to 0.52 ms and is indicated by the arrow. B) The burst duration distribution plotted on a semi-log scale, and fit with a transformed exponential function. The peak of the fitted curve (arrow) also indicates a mean burst duration of 0.52 ms. C) The scatter plot indicates the average burst duration of the primary event class at +50 mV applied potential for each recording (filled circles), alongside the overall mean burst duration ± SD (open circle).

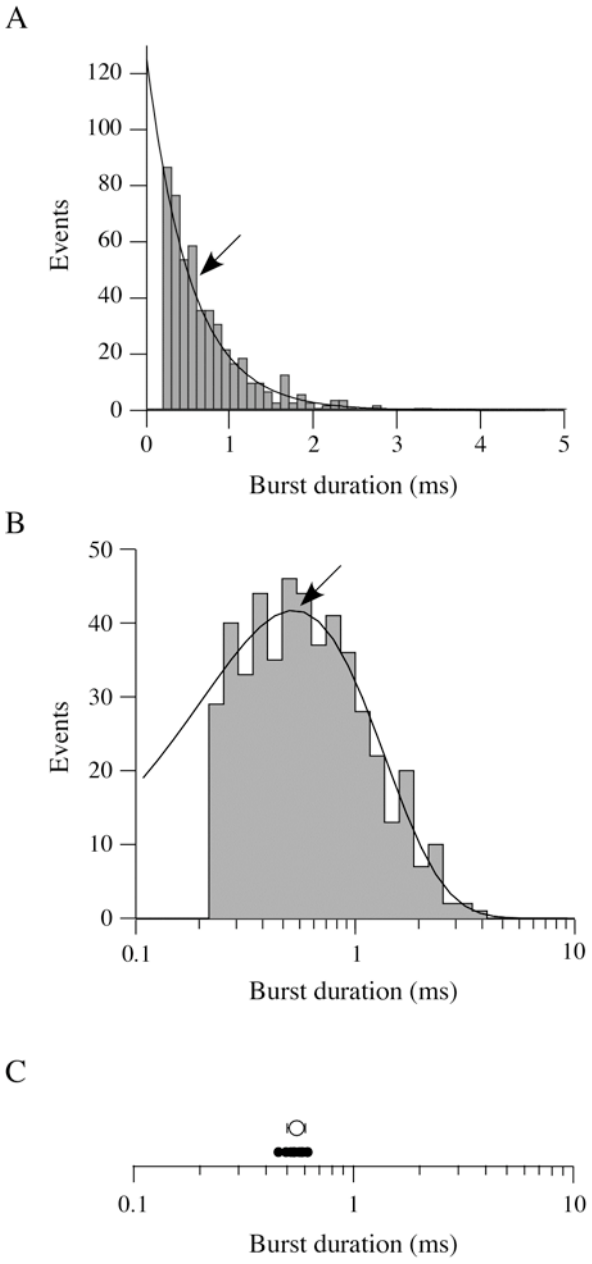
A
120
100
80
60
40
20
0
Events
0
1
2
3
4
5
Burst duration (ms)
B
50
40
30
20
10
0
Events
0.1
1
10
Burst duration (ms)
C
0.1
1
10
Burst duration (ms)

exhibited only the primary event class so it was straightforward to generate the burst duration distribution (Figure 4.2B). For cells that had both event classes, the burst duration analysis was restricted to one class at a time. For most patches the amplitude distributions were easily separable, but in the cases where the primary and secondary classes overlapped care was taken to exclude events within the region of overlap. The average burst duration at +50 mV applied potential for each recording (n=10) yielded an average burst time of 0.53 ± 0.06 ms (n=10) for the primary class (Figure 4.2C).

The burst duration of AChRs has been shown to exhibit a weak voltage-dependence. Due to variability in the resting potential of cells during on-cell recordings, a possible concern was that I was comparing the burst duration of recordings at different transmembrane potentials. My estimates indicated the standard deviation of V_{rest} was 8 mV, but the two most extreme V_{rest} value were, -90 and -68 mV. I was therefore comparing the burst duration of channels that were experiencing an estimated 20 mV difference in membrane potential. However, my analysis of the voltage-dependence of the fast muscle AChR presented later in this chapter indicated that the expected change in burst duration over a range of 20 mV was small (~10%), permitting burst duration data to be grouped by applied potential.

Characterization of the secondary ACh-activated event class of fast muscle

In addition to the primary amplitude class of fast muscle single-channel events, there were some events whose amplitude fell outside of the main distribution in 7 of 12 cells examined at +50 mV. These secondary events were always smaller than the primary amplitude class, and contributed an average of 7 ± 3% of the total number of

Figure 4.3: Properties of the secondary class of ACh-activated channels of fast muscle. A) Sample recording showing the two amplitude classes. Dashed lines indicate the open level of primary (black) and secondary (red) events. B) Amplitude histogram with Gaussian fit to primary event class (black) and secondary event class (red). Primary event class peak corresponds to 8.6 pA, and secondary event class peak corresponds to 6.5 pA. C) Scatter plot of secondary class conductance values for each recording (red filled circles), along with the overall mean ± SD (open red circles). The primary class conductance values are included for comparison, in black. D) Cumulative current-voltage relations for secondary (red circles) and primary (black circles) event classes. Linear fit corresponds to an average conductance of 68 pS for primary conductance (black) and 51 pS for the secondary conductance (red). E) Representative burst duration histogram for secondary class events. Single exponential fit indicates a mean burst duration of 1.5 ms, at an applied potential of +50 mV. The average burst duration values for 7 recordings (red filled circles) and overall mean burst duration ± SD (open circle) are indicated in the scatter plot below the histogram.

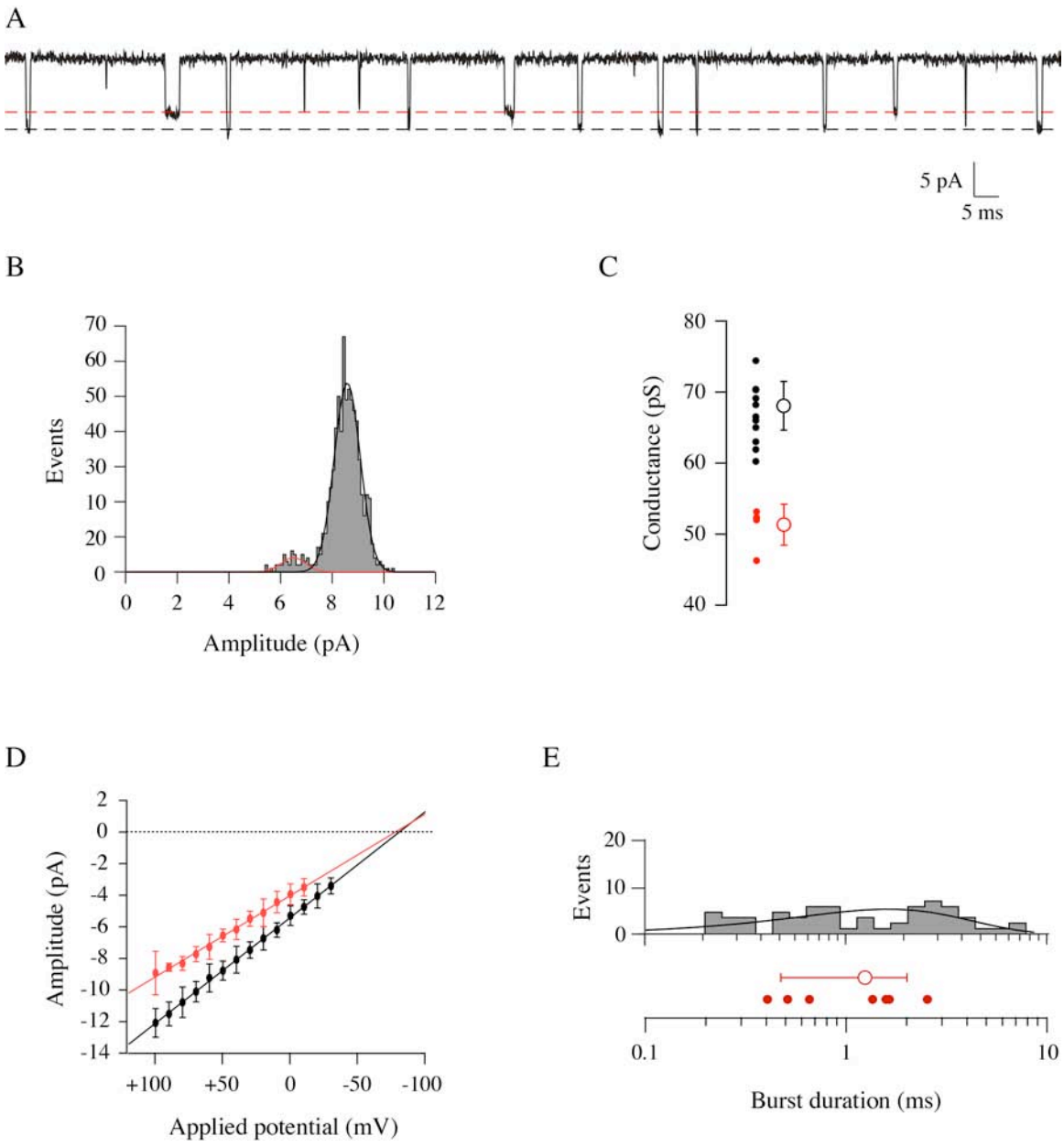
A
5 pA
5 ms
B
Events
Amplitude (pA)
C
Conductance (pS)
D
Amplitude (pA)
Applied potential (mV)
E
Events
Burst duration (ms)

openings. Figure 4.3A shows sample events from a recording where both event classes were present. The amplitude distribution was fit with two Gaussian functions, one corresponding to the primary class, and a second to the secondary amplitude class (Figure 4.3B). The contribution to the total number of events was determined by the weight of the fits. For the histogram shown, the principal class represented 94% of the total, and the secondary class represented 6%. Only five recordings provided enough secondary events to measure the amplitude at multiple potentials. The conductance values, determined by fitting the current-voltage relations of the secondary class in each recording, are shown in Figure 4.3C. The average single-channel conductance of the secondary event class was 51 ± 3 pS. The cumulative current-voltage plot of the average amplitude at each potential also indicated an average conductance of 53 pS (Figure 4.3D).

I also determined the burst duration of the secondary event class. The fit of the burst duration frequency histogram for the recording shown in Figure 4.3A indicated a mean burst duration of 1.5 ms (Figure 4.3E). The burst duration of the secondary class was fit at +50 mV in each recording where it was present, and the mean burst duration for each of the seven recordings is shown as a scatter plot below Figure 4.3E. The overall average burst duration for all cells was 1.2 ± 0.7 ms.

Characterization of the primary ACh-activated event class of slow muscle

The single channel properties of slow muscle AChRs were similarly examined. An example record from an on-cell recording of slow muscle is shown in Figure 4.4A. As seen in fast muscle, single channel events in slow muscle could be recorded at any

Figure 4.4: Properties of ACh-activated single-channel events of slow muscle. A) Sample single-channel openings from slow muscle at an applied potential of +50 mV. B) Amplitude histogram of all events recorded from example cell in A, fit to a Gaussian curve. C) Current-voltage relationship for the example recording in A and B, fit by linear regression (black). The slope conductance corresponds to 65 pS. Dashed line indicates zero current level. D) Current-voltage relationship for all 8 individual recordings, each with linear fits (black). E) On the left, a scatter plot indicates the conductance values for individual recordings (filled circles) alongside the mean conductance ± SD (open circle). On the right, a scatter plot indicates the estimated V_{rest} values for individual recordings (filled circles), alongside the mean V_{rest} ± SD (open circle). F) Cumulative current-voltage relationship with linear fit (black). The slope conductance corresponds to 66 pS.

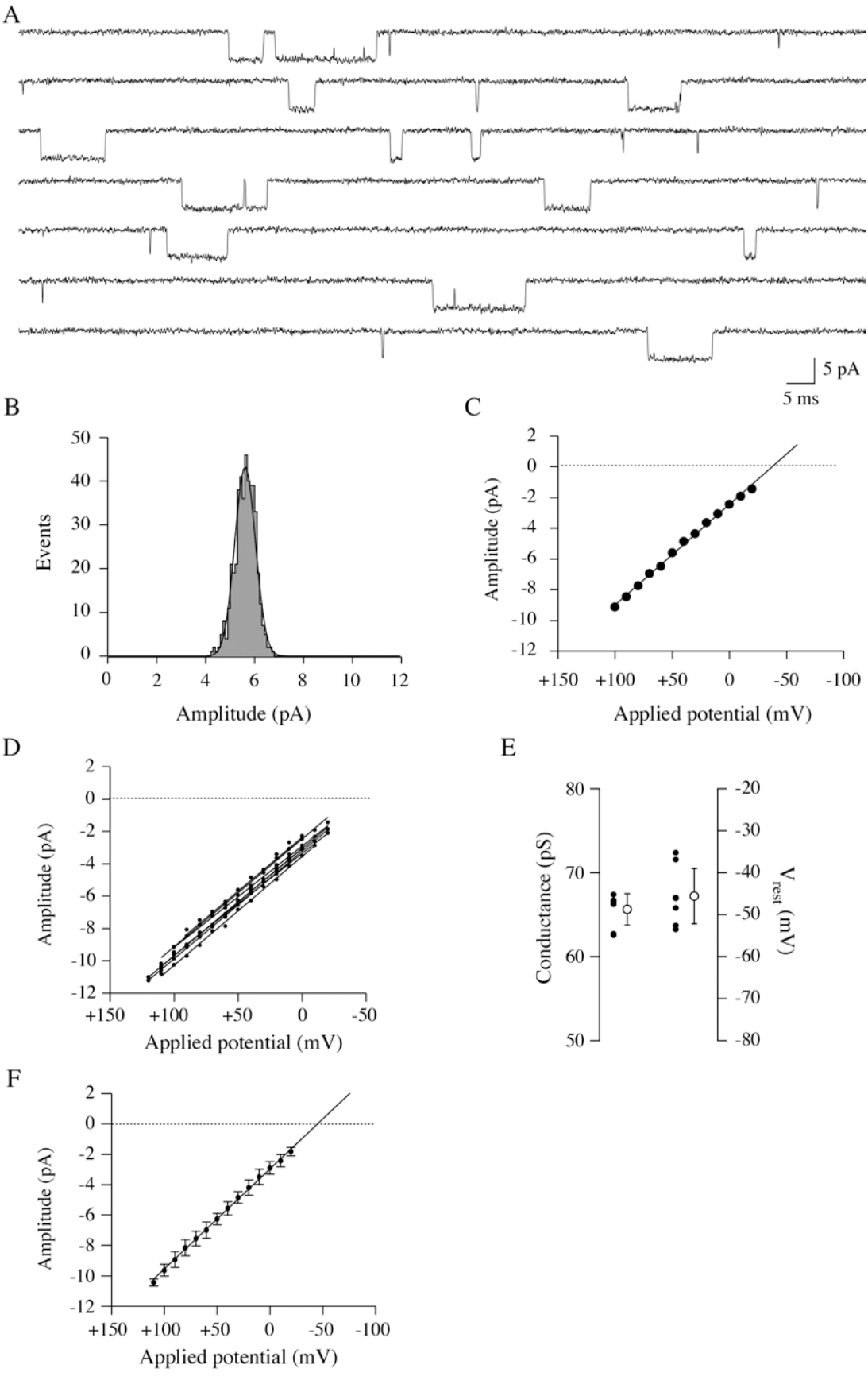
A
5 pA
5 ms
B
Events
Amplitude (pA)
C
Amplitude (pA)
Applied potential (mV)
D
Amplitude (pA)
Applied potential (mV)
E
Conductance (pS)
V rest (mV)
F
Amplitude (pA)
Applied potential (mV)

position along the muscle. At 300 nM ACh, qualitatively, the frequency of events appeared similar to that seen in fast muscle.

Most events in slow muscle represented a single amplitude class at an applied potential of +50 mV (Figure 4.4B). In 6 of 11 recordings at +50 mV there was an additional larger event class that contributed an average of 12 ± 9% to the total number of events. This secondary class will be described following the characterization of the primary event class.

The amplitude of the primary event class was determined as described for fast muscle, and the fit in Figure 4.4B indicated a mean amplitude of 5.8 pA, at +50 mV applied potential. Current-voltage plots constructed for the primary class were also fit by linear regression (Figure 4.4C). The slope of the fit to the sample patch indicated a conductance of 65 pS, and the x-intercept estimated the resting potential was -43 mV. The current-voltage relationship and linear fit are shown for each cell (n=8), in Figure 4.4D. In Figure 4.4E, the values for the conductance and the estimated V_{rest} determined for each recording are shown alongside their respective mean values. These values indicated that the slow muscle primary AChR class had an average conductance of 66 ± 2 pS, and the V_{rest} was estimated to be -46 ± 6.6 mV. The estimate of V_{rest} was considerably depolarized compared to fast muscle cells.

The primary class single-channel conductance was also estimated by constructing a cumulative current-voltage plot (Figure 4.4F). The cumulative data represented the average event amplitude for all recordings (n=8) at each applied potential. The linear fit to the cumulative data indicated that the slow muscle primary AChR class had an average conductance of 66 pS, and estimated V_{rest} of -45 mV.

The mean channel burst duration of the principal class on slow muscle was determined in the same manner as for fast muscle. As with fast muscle, when both the primary and secondary event classes were present, care was taken to construct duration histograms containing only events from one class. I used the double Gaussian fit to the amplitude histogram to estimate and exclude ambiguous events that could represent either class distribution.

Figure 4.5A shows a burst duration frequency histogram of the primary event class at +50 mV. The fit of the burst distribution required two exponents for all ten recordings. The two components corresponded to the long duration openings that were interlaced with extremely short duration openings (Figure 4.5A). On the semi-log plot, this double exponential distribution appeared as two peaks. The fit to the brief component indicated that the mean burst duration of these events was beyond my ability to measure (<200 μS), due to the limited frequency response of the electronics. Therefore, I could not be confident with the kinetic estimates or the contribution to the overall distribution.

The second component of the burst duration histogram, however, was well resolved. For the sample distribution shown, the fit indicated a mean burst duration of 4.3 ms at an applied potential of +50 mV. The overall mean duration of the second component was 3.5 ± 0.9 ms at an applied potential of +50 mV (Figure 4.5B, n=10 recordings).

Figure 4.5: Burst duration of the primary class of ACh-activated channels of slow muscle. A) Burst duration histogram for the example recording in Figure 4.4A, fit with a double exponential. The mean burst duration value was 0.11 ms for the brief component, and 4.3 ms for the slow component. B) The scatter plot indicates the mean burst duration values for both the brief (filled triangles) and slow components (filled circles) of the double exponential fit, for all 10 recordings. The overall mean burst duration ± SD for the slow component corresponds to 3.5 ± 0.9 ms (open circle).

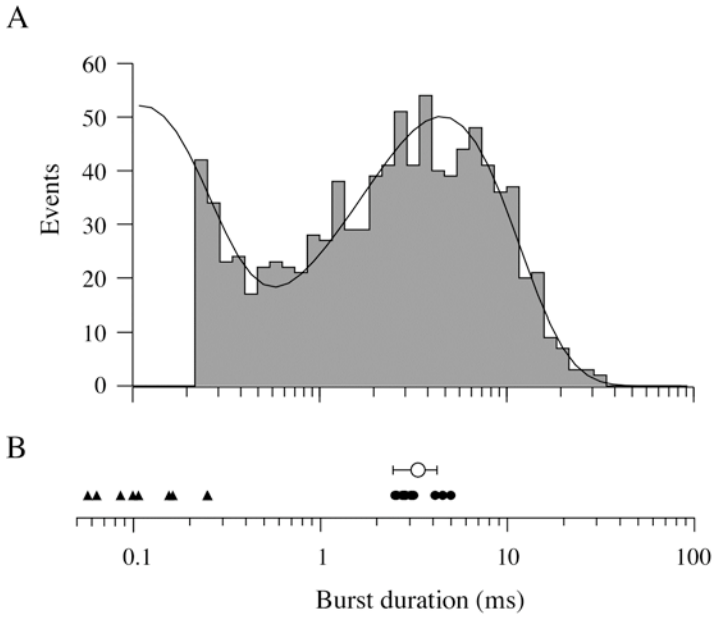
A
60
50
40
30
20
10
0
Events
B
0.1
1
10
100
Burst duration (ms)

Characterization of the secondary class of AChRs on slow muscle

The secondary class of events on slow muscle was present in 6 of 11 recordings at an applied potential of +50 mV. A sample trace that contained events of both the principal and secondary classes is shown in Figure 4.6A. Unlike fast muscle, the secondary class of events in slow muscle was slightly larger in amplitude than the principal class, and appeared as a right shoulder in the amplitude distribution (Figure 4.6B). A dual Gaussian fit to both distributions estimated the overlap and amplitude for each class at each potential. Using the estimated peak amplitudes, current-voltage plots were constructed and fit by linear regression for 5 recordings where the secondary class was present at multiple applied potentials. The average single-channel conductance of the secondary class was 70 ± 4 pS (Figure 4.6C). A cumulative current-voltage plot was constructed from the averaged amplitude at each potential (Figure 4.6D); the slope of the cumulative data indicated a single-channel conductance of 72 pS for the secondary event class.

In each recording, the secondary event class estimates of V_{rest} were more hyperpolarized than the primary class estimates (-49 ± 4 mV primary, -61 ± 6 mV secondary). As shown in the cumulative current-voltage relationship (Figure 4.6D), the two classes of AChRs on slow muscle do not extrapolate to the same x-intercept. However, both events were recorded in the same patch, rendering differences in V_{rest} impossible. The answer lies in the non-linear current-voltage relations of the primary class. This property of the primary AChR class of slow muscle will be fully addressed in Chapter 6, which deals with rectification.

Figure 4.6: Properties of the secondary class of ACh-activated events of slow muscle. A) Sample recording showing the two amplitude classes. Dashed line indicates the open level of primary (black) and secondary (red) events. B) Amplitude histogram with the Gaussian fits to the primary event class (black) and secondary event class (red). Fit to primary peak corresponds to 6.0 pA, and fit to secondary peak corresponds to 7.2 pA. C) Scatter plot of secondary event class conductance values for each of 5 recordings (red filled circles), and mean conductance value ± SD (red open circle). Primary event class conductance values (black) are included for comparison. D) Cumulative current-voltage relations for secondary (red) and primary (black) event classes. Linear fit indicates an average secondary class conductance of 72 pS. E) Example burst duration histogram for secondary class events. Scatter plot below histogram indicates mean burst duration determined for each recording (filled circles), and average burst duration ± SD (open circles).

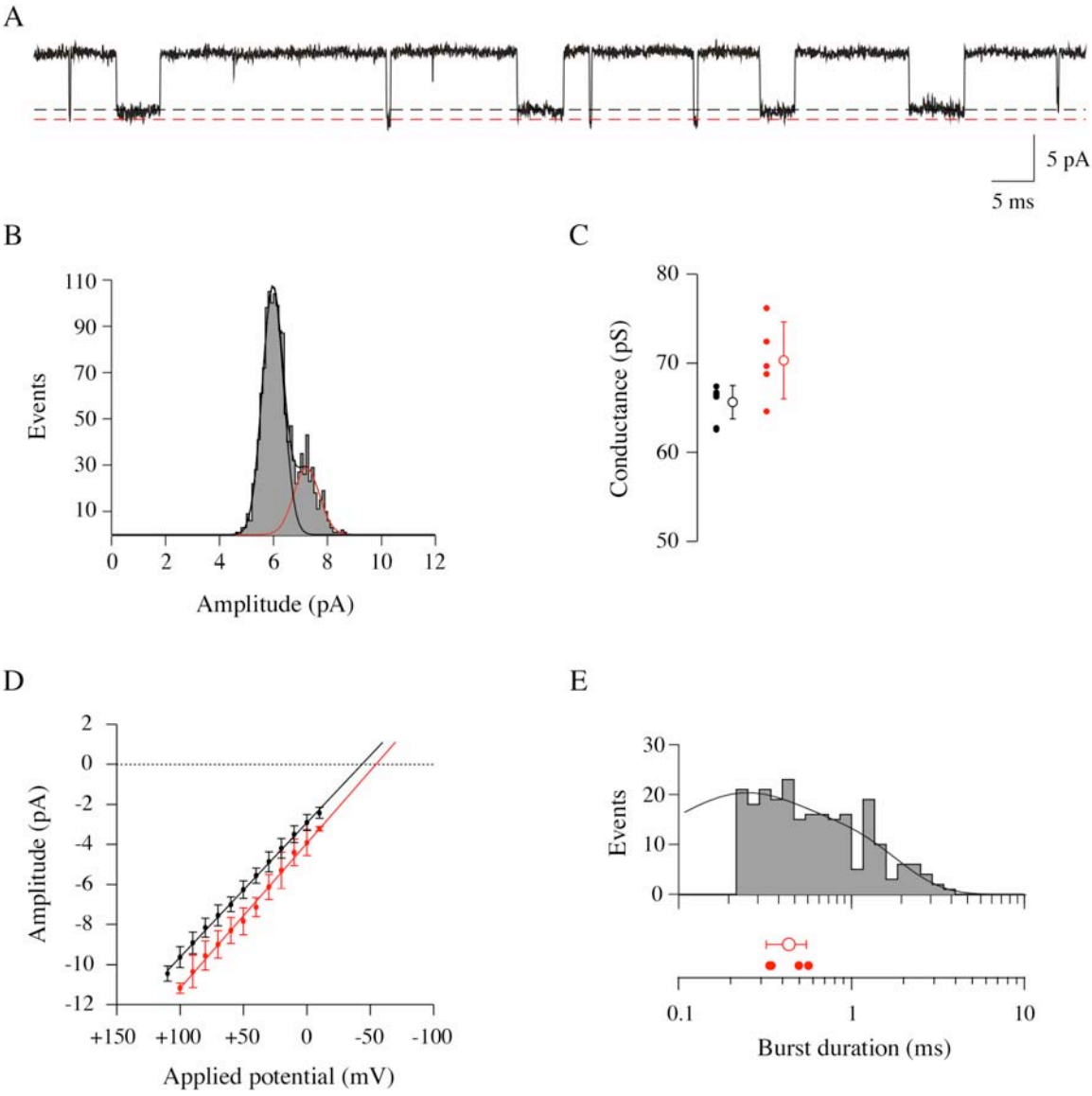
A
5 pA
5 ms
B
Events
110
90
70
50
30
10
0
2
4
6
8
10
12
Amplitude (pA)
C
Conductance (pS)
80
70
60
50
D
Amplitude (pA)
2
0
-2
-4
-6
-8
-10
-12
+150
+100
+50
0
-50
-100
Applied potential (mV)
E
Events
30
20
10
0
0.1
1
10
Burst duration (ms)

Burst duration histograms were also constructed for the secondary class of events on slow muscle (Figure 4.6E). The fit of the secondary class burst duration distributions only required a single exponent. Four of 6 recordings at + 50 mV had enough events to estimate the mean burst duration, and the average burst duration for all recordings was 0.43 ± 0.1 ms. Overall, the characteristics of the secondary AChR class of slow muscle are similar to those of the primary class of fast muscle.

Comparison of fast and slow muscle burst duration to synaptic current decay

Characterization of the single-channel properties of AChRs of slow and fast muscle was undertaken to determine if differences in burst duration could account for the differences in τ_{decay}. The average values for fast and slow muscle AChRs indicated a six-fold difference in average burst duration (0.53 ms vs. 3.3 ms). Comparison of the τ_{decay} values of the synaptic currents, and the mean burst duration values of the AChRs for both muscle types (Figure 4.7) indicated that the difference in τ_{decay} between fast and slow muscle synaptic current could be attributed to differences in the AChR burst duration.

Voltage-dependence of the mean burst duration of fast and slow primary AChRs

A further functional signature for AChRs is the weak dependence of the burst duration on membrane voltage. Prior to the advent of single-channel recording, it was determined that the decay of synaptic currents exhibited an exponential dependence on membrane voltage (Takeuchi and Takeuchi, 1959; Kordas, 1969; Magleby and Stevens, 1972). Through noise analysis studies, this macroscopic current dependence on membrane voltage was assigned to the voltage influence on the burst duration of the

Figure 4.7: Comparison of synaptic current and single-channel kinetics of slow and fast muscle. τ_{decay} values of muscle synaptic events at -90 mV, compared to burst duration values of muscle AChRs at +50 mV applied potential. Individual cell (τ_{decay}) or patch (AChR burst duration) values are indicated with filled circles, alongside mean values ± SD indicated with open circles.

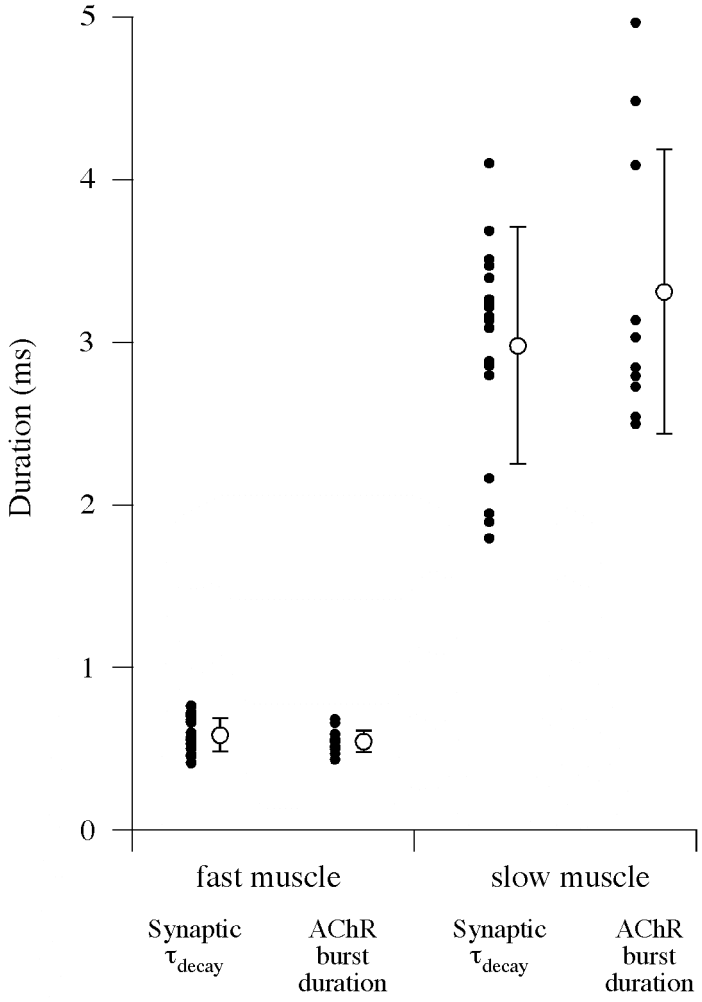
Duration (ms)
5
4
3
2
1
0
fast muscle
slow muscle
Synaptic τdecay
AChR burst duration
Synaptic τdecay
AChR burst duration

AChR (Magleby and Stevens, 1972). Studies comparing fast and slow muscle indicated differences in the voltage-dependence of the synaptic currents between cell types (Federov et al, 1982; Dionne and Parsons, 1981), but not in every preparation (Miledi and Uchitel 1981; Uchitel and Miledi, 1987). Thus, it seemed worthwhile to examine both the fast and slow muscle AChR burst duration dependence on membrane voltage.

I analyzed the average burst duration of the primary event class of slow and fast muscle over a range of applied potentials between +130 and -30. A plot of the mean burst duration vs. the applied potential for all fast muscle recordings is shown in Figure 4.8A. For fast AChRs, the plot of the burst duration versus applied voltage was generally better fit by an exponential function than a linear function. This was apparent in both visual inspection of the fits and in the R^2 value. The average R^2 value associated with an exponential fit was 0.85; the same data fit by linear regression had an average R^2 value of 0.80. This relationship predicted an e-fold increase in burst duration occurred with every 108 ± 30 mV of hyperpolarization.

A cumulative plot was constructed from the average burst duration of all recordings (Figure 4.8B). The exponential fit to the cumulative data indicated an e-fold increase in burst duration with every 122 mV hyperpolarization. The cumulative data plot was also best described by an exponential function (R^2=0.97 for exponential; R^2=0.90 for linear).

Similar analysis was performed for the primary event class on slow muscle. The scatter plot in Figure 4.8C indicates the burst duration at each applied potential, for all slow muscle recordings (n=9). Unlike fast muscle, the individual plots were equally described by linear (R^2=0.51) and exponential fits (R^2=0.50). A cumulative burst

Figure 4.8. Voltage-dependence of muscle AChR burst duration. A) Mean burst duration for each recording of fast muscle primary events (filled circles, n=7 recordings) at each potential, shown with their respective exponential fits. B) Cumulative burst duration-voltage plot constructed from cells in A. Exponential fit (black) indicates e-fold change in burst duration per 122 mV. Linear fit shown in red, for comparison. C) Mean burst duration for each recording of slow muscle primary events (filled circles, n=9 recordings), shown with their respective exponential fits. D) Cumulative plot constructed from recordings in C. E) Cumulative plot from D, restricted to positive applied potentials between +130 and +10 mV. Exponential fit indicates e-fold change in burst duration per 263 mV. Linear fit shown in red, for comparison.

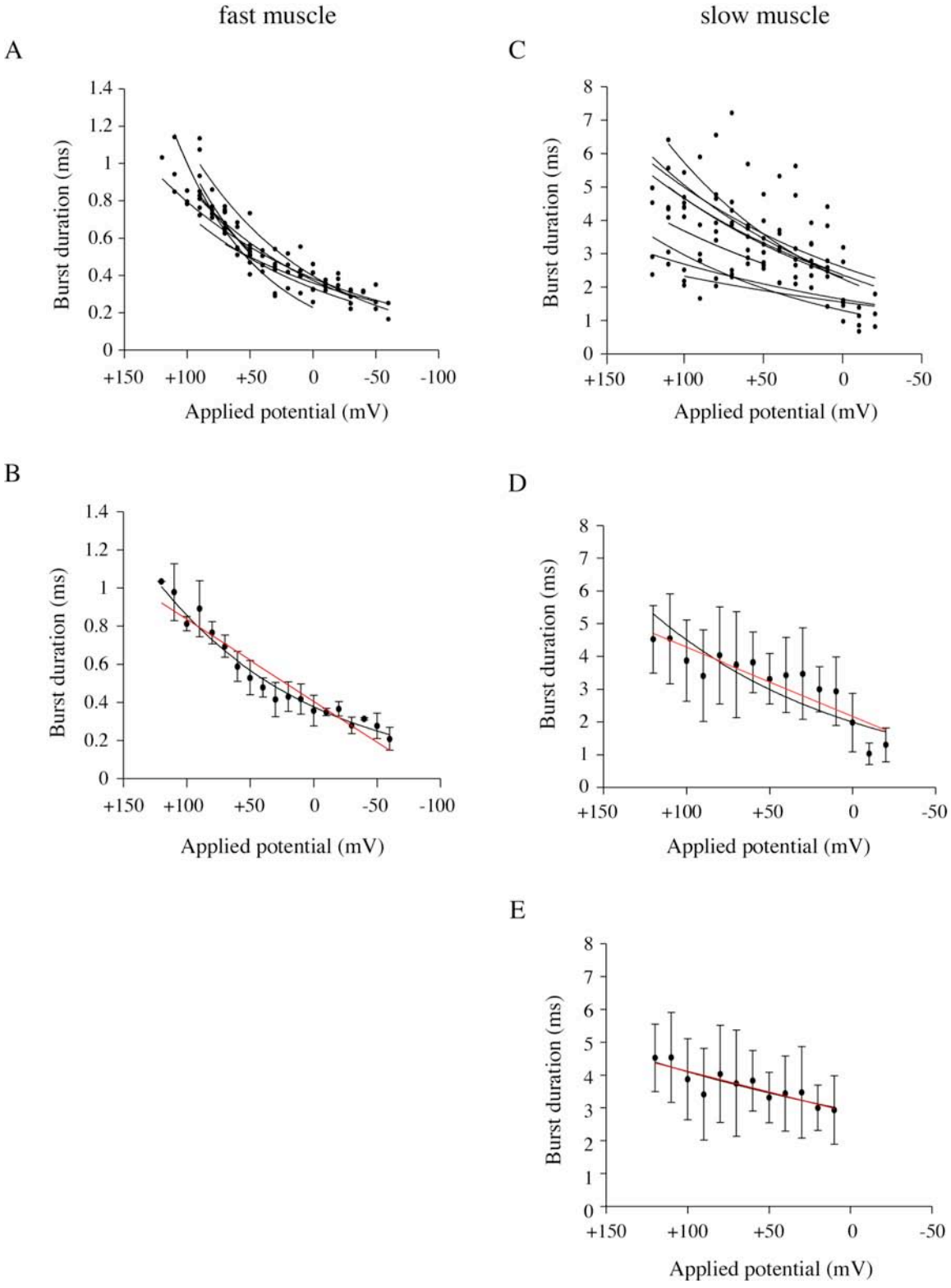
fast muscle
slow muscle
A
B
C
D
E
Burst duration (ms)
Applied potential (mV)
+150
+100
+50
0
-50
-100

duration versus applied voltage plot was also constructed (Figure 4.8D), and was better described by a linear (R^2=0.8) rather than an exponential fit (R^2=0.68).

Qualitative inspection of the cumulative plot in Figure 4.8D suggested that the burst duration remained relatively constant over hyperpolarizing applied potentials, then decreased rapidly over the three most depolarized potentials. To determine if a better fit could be obtained, I excluded the most depolarized holding potentials. An exponential fit to the range of potentials between -150 and -10 mV was improved visually, and provided an R^2 value of 0.9 (Figure 4.8E). However, both exponential and linear trend lines still described the cumulative data equally well over the hyperpolarized range (R^2=0.9, both fits). The fit in Figure 4.8E indicated that an average e-fold increase in burst duration of the slow muscle occurred with every 263 mV hyperpolarization.

For consistency, I also examined the fast muscle cumulative burst duration plot over the restricted range of applied potentials (-150 to -10). The fit over the hyperpolarized range was similar to the entire range: the data was still best described by an exponential fit (R^2=0.96), and the e-fold change in burst duration was 109 mV. These results suggested that, compared to the fast muscle AChR, the burst duration of the slow muscle AChR is only weakly dependent on voltage.

Summary of results from Chapter 3 and Chapter 4

Table 4.1 summarizes the characteristics of the single-channel events on both slow and fast muscle. The characteristics of the synaptic events determined in Chapter 3 are included for reference. Blank areas represent characteristics that will be determined in the remaining Chapters.

Table 4.1: Summary of results from Chapters 3 through 4.

Source	Type	Representation (total events or amplitude)	Conductance	Kinetics (τ_{decay} or burst duration)	Voltage-dependence	
					Burst duration	Conductance
muscle synaptic events	fast	100%	-	brief (~0.5 ms)	-	
	slow	80-100%	-	long (~3 ms)	-	
muscle single channels	fast	90-100%	68 ± 4 pS	brief (~0.5 ms)	exponential	
	slow	80-100%	66 ± 2 pS	long (~3.5 ms)	atypical	
muscle single channels secondary class	fast	0-12%	51 ± 3 pS	intermediate (~1.2 ms)	-	
	slow	0-23%	70 ± 4 pS	brief (~0.5 ms)	-	
reconstituted single channels						
MO muscle synaptic events	ε					
	γ					

CHAPTER 5

Reconstituted zebrafish AChR characteristics

Zebrafish AChR subunit identification

I have established that the difference in the decay time of slow and fast muscle cells is due to differences in the AChR burst duration. The burst duration of AChRs is determined, in part, by the subunit composition; regulation of receptor subunit composition is a mechanism by which synaptic current decay is modulated in developing fast muscle synapses (Mishina et al, 1986). To determine if differences in subunit composition accounted for the burst duration difference between fast and slow muscle AChRs, it was necessary to identify and reconstitute the zebrafish muscle AChR subunits for single-channel analysis.

In zebrafish, only the α and δ subunit mRNA sequences have been reported (Sepich et al, 1998; Ono et al, 2004). Our collaborators, Drs. Fumihito Ono and Jason Urban (NIAAA) cloned the remaining subunit cDNAs. Zebrafish also express a homolog of the β subunit termed β1a. This subunit is also encoded in the genome of two other teleost fish, and likely represents a gene duplication event (Jones et al, 2003).

Because this is the first report identifying the muscle AChR subunits in zebrafish, I have included the predicted protein sequences of each subunit aligned with the sequences of other vertebrate species (Figure 5.1 – Figure 5.7).

Figure 5.1: Primary amino acid sequence alignment of the zebrafish α subunit. Identical residues unshaded, conserved residues in light grey, and different residues in dark grey.

```
zebrafish α    1 MNYFILILPILPYLYGPAVCSEDETRLVKTLFTGYNKVVRPVSHFKDPVV
frog α         1 MDYTASCLIFLFIAAGTVFGTDHETRLIGDLFANYNKVVRPVETYKDQVV
mouse α        1 MELSTVLLLLGLCSAGLVLGSEHETRLVAKLFEDYSSVVRPVEDHREIVQ
consensus      1 Mdyt-liLiil---aG-vvgsehETRLvg-LF--YnkVVRPVe-fkd-Vv

zebrafish α   51 VTVGLQLIQLISVDEVNQIVTSNVRLKQQWKDVHLQWNPDDYGGIRKIRI
frog α        51 VTVGLQLIQLINVDEVNQIVSTNIRLKQQWRDVNLKWDPAKYGGVKKIRI
mouse α       51 VTVGLQLIQLINVDEVNQIVTTNVRLKQQWVDYNLKWNPDDYGGVKKIHI
consensus     51 VTVGLQLIQLInVDEVNQIVttNvRLKQQWkDvnLkWnPddYGGvkKIrI

zebrafish α  101 PSTDLWKPDLVLYNNADGDFAIVHETKVLLEHTGMITWTPPAIFKSYCEI
frog α       101 PSSDVWSPDLVLYNNADGDFAISKDTKILLEYTGKITWTPPAIFKSYCEI
mouse α      101 PSEKIWRPDVVLYNNADGDFAIVKFTKVLLDYTGHITWTPPAIFKSYCEI
consensus    101 PStdlWkPDlVLYNNADGDFAIvkeTKvLLeyTG-ITWTPPAIFKSYCEI

zebrafish α  151 VVLHFPFDLQNCSMKLGTWTYDGNLVIINPDSDRPDLSNFMESGEWVMKD
frog α       151 IVTYFPFDQQNCSMKFGTWTYDGSLLVINPERDRPDLSNFMASGEWMMKD
mouse α      151 IVTHFPFDEQNCSMKLGTWTYDGSVVAINPESDQPDLSNFMESGEWVIKE
consensus    151 iVthFPFD-QNCSMKlGTWTYDGslviINPesDrPDLSNFMeSGEWvmKd

zebrafish α  201 YRSWKHWVYYACCPDTPYLDITYHFLLLRLPLYFIVNVIIPCMLFSFLTG
frog α       201 YRCWKHWVYYTCCPDKPYLDITYHFVLQRLPLYFIVNVIIPCLLFSFLTG
mouse α      201 ARGWKHWVFYSCCPTTPYLDITYHFVMQRLPLYFIVNVIIPCLLFSFLTS
consensus    201 yR-WKHWVyYtCCPdtPYLDITYHFvlqRLPLYFIVNVIIPClLFSFLTg

zebrafish α  251 LVFYLPTDSGEKMTLSISVLLSLTVFLLVIVELIPSTSSAVPLIGKYMLF
frog α       251 LVFYLPTDSGEKMTLSISVLLSLTVFLLVIVELIPSTSSAVPLIGKYMLF
mouse α      251 LVFYLPTDSGEKMTLSISVLLSLTVFLLVIVELIPSTSSAVPLIGKYMLF
consensus    251 LVFYLPTDSGEKMTLSISVLLSLTVFLLVIVELIPSTSSAVPLIGKYMLF

zebrafish α  301 TMIFVIASIIITVIVINTHHRSPSTHIMPAWVRKIFIDTIPNMMFFSTMK
frog α       301 TMVFVIASIIITVIVINTHHRSPSTHTMPPWVRKIFIETIPNIMFFSTMK
mouse α      301 TMVFVIASIIITVIVINTHHRSPSTHIMPEWVRKVFIDTIPNIMFFSTMK
consensus    301 TMvFVIASIIITVIVINTHHRSPSTHiMP-WVRKiFIdTIPNiMFFSTMK

zebrafish α  351 RPSQERQEKRLFPADFDISDISGKPMPASVTYHSPITKNPDVRSAIEGVK
frog α       351 RPSQEKQPQKTFAEEMDISHISGKLGPAAVTYQSPALKNPDVKSAIEGIK
mouse α      351 RPSRDKQEKRIFTEDIDISDISGKPGPPPMGFHSPLIKHPEVKSAIEGVK
consensus    351 RPSqekQekrlF-edmDISdISGKpgPa-vtyhSPilKnPdVkSAIEGvK

zebrafish α  401 YIADTMKSDEESNNAAEEWKFVAMVLDHILLCVFMAVCIIGTLGVFAGRL
frog α       401 YIAETMKSDQESNKASEEWKFVAMVLDHILLAVFMTVCVIGTLAVFAGRI
mouse α      401 YIAETMKSDQESNNAAEEWKYVAMVMDHILLGVFMLVCLIGTLAVFAGRL
consensus    401 YIAeTMKSDqESNnAaEEWKfVAMVlDHILLaVFM-VCiIGTLaVFAGRl

zebrafish α  451 IELSML-
frog α       451 IEMNMQE
mouse α      451 IELHQQG
consensus    451 IEl-mq-
```

Figure 5.2: Primary amino acid sequence alignment of the zebrafish β subunit. Identical residues unshaded, conserved residues in light grey, and different residues in dark grey.

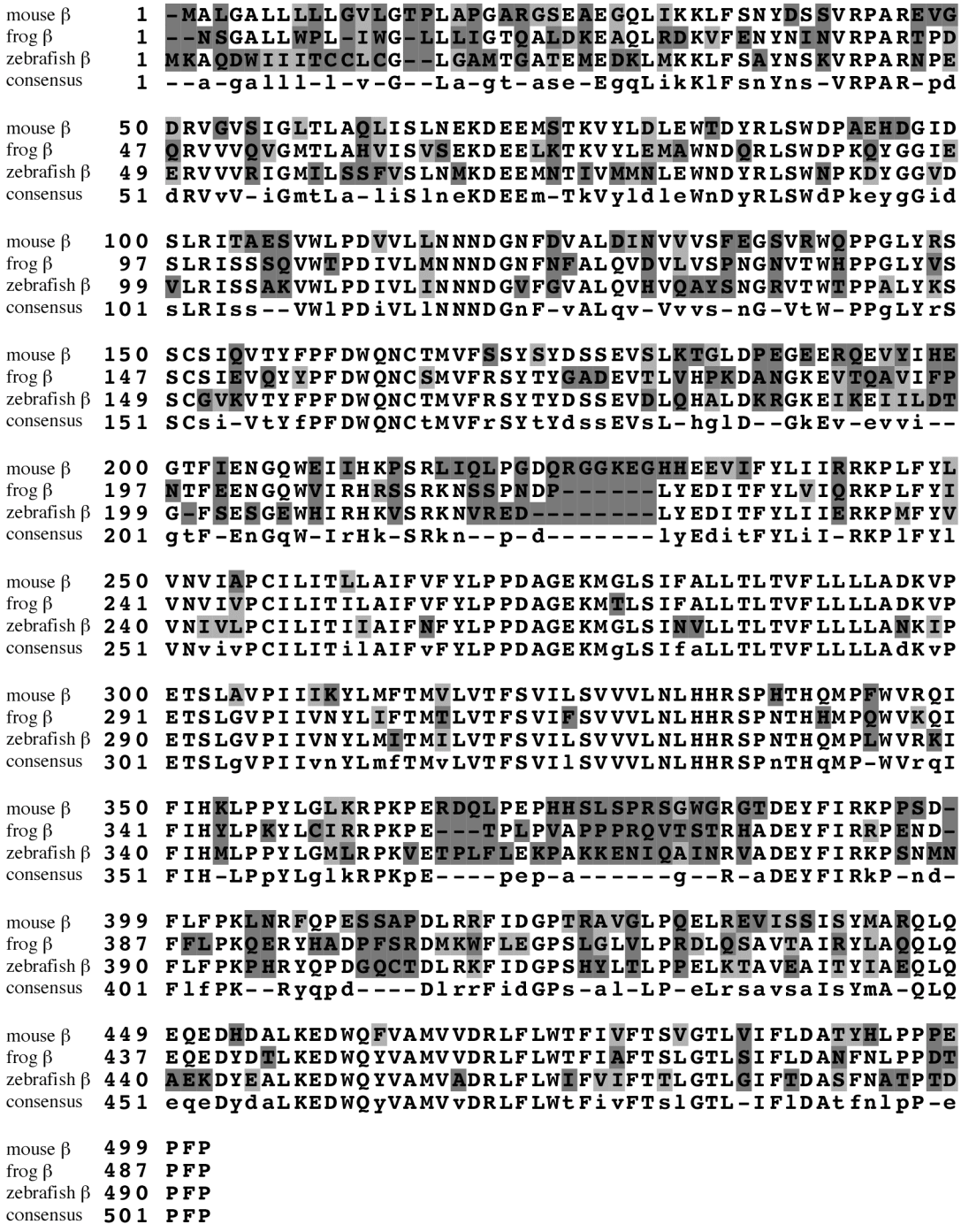
mouse β 1 -MALGALLLLLGVLGTPLAPGARGSEAEGQLIKKLFSNYDSSVRPAREVG
frog β 1 --NSGALLWPL-IWG-LLLIGTQALDKEAQLRDKVFENYNINVRPARTPD
zebrafish β 1 MKAQDWIIITCCLCG--LGAMTGATEMEDKLMKKLFSAYNSKVRPARNPE
consensus 1 --a-galll-l-v-G--La-gt-ase-EgqLikKlFsnYns-VRPAR-pd
mouse β 50 DRVGVSIGLTLAQLISLNEKDEEMSTKVYLDLEWTDYRLSWDPAEHDGID
frog β 47 QRVVVQVGMTLAHVISVSEKDEELKTKVYLEMAWNDQRLSWDPKQYGGIE
zebrafish β 49 ERVVVRIGMILSSFVSLNMKDEEMNTIVMMNLEWNDYRLSWNPKDYGGVD
consensus 51 dRVvV-iGmtLa-liSlneKDEEm-TkVyldleWnDyRLSWdPkeygGid
mouse β 100 SLRITAESVWLPDVVLLNNNDGNFDVALDINVVVSFEGSVRWQPPGLYRS
frog β 97 SLRISSSQVWTPDIVLMNNNDGNFNFALQVDVLVSPNGNVTWHPPGLYVS
zebrafish β 99 VLRISSAKVWLPDIVLINNNDGVFGVALQVHVQAYSNGRVTWTPPALYKS
consensus 101 sLRIss--VWlPDiVLlNNNDGnF-vALqv-Vvvs-nG-VtW-PPgLYrS
mouse β 150 SCSIQVTYFPFDWQNCTMVFSSYSYDSSEVSLKTGLDPEGEERQEVYIHE
frog β 147 SCSIEVQYYPFDWQNCSMVFRSYTYGADEVTLVHPKDANGKEVTQAVIFP
zebrafish β 149 SCGVKVTYFPFDWQNCTMVFRSYTYDSSEVDLQHALDKRGKEIKEIILDT
consensus 151 SCsi-VtYfPFDWQNCtMVFrSYtYdssEVsL-hglD--GkEv-evvi--
mouse β 200 GTFIENGQWEIIHKPSRLIQLPGDQRGGKEGHHEEVIFYLIIRRKPLFYL
frog β 197 NTFEENGQWVIRHRSSRKNSSPNDP------LYEDITFYLVIQRKPLFYI
zebrafish β 199 G-FSESGEWHIRHKVSRKNVRED--------LYEDITFYLIIERKPMFYV
consensus 201 gtF-EnGqW-IrHk-SRkn--p-d-------lyEditFYLiI-RKPlFYl
mouse β 250 VNVIAPCILITLLAIFVFYLPPDAGEKMGLSIFALLTLTVFLLLLADKVP
frog β 241 VNVIVPCILITILAIFVFYLPPDAGEKMTLSIFALLTLTVFLLLLADKVP
zebrafish β 240 VNIVLPCILITIIAIFNFYLPPDAGEKMGLSINVLLTLTVFLLLLANKIP
consensus 251 VNvivPCILITilAIFvFYLPPDAGEKMgLSIfaLLTLTVFLLLLAdKvP
mouse β 300 ETSLAVPIIIKYLMFTMVLVTFSVILSVVVLNLHHRSPHTHQMPFWVRQI
frog β 291 ETSLGVPIIVNYLIFTMTLVTFSVIFSVVVLNLHHRSPNTHHMPQWVKQI
zebrafish β 290 ETSLGVPIIVNYLMITMILVTFSVILSVVVLNLHHRSPNTHQMPLWVRKI
consensus 301 ETSLgVPIIvnYLmfTMvLVTFSVIlSVVVLNLHHRSPnTHqMP-WVrqI
mouse β 350 FIHKLPPYLGLKRPKPERDQLPEPHHSLSPRSGWGRGTDEYFIRKPPSD-
frog β 341 FIHYLPKYLCIRRPKPE---TPLPVAPPPRQVTSTRHADEYFIRRPENDE
zebrafish β 340 FIHMLPPYLGMLRPKVETPLFLEKPAKKENIQAINRVADEYFIRKPSNMN
consensus 351 FIH-LPpYLglkRPKpE----pep-a------g--R-aDEYFIRkP-nd-
mouse β 399 FLFPKLNRFQPESSAPDLRRFIDGPTRAVGLPQELREVISSISYMARQLQ
frog β 387 FFLPKQERYHADPFSRDMKWFLEGPSLGLVLPRDLQSAVTAIRYLAQQLQ
zebrafish β 390 FLFPKPHRYQPDGQCTDLRKFIDGPSHYLTLPPELKTAVEAITYIAEQLQ
consensus 401 FlfPK--Ryqpd----DlrrFidGPs-al-LP-eLrsavsaIsYmA-QLQ
mouse β 449 EQEDHDALKEDWQFVAMVVDRLFLWTFIVFTSVGTLVIFLDATYHLPPPE
frog β 437 EQEDYDTLKEDWQYVAMVVDRLFLWTFIAFTSLGTLSIFLDANFNLPPDT
zebrafish β 440 AEKDYEALKEDWQYVAMVADRLFLWIFVIFTTLGTLGIFTDASFNATPTD
consensus 451 eqeDydaLKEDWQyVAMVvDRLFLWtFivFTslGTL-IFlDAtfnlpP-e
mouse β 499 PFP
frog β 487 PFP
zebrafish β 490 PFP
consensus 501 PFP

Figure 5.3: Primary amino acid sequence alignment of the zebrafish β1a subunit. Identical residues unshaded, conserved residues in light grey, and different residues in dark grey.

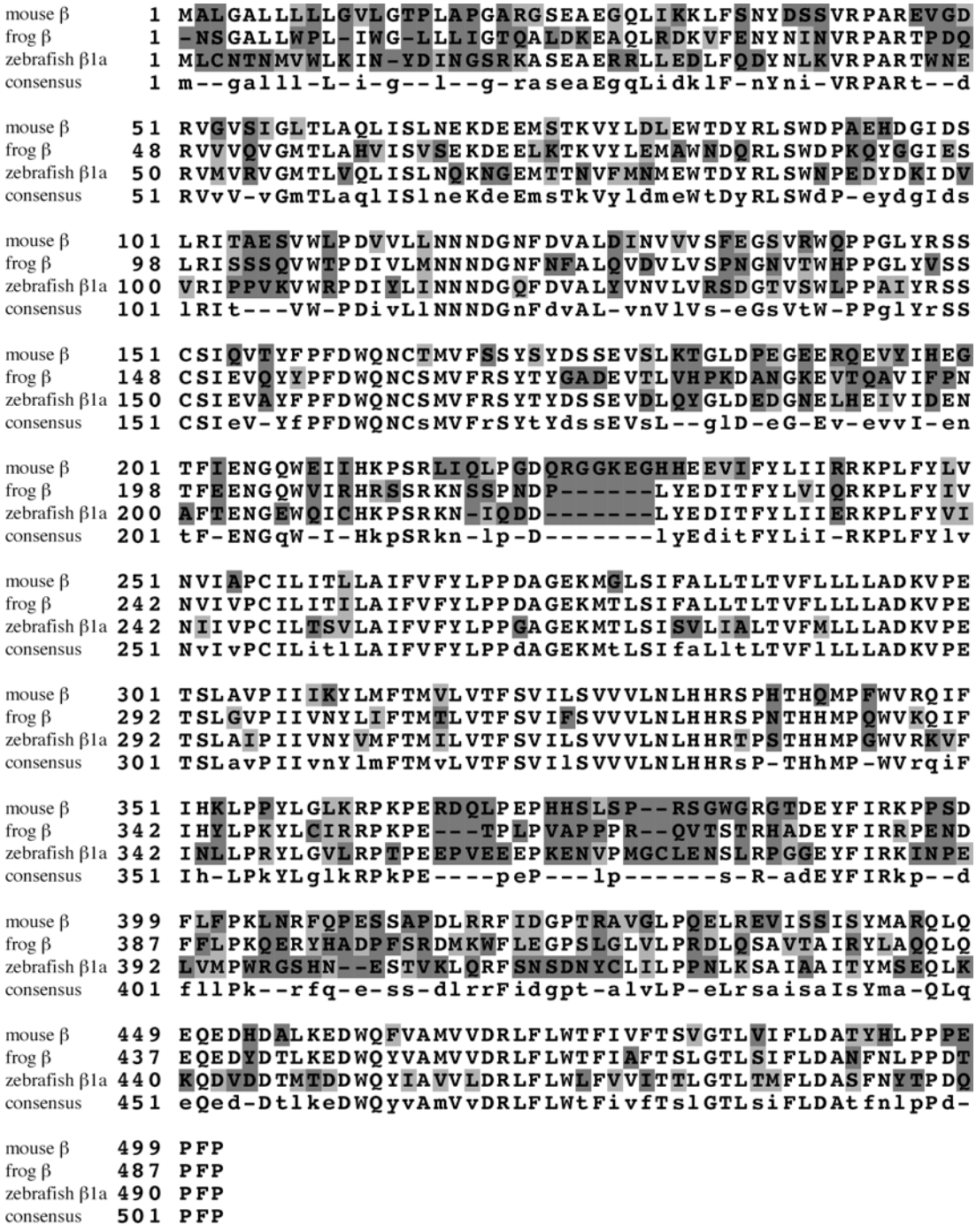
mouse β 1 MALGALLLLLGVLGTPLAPGARGSEAEGQLIKKLFSNYDSSVRPAREVGD
frog β 1 -NSGALLWPL-IWG-LLLIGTQALDKEAQLRDKVFENYNINVRPARTPDQ
zebrafish β1a 1 MLCNTNMVWLKIN-YDINGSRKASEAERRLLEDLFQDYNLKVRPARTWNE
consensus 1 m--galll-L-i-g--l--g-raseaEgqLidklF-nYni-VRPARt--d
mouse β 51 RVGVSIGLTLAQLISLNEKDEEMSTKVYLDLEWTDYRLSWDPAEHDGIDS
frog β 48 RVVVQVGMTLAHVISVSEKDEELKTKVYLEMAWNDQRLSWDPKQYGGIES
zebrafish β1a 50 RVMVRVGMTLVQLISLNQKNGEMTTNVFMNMEWTDYRLSWNPEDYDKIDV
consensus 51 RVvV-vGmTLaqlISlneKdeEmsTkVyldmeWtDyRLSWdP-eydgIds
mouse β 101 LRITAESVWLPDVVLLNNNDGNFDVALDINVVVSFEGSVRWQPPGLYRSS
frog β 98 LRISSSQVWTPDIVLMNNNDGNFNFALQVDVLVSPNGNVTWHPPGLYVSS
zebrafish β1a 100 VRIPPVKVWRPDIYLINNNDGQFDVALYVNVLVRSDGTVSWLPPAIYRSS
consensus 101 lRIt---VW-PDivLlNNNDGnFdvAL-vnVlVs-eGsVtW-PPglYrSS
mouse β 151 CSIQVTYFPFDWQNCTMVFSSYSYDSSEVSLKTGLDPEGEERQEVYIHEG
frog β 148 CSIEVQYYPFDWQNCSMVFRSYTYGADEVTLVHPKDANGKEVTQAVIFPN
zebrafish β1a 150 CSIEVAYFPFDWQNCSMVFRSYTYDSSEVDLQYGLDEDGNELHEIVIDEN
consensus 151 CSIeV-YfPFDWQNCsMVFrSYtYdssEVsL--glD-eG-Ev-evvI-en
mouse β 201 TFIENGQWEIIHKPSRLIQLPGDQRGGKEGHHEEVIFYLIIRRKPLFYLV
frog β 198 TFEENGQWVIRHRSSRKNSSPNDP------LYEDITFYLVIQRKPLFYIV
zebrafish β1a 200 AFTENGEWQICHKPSRKN-IQDD-------LYEDITFYLIIERKPLFYVI
consensus 201 tF-ENGqW-I-HkpSRkn-lp-D-------lyEditFYLiI-RKPLFYlv
mouse β 251 NVIAPCILITLLAIFVFYLPPDAGEKMGLSIFALLTLTVFLLLLADKVPE
frog β 242 NVIVPCILITILAIFVFYLPPDAGEKMTLSIFALLTLTVFLLLLADKVPE
zebrafish β1a 242 NIIVPCILTSVLAIFVFYLPPGAGEKMTLSISVLIALTVFMLLLADKVPE
consensus 251 NvIvPCILitlLAIFVFYLPPdAGEKMtLSIfaLltLTVFlLLLADKVPE
mouse β 301 TSLAVPIIIKYLMFTMVLVTFSVILSVVVLNLHHRSPHTHQMPFWVRQIF
frog β 292 TSLGVPIIVNYLIFTMTLVTFSVIFSVVVLNLHHRSPNTHHMPQWVKQIF
zebrafish β1a 292 TSLAIPIIVNYVMFTMILVTFSVILSVVVLNLHHRTPSTHHMPGWVRKVF
consensus 301 TSLavPIIvnYlmFTMvLVTFSVIlSVVVLNLHHRsP-THhMP-WVrqiF
mouse β 351 IHKLPPYLGLKRPKPERDQLPEPHHSLSP--RSGWGRGTDEYFIRKPPSD
frog β 342 IHYLPKYLCIRRPKPE---TPLPVAPPPR--QVTSTRHADEYFIRRPEND
zebrafish β1a 342 INLLPRYLGVLRPTPEEPVEEEPKENVPMGCLENSLRPGGEYFIRKINPE
consensus 351 Ih-LPkYLglkRPkPE----peP---lp------s-R-adEYFIRkp--d
mouse β 399 FLFPKLNRFQPESSAPDLRRFIDGPTRAVGLPQELREVISSISYMARQLQ
frog β 387 FFLPKQERYHADPFSRDMKWFLEGPSLGLVLPRDLQSAVTAIRYLAQQLQ
zebrafish β1a 392 LVMPWRGSHN--ESTVKLQRFSNSDNYCLILPPNLKSAIAAITYMSEQLK
consensus 401 fllPk--rfq-e-ss-dlrrFidgpt-alvLP-eLrsaisaIsYma-QLq
mouse β 449 EQEDHDALKEDWQFVAMVVDRLFLWTFIVFTSVGTLVIFLDATYHLPPPE
frog β 437 EQEDYDTLKEDWQYVAMVVDRLFLWTFIAFTSLGTLSIFLDANFNLPPDT
zebrafish β1a 440 KQDVDDTMTDDWQYIAVVLDRLFLWLFVVITTLGTLTMFLDASFNYTPDQ
consensus 451 eQed-DtlkeDWQyvAmVvDRLFLWtFivfTslGTLsiFLDAtfnlpPd-
mouse β 499 PFP
frog β 487 PFP
zebrafish β1a 490 PFP
consensus 501 PFP

Figure 5.4: Primary amino acid sequence alignment of the zebrafish β and β1a subunits. Identical residues unshaded, conserved residues in light grey, and different residues in dark grey.

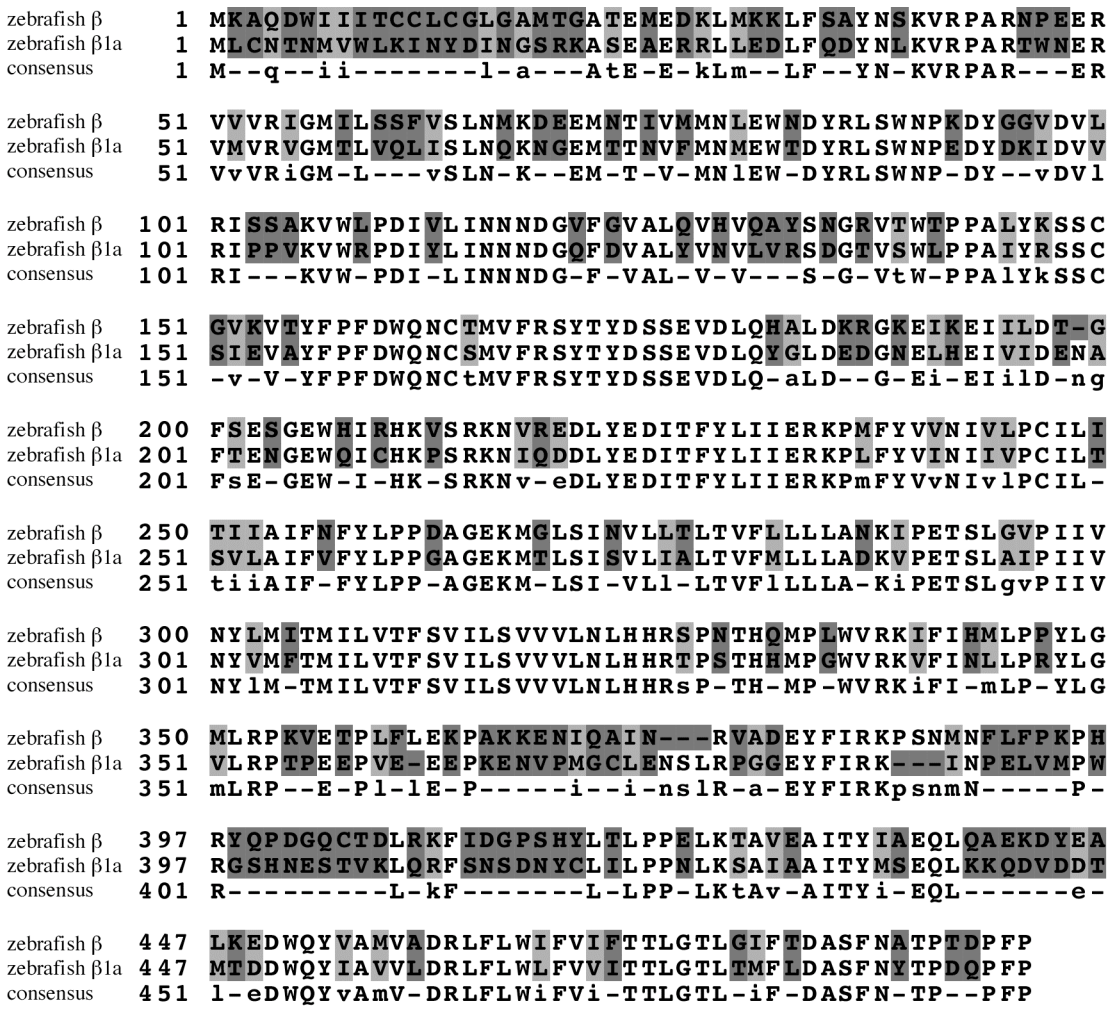
zebrafish β 1 MKAQDWIIITCCLCGLGAMTGATEMEDKLMKKLFSAYNSKVRPARNPEER
zebrafish β1a 1 MLCNTNMVWLKINYDINGSRKASEAERRLLEDLFQDYNLKVRPARTWNER
consensus 1 M--q--ii-------l-a---AtE-E-kLm--LF--YN-KVRPAR---ER
zebrafish β 51 VVVRIGMILSSFVSLNMKDEEMNTIVMMNLEWNDYRLSWNPKDYGGVDVL
zebrafish β1a 51 VMVRVGMTLVQLISLNQKNGEMTTNVFMNMEWTDYRLSWNPEDYDKIDVV
consensus 51 VvVRiGM-L---vSLN-K--EM-T-V-MNlEW-DYRLSWNP-DY--vDVl
zebrafish β 101 RISSAKVWLPDIVLINNNDGVFGVALQVHVQAYSNGRVTWTPPALYKSSC
zebrafish β1a 101 RIPPVKVWRPDIYLINNNDGQFDVALYVNVLVRSDGTVSWLPPAIYRSSC
consensus 101 RI---KVW-PDI-LINNNDG-F-VAL-V-V---S-G-VtW-PPAlYkSSC
zebrafish β 151 GVKVTYFPFDWQNCTMVFRSYTYDSSEVDLQHALDKRGKEIKEIILDT-G
zebrafish β1a 151 SIEVAYFPFDWQNCSMVFRSYTYDSSEVDLQYGLDEDGNELHEIVIDENA
consensus 151 -v-V-YFPFDWQNCtMVFRSYTYDSSEVDLQ-aLD--G-Ei-EIilD-ng
zebrafish β 200 FSESGEWHIRHKVSRKNVREDLYEDITFYLIIERKPMFYVVNIVLPCILI
zebrafish β1a 201 FTENGEWQICHKPSRKNIQDDLYEDITFYLIIERKPLFYVINIIVPCILT
consensus 201 FsE-GEW-I-HK-SRKNv-eDLYEDITFYLIIERKPmFYVvNIvlPCIL-
zebrafish β 250 TIIAIFNFYLPPDAGEKMGLSINVLLTLTVFLLLLANKIPETSLGVPIIV
zebrafish β1a 251 SVLAIFVFYLPPGAGEKMTLSISVLIALTVFMLLLADKVPETSLAIPIIV
consensus 251 tiiAIF-FYLPP-AGEKM-LSI-VLl-LTVFlLLLA-KiPETSLgvPIIV
zebrafish β 300 NYLMITMILVTFSVILSVVVLNLHHRSPNTHQMPLWVRKIFIHMLPPYLG
zebrafish β1a 301 NYVMFTMILVTFSVILSVVVLNLHHRTPSTHHMPGWVRKVFINLLPRYLG
consensus 301 NYlM-TMILVTFSVILSVVVLNLHHRsP-TH-MP-WVRKiFI-mLP-YLG
zebrafish β 350 MLRPKVETPLFLEKPAKKENIQAIN---RVADEYFIRKPSNMNFLFPKPH
zebrafish β1a 351 VLRPTPEEPVE-EEPKENVPMGCLENSLRPGGEYFIRK---INPELVMPW
consensus 351 mLRP--E-Pl-lE-P-----i--i-nslR-a-EYFIRKpsnmN-----P-
zebrafish β 397 RYQPDGQCTDLRKFIDGPSHYLTLPPELKTAVEAITYIAEQLQAEKDYEA
zebrafish β1a 397 RGSHNESTVKLQRFSNSDNYCLILPPNLKSAIAAITYMSEQLKKQDVDDT
consensus 401 R---------L-kF-------L-LPP-LKtAv-AITYi-EQL------e-
zebrafish β 447 LKEDWQYVAMVADRLFLWIFVIFTTLGTLGIFTDASFNATPTDPFP
zebrafish β1a 447 MTDDWQYIAVVLDRLFLWLFVVITTLGTLTMFLDASFNYTPDQPFP
consensus 451 l-eDWQYvAmV-DRLFLWiFVi-TTLGTL-iF-DASFN-TP--PFP

Figure 5.5: Primary amino acid sequence alignment of the zebrafish δ subunit. Identical residues unshaded, conserved residues in light grey, and different residues in dark grey.

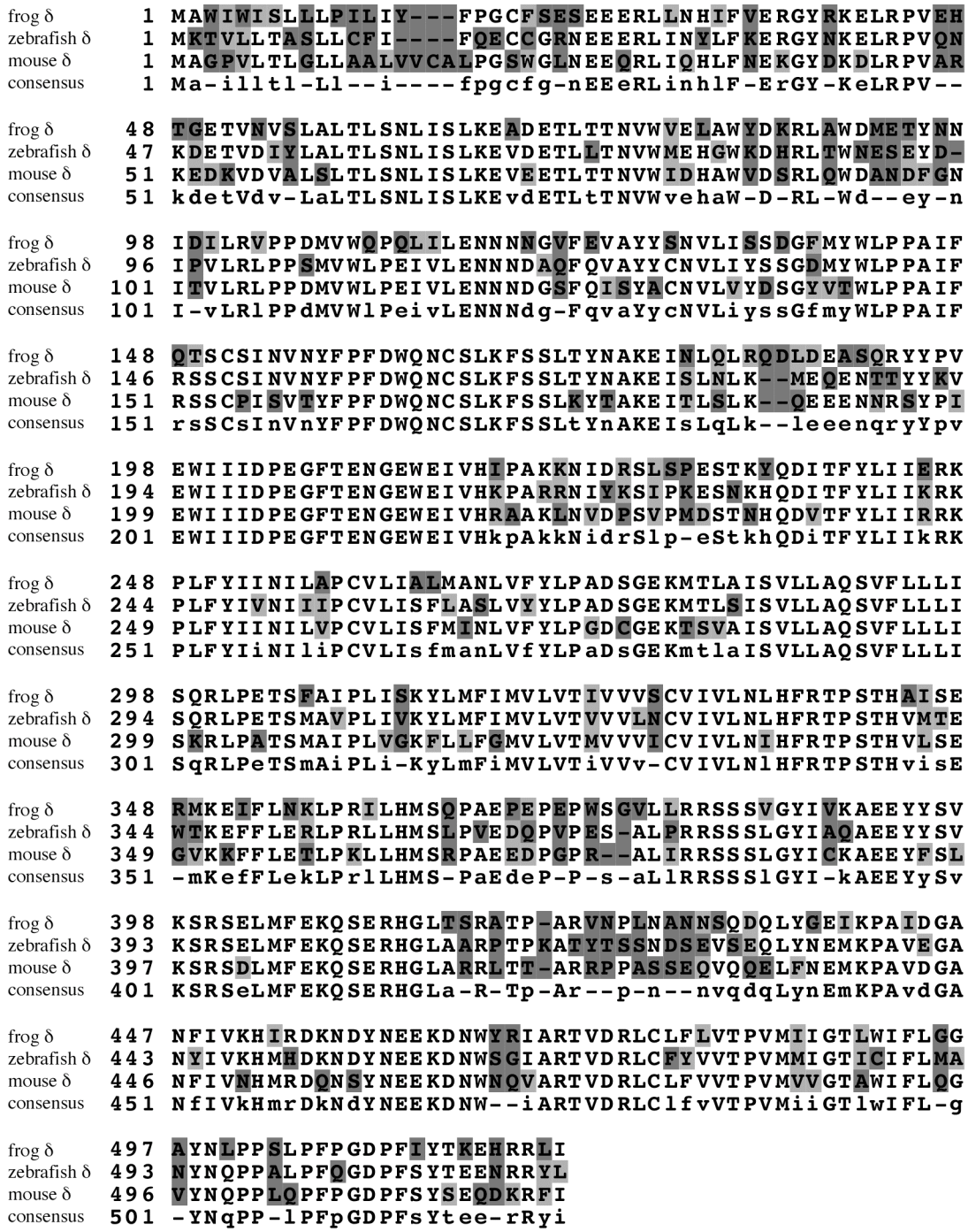
frog δ 1 MAWIWISLLLPILIY---FPGCFSESEEERLLNHIFVERGYRKELRPVEH
zebrafish δ 1 MKTVLLTASLLCFI----FQECCGRNEEERLINYLFKERGYNKELRPVQN
mouse δ 1 MAGPVLTLGLLAALVVCALPGSWGLNEEQRLIQHLFNEKGYDKDLRPVAR
consensus 1 Ma-illtl-Ll--i----fpgcfg-nEEeRLinhlF-ErGY-KeLRPV--
frog δ 48 TGETVNVSLALTLSNLISLKEADETLTTNVWVELAWYDKRLAWDMETYNN
zebrafish δ 47 KDETVDIYLALTLSNLISLKEVDETLLTNVWMEHGWKDHRLTWNESEYD-
mouse δ 51 KEDKVDVALSLTLSNLISLKEVEETLTTNVWIDHAWVDSRLQWDANDFGN
consensus 51 kdetVdv-LaLTLSNLISLKEvdETLtTNVWvehaW-D-RL-Wd--ey-n
frog δ 98 IDILRVPPDMVWQPQLILENNNNGVFEVAYYSNVLISSDGFMYWLPPAIF
zebrafish δ 96 IPVLRLPPSMVWLPEIVLENNNDAQFQVAYYCNVLIYSSGDMYWLPPAIF
mouse δ 101 ITVLRLPPDMVWLPEIVLENNNDGSFQISYACNVLVYDSGYVTWLPPAIF
consensus 101 I-vLRlPPdMVWlPeivLENNNdg-FqvaYycNVLiyssGfmyWLPPAIF
frog δ 148 QTSCSINVNYFPFDWQNCSLKFSSLTYNAKEINLQLRQDLDEASQRYYPV
zebrafish δ 146 RSSCSINVNYFPFDWQNCSLKFSSLTYNAKEISLNLK--MEQENTTYYKV
mouse δ 151 RSSCPISVTYFPFDWQNCSLKFSSLKYTAKEITLSLK--QEEENNRSYPI
consensus 151 rsSCsInVnYFPFDWQNCSLKFSSLtYnAKEIsLqLk--leeenqryYpv
frog δ 198 EWIIIDPEGFTENGEWEIVHIPAKKNIDRSLSPESTKYQDITFYLIIERK
zebrafish δ 194 EWIIIDPEGFTENGEWEIVHKPARRNIYKSIPKESNKHQDITFYLIIKRK
mouse δ 199 EWIIIDPEGFTENGEWEIVHRAAKLNVDPSVPMDSTNHQDVTFYLIIRRK
consensus 201 EWIIIDPEGFTENGEWEIVHkpAkkNidrSlp-eStkhQDiTFYLIIkRK
frog δ 248 PLFYIINILAPCVLIALMANLVFYLPADSGEKMTLAISVLLAQSVFLLLI
zebrafish δ 244 PLFYIVNIIIPCVLISFLASLVYYLPADSGEKMTLSISVLLAQSVFLLLI
mouse δ 249 PLFYIINILVPCVLISFMINLVFYLPGDCGEKTSVAISVLLAQSVFLLLI
consensus 251 PLFYIiNIliPCVLIsfmanLVfYLPaDsGEKmtlaISVLLAQSVFLLLI
frog δ 298 SQRLPETSFAIPLISKYLMFIMVLVTIVVVSCVIVLNLHFRTPSTHAISE
zebrafish δ 294 SQRLPETSMAVPLIVKYLMFIMVLVTVVVLNCVIVLNLHFRTPSTHVMTE
mouse δ 299 SKRLPATSMAIPLVGKFLLFGMVLVTMVVVICVIVLNIHFRTPSTHVLSE
consensus 301 SqRLPeTSmAiPLi-KyLmFiMVLVTiVVv-CVIVLNlHFRTPSTHvisE
frog δ 348 RMKEIFLNKLPRILHMSQPAEPEPEPWSGVLLRRSSSVGYIVKAEEYYSV
zebrafish δ 344 WTKEFFLERLPRLLHMSLPVEDQPVPES-ALPRRSSSLGYIAQAEEYYSV
mouse δ 349 GVKKFFLETLPKLLHMSRPAEEDPGPR--ALIRRSSSLGYICKAEEYFSL
consensus 351 -mKefFLekLPrlLHMS-PaEdeP-P-s-aLlRRSSSlGYI-kAEEYySv
frog δ 398 KSRSELMFEKQSERHGLTSRATP-ARVNPLNANNSQDQLYGEIKPAIDGA
zebrafish δ 393 KSRSELMFEKQSERHGLAARPTPKATYTSSNDSEVSEQLYNEMKPAVEGA
mouse δ 397 KSRSDLMFEKQSERHGLARRLTT-ARRPPASSEQVQQELFNEMKPAVDGA
consensus 401 KSRSeLMFEKQSERHGLa-R-Tp-Ar--p-n--nvqdqLynEmKPAvdGA
frog δ 447 NFIVKHIRDKNDYNEEKDNWYRIARTVDRLCLFLVTPVMIIGTLWIFLGG
zebrafish δ 443 NYIVKHMHDKNDYNEEKDNWSGIARTVDRLCFYVVTPVMMIGTICIFLMA
mouse δ 446 NFIVNHMRDQNSYNEEKDNWNQVARTVDRLCLFVVTPVMVVGTAWIFLQG
consensus 451 NfIVkHmrDkNdYNEEKDNW--iARTVDRLClfvVTPVMiiGTlwIFL-g
frog δ 497 AYNLPPSLPFPGDPFIYTKEHRRLI
zebrafish δ 493 NYNQPPALPFQGDPFSYTEENRRYL
mouse δ 496 VYNQPPLQPFPGDPFSYSEQDKRFI
consensus 501 -YNqPP-lPFpGDPFsYtee-rRyi

Figure 5.6: Primary amino acid sequence alignment of the zebrafish γ subunit. Identical residues unshaded, conserved residues in light grey, and different residues in dark grey.

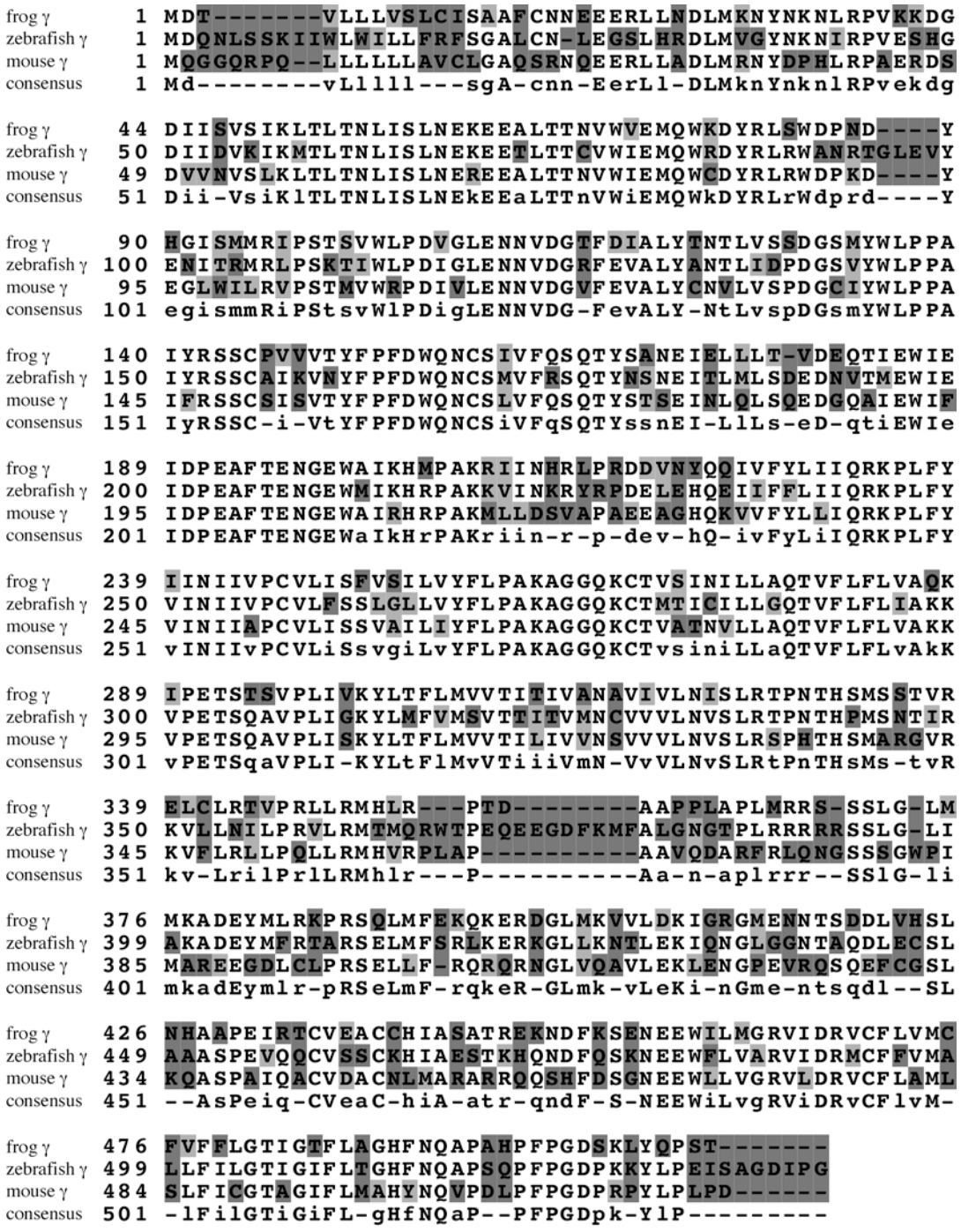
frog γ 1 MDT-------VLLLVSLCISAAFCNNEEERLLNDLMKNYNKNLRPVKKDG
zebrafish γ 1 MDQNLSSKIIWLWILLFRFSGALCN-LEGSLHRDLMVGYNKNIRPVESHG
mouse γ 1 MQGGQRPQ--LLLLLLAVCLGAQSRNQEERLLADLMRNYDPHLRPAERDS
consensus 1 Md--------vLllll---sgA-cnn-EerLl-DLMknYnknlRPvekdg
frog γ 44 DIISVSIKLTLTNLISLNEKEEALTTNVWVEMQWKDYRLSWDPND----Y
zebrafish γ 50 DIIDVKIKMTLTNLISLNEKEETLTTCVWIEMQWRDYRLRWANRTGLEVY
mouse γ 49 DVVNVSLKLTLTNLISLNEREEALTTNVWIEMQWCDYRLRWDPKD----Y
consensus 51 Dii-VsiKlTLTNLISLNEkEEaLTTnVWiEMQWkDYRLrWdprd----Y
frog γ 90 HGISMMRIPSTSVWLPDVGLENNVDGTFDIALYTNTLVSSDGSMYWLPPA
zebrafish γ 100 ENITRMRLPSKTIWLPDIGLENNVDGRFEVALYANTLIDPDGSVYWLPPA
mouse γ 95 EGLWILRVPSTMVWRPDIVLENNVDGVFEVALYCNVLVSPDGCIYWLPPA
consensus 101 egismmRiPStsvWlPDigLENNVDG-FevALY-NtLvspDGsmYWLPPA
frog γ 140 IYRSSCPVVVTYFPFDWQNCSIVFQSQTYSANEIELLLT-VDEQTIEWIE
zebrafish γ 150 IYRSSCAIKVNYFPFDWQNCSMVFRSQTYNSNEITLMLSDEDNVTMEWIE
mouse γ 145 IFRSSCSISVTYFPFDWQNCSLVFQSQTYSTSEINLQLSQEDGQAIEWIF
consensus 151 IyRSSC-i-VtYFPFDWQNCSiVFqSQTYssnEI-LlLs-eD-qtiEWIe
frog γ 189 IDPEAFTENGEWAIKHMPAKRIINHRLPRDDVNYQQIVFYLIIQRKPLFY
zebrafish γ 200 IDPEAFTENGEWMIKHRPAKKVINKRYRPDELEHQEIIFFLIIQRKPLFY
mouse γ 195 IDPEAFTENGEWAIRHRPAKMLLDSVAPAEEAGHQKVVFYLLIQRKPLFY
consensus 201 IDPEAFTENGEWaIkHrPAKriin-r-p-dev-hQ-ivFyLiIQRKPLFY
frog γ 239 IINIIVPCVLISFVSILVYFLPAKAGGQKCTVSINILLAQTVFLFLVAQK
zebrafish γ 250 VINIIVPCVLFSSLGLLVYFLPAKAGGQKCTMTICILLGQTVFLFLIAKK
mouse γ 245 VINIIAPCVLISSVAILIYFLPAKAGGQKCTVATNVLLAQTVFLFLVAKK
consensus 251 vINIIvPCVLiSsvgiLvYFLPAKAGGQKCTvsiniLLaQTVFLFLvAkK
frog γ 289 IPETSTSVPLIVKYLTFLMVVTITIVANAVIVLNISLRTPNTHSMSSTVR
zebrafish γ 300 VPETSQAVPLIGKYLMFVMSVTTITVMNCVVVLNVSLRTPNTHPMSNTIR
mouse γ 295 VPETSQAVPLISKYLTFLMVVTILIVVNSVVVLNVSLRSPHTHSMARGVR
consensus 301 vPETSqaVPLI-KYLtFlMvVTiiiVmN-VvVLNvSLRtPnTHsMs-tvR
frog γ 339 ELCLRTVPRLLRMHLR---PTD---------AAPPLAPLMRRS-SSLG-LM
zebrafish γ 350 KVLLNILPRVLRMTMQRWTPEQEEGDFKMFALGNGTPLRRRRRSSLG-LI
mouse γ 345 KVFLRLLPQLLRMHVRPLAP----------AAVQDARFRLQNGSSSGWPI
consensus 351 kv-LrilPrlLRMhlr---P----------Aa-n-aplrrr--SSlG-li
frog γ 376 MKADEYMLRKPRSQLMFEKQKERDGLMKVVLDKIGRGMENNTSDDLVHSL
zebrafish γ 399 AKADEYMFRTARSELMFSRLKERKGLLKNTLEKIQNGLGGNTAQDLECSL
mouse γ 385 MAREEGDLCLPRSELLF-RQRQRNGLVQAVLEKLENGPEVRQSQEFCGSL
consensus 401 mkadEymlr-pRSeLmF-rqkeR-GLmk-vLeKi-nGme-ntsqdl--SL
frog γ 426 NHAAPEIRTCVEACCHIASATREKNDFKSENEEWILMGRVIDRVCFLVMC
zebrafish γ 449 AAASPEVQQCVSSCKHIAESTKHQNDFQSKNEEWFLVARVIDRMCFFVMA
mouse γ 434 KQASPAIQACVDACNLMARARRQQSHFDSGNEEWLLVGRVLDRVCFLAML
consensus 451 --AsPeiq-CVeaC-hiA-atr-qndF-S-NEEWiLvgRViDRvCFlvM-
frog γ 476 FVFFLGTIGTFLAGHFNQAPAHPFPGDSKLYQPST-------
zebrafish γ 499 LLFILGTIGIFLTGHFNQAPSQPFPGDPKKYLPEISAGDIPG
mouse γ 484 SLFICGTAGIFLMAHYNQVPDLPFPGDPRPYLPLPD------
consensus 501 -lFilGTiGiFL-gHfNQaP--PFPGDpk-YlP---------

Figure 5.7: Primary amino acid sequence alignment of the zebrafish ε subunit. Identical residues unshaded, conserved residues in light grey, and different residues in dark grey.

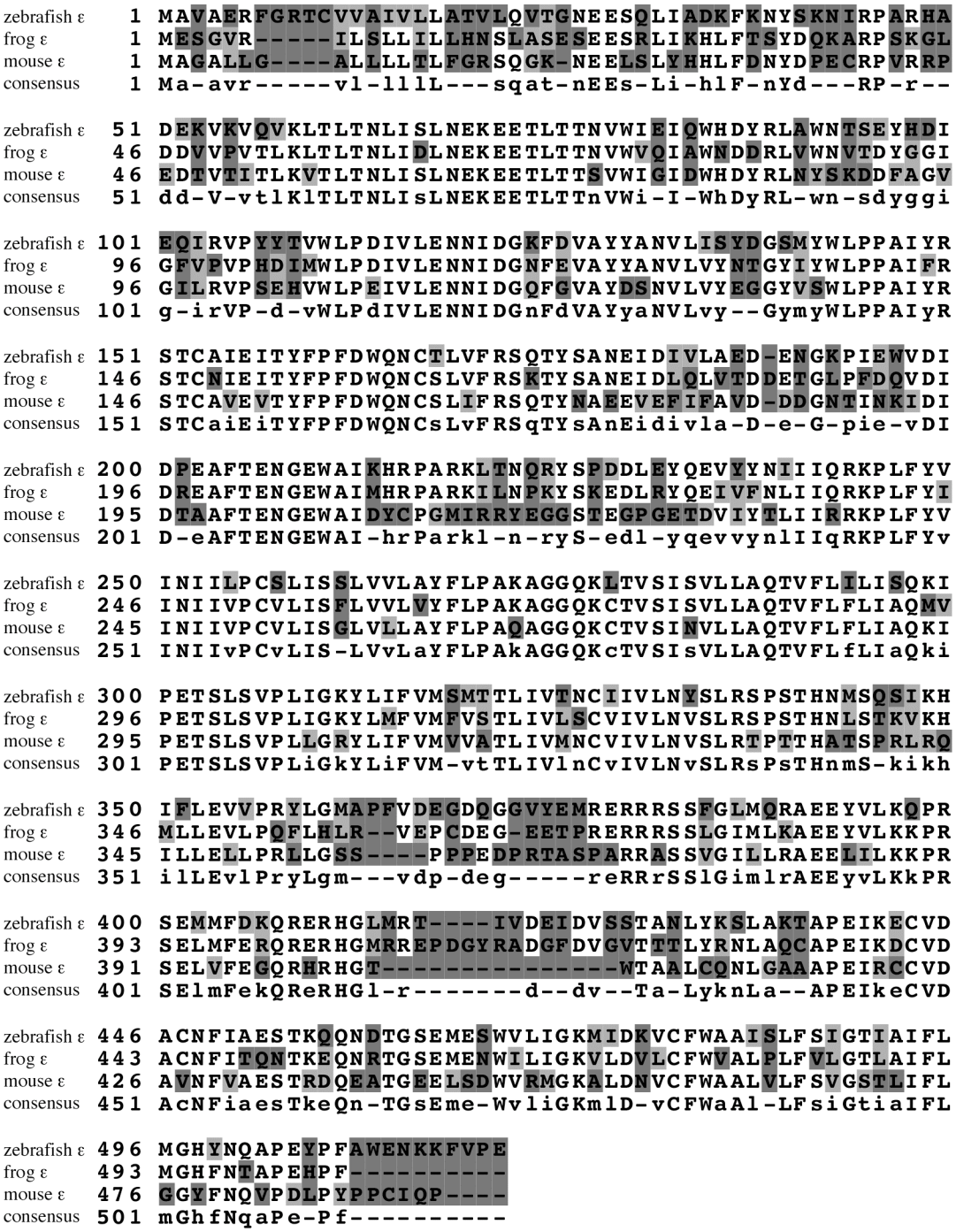
zebrafish ε 1 MAVAERFGRTCVVAIVLLATVLQVTGNEESQLIADKFKNYSKNIRPARHA
frog ε 1 MESGVR-----ILSLLILLHNSLASESEESRLIKHLFTSYDQKARPSKGL
mouse ε 1 MAGALLG----ALLLLTLFGRSQGK-NEELSLYHHLFDNYDPECRPVRRP
consensus 1 Ma-avr-----vl-lllL---sqat-nEEs-Li-hlF-nYd---RP-r--
zebrafish ε 51 DEKVKVQVKLTLTNLISLNEKEETLTTNVWIEIQWHDYRLAWNTSEYHDI
frog ε 46 DDVVPVTLKLTLTNLIDLNEKEETLTTNVWVQIAWNDDRLVWNVTDYGGI
mouse ε 46 EDTVTITLKVTLTNLISLNEKEETLTTSVWIGIDWHDYRLNYSKDDFAGV
consensus 51 dd-V-vtlKlTLTNLIsLNEKEETLTTnVWi-I-WhDyRL-wn-sdyggi
zebrafish ε 101 EQIRVPYYTVWLPDIVLENNIDGKFDVAYYANVLISYDGSMYWLPPAIYR
frog ε 96 GFVPVPHDIMWLPDIVLENNIDGNFEVAYYANVLVYNTGYIYWLPPAIFR
mouse ε 96 GILRVPSEHVWLPEIVLENNIDGQFGVAYDSNVLVYEGGYVSWLPPAIYR
consensus 101 g-irVP-d-vWLPdIVLENNIDGnFdVAYyaNVLvy--GymyWLPPAIyR
zebrafish ε 151 STCAIEITYFPFDWQNCTLVFRSQTYSANEIDIVLAED-ENGKPIEWVDI
frog ε 146 STCNIEITYFPFDWQNCSLVFRSKTYSANEIDLQLVTDDETGLPFDQVDI
mouse ε 146 STCAVEVTYFPFDWQNCSLIFRSQTYNAEEVEFIFAVD-DDGNTINKIDI
consensus 151 STCaiEiTYFPFDWQNCsLvFRSqTYsAnEidivla-D-e-G-pie-vDI
zebrafish ε 200 DPEAFTENGEWAIKHRPARKLTNQRYSPDDLEYQEVYYNIIIQRKPLFYV
frog ε 196 DREAFTENGEWAIMHRPARKILNPKYSKEDLRYQEIVFNLIIQRKPLFYI
mouse ε 195 DTAAFTENGEWAIDYCPGMIRRYEGGSTEGPGETDVIYTLIIRRKPLFYV
consensus 201 D-eAFTENGEWAI-hrParkl-n-ryS-edl-yqevvynlIIqRKPLFYv
zebrafish ε 250 INIILPCSLISSLVVLAYFLPAKAGGQKLTVSISVLLAQTVFLILISQKI
frog ε 246 INIIVPCVLISFLVVLVYFLPAKAGGQKCTVSISVLLAQTVFLFLIAQMV
mouse ε 245 INIIVPCVLISGLVLLAYFLPAQAGGQKCTVSINVLLAQTVFLFLIAQKI
consensus 251 INIIvPCvLIS-LVvLaYFLPAkAGGQKcTVSIsVLLAQTVFLfLIaQki
zebrafish ε 300 PETSLSVPLIGKYLIFVMSMTTLIVTNCIIVLNYSLRSPSTHNMSQSIKH
frog ε 296 PETSLSVPLIGKYLMFVMFVSTLIVLSCVIVLNVSLRSPSTHNLSTKVKH
mouse ε 295 PETSLSVPLLGRYLIFVMVVATLIVMNCVIVLNVSLRTPTTHATSPRLRQ
consensus 301 PETSLSVPLiGkYLiFVM-vtTLIVlnCvIVLNvSLRsPsTHnmS-kikh
zebrafish ε 350 IFLEVVPRYLGMAPFVDEGDQGGVYEMRERRRSSFGLMQRAEEYVLKQPR
frog ε 346 MLLEVLPQFLHLR--VEPCDEG-EETPRERRRSSLGIMLKAEEYVLKKPR
mouse ε 345 ILLELLPRLLGSS----PPPEDPRTASPARRASSVGILLRAEELILKKPR
consensus 351 ilLEvlPryLgm---vdp-deg-----reRRrSSlGimlrAEEyvLKkPR
zebrafish ε 400 SEMMFDKQRERHGLMRT----IVDEIDVSSTANLYKSLAKTAPEIKECVD
frog ε 393 SELMFERQRERHGMRREPDGYRADGFDVGVTTTLYRNLAQCAPEIKDCVD
mouse ε 391 SELVFEGQRHRHGT----------------WTAALCQNLGAAAPEIRCCVD
consensus 401 SElmFekQReRHGl-r-------d--dv--Ta-LyknLa--APEIkeCVD
zebrafish ε 446 ACNFIAESTKQQNDTGSEMESWVLIGKMIDKVCFWAAISLFSIGTIAIFL
frog ε 443 ACNFITQNTKEQNRTGSEMENWILIGKVLDVLCFWVALPLFVLGTLAIFL
mouse ε 426 AVNFVAESTRDQEATGEELSDWVRMGKALDNVCFWAALVLFSVGSTLIFL
consensus 451 AcNFiaesTkeQn-TGsEme-WvliGKmlD-vCFWaAl-LFsiGtiaIFL
zebrafish ε 496 MGHYNQAPEYPFAWENKKFVPE
frog ε 493 MGHFNTAPEHPF----------
mouse ε 476 GGYFNQVPDLPYPPCIQP----
consensus 501 mGhfNqaPe-Pf----------

Because protein sequences for AChR subunits are highly similar at the amino acid level, the question arises as to whether a given subunit has been identified. To aid in this determination, an unrooted phylogenetic tree was generated by multiple sequence alignment of zebrafish amino acid sequence with muscle AChR subunit sequences for human, mouse, frog (Xenopus laevis), pufferfish (Takifugu rubripes), chicken, and cow (Figure 5.8A). The accession numbers for the protein sequences used in the alignment are included in Chapter 2. The phylogenetic tree segregates into five main branches, which are colored for clarity. Each branch corresponds to a different subunit cluster, α, β, δ, γ and ε. As with the other species, the zebrafish subunits all separate into their respective branches.

Similarity between human and zebrafish subunit protein sequences was quantified by the percent amino acid identity determined by pairwise alignments. Each predicted zebrafish homolog shares the highest amino acid identity with its human counterpart (Figure 5.8B).

Macroscopic currents produced by zebrafish AChRs in oocytes

The Xenopus oocyte expression system has been used extensively to investigate the single-channel properties of reconstituted AChRs. I used stage V and VI Xenopus oocytes to reconstitute zebrafish AChRs for all of my functional studies. The first approach was to determine which of the many possible combinations of zebrafish subunits were functional. I worked under the assumption that the α subunit was indispensable for channel function, which has held true for all nicotinic AChRs, both neuronal and muscle receptor types. Additionally, studies of mutant zebrafish indicates

Figure 5.8: Comparison of zebrafish subunit amino acid sequence similarity to other vertebrates. A) Muscle AChR subunit amino acid sequence phylogenetic tree. Accession numbers associated with each sequence are indicated in Chapter 2. B) Table of percent identity values from pair-wise alignments of human and zebrafish muscle AChR amino acid sequence. Human sequences are indicated in uppercase, and zebrafish subunits are indicated by symbols. Numbers set in bold type indicate greatest percent identity values.

A

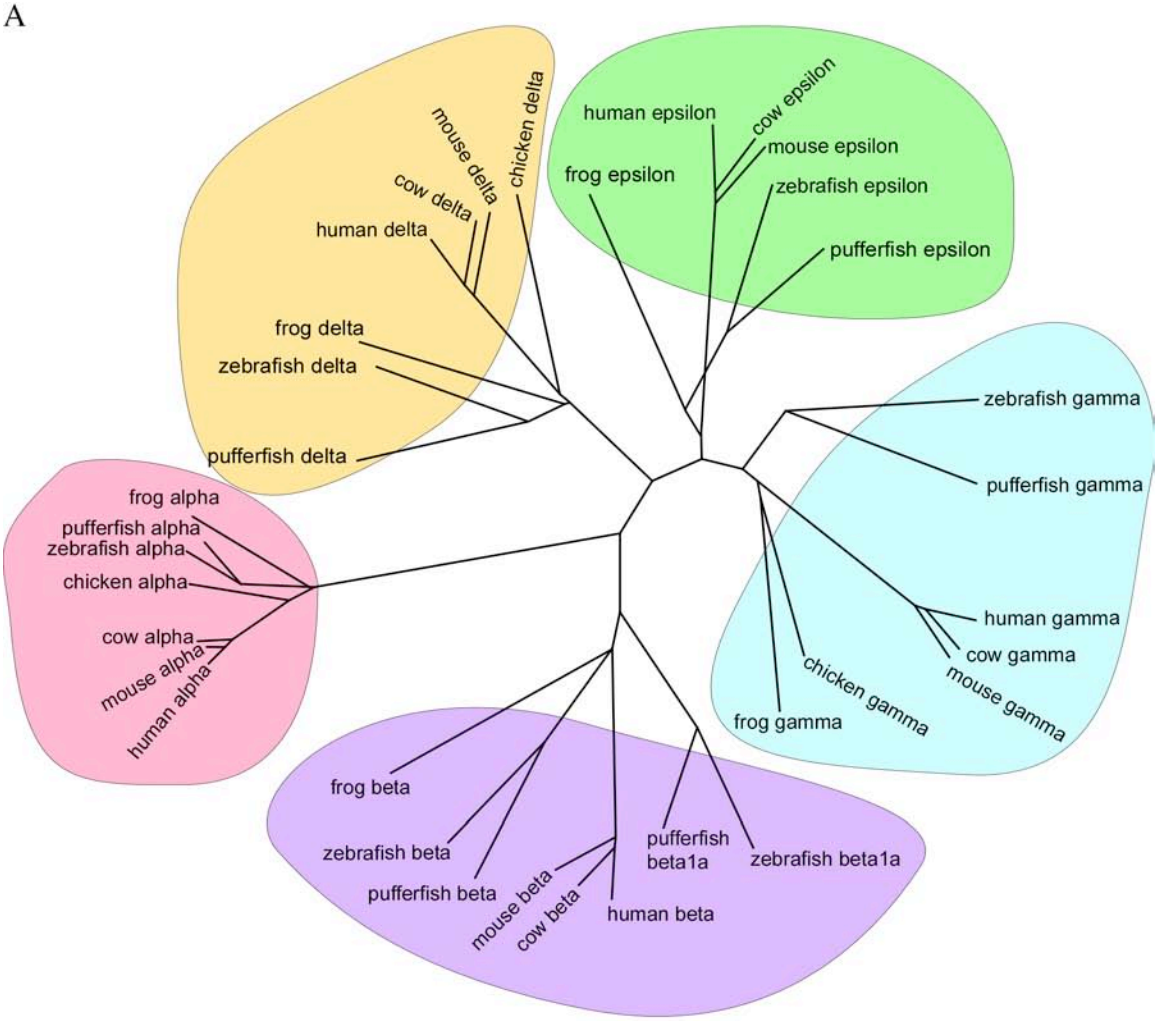

B

	α	β	β_{1a}	δ	γ	ε
A	**77.2**	36.1	38.1	33.3	30.5	31.5
B	35.8	**58.2**	**53.5**	39.2	36.7	37.4
D	34.2	37	39.3	**67.2**	43.4	45.8
G	31.2	36.3	40.5	45.1	**53.4**	50.7
E	30.2	37.5	40	43.4	46.2	**53.4**

that the α subunit is necessary to form fast and slow muscle receptors (Sepich et al, 1998).

Different combinations of synthetic RNA encoding each subunit were mixed in equal ratios with the α subunit RNA, and then injected into the oocytes. I used two-electrode voltage clamp to determine the maximum current response associated with ACh application. For this purpose, oocyte membrane potentials were held at -80 mV, and a saturating concentration (30 μM) ACh was applied for approximately 10 seconds, or until a plateau was recorded for the elicited current. The synthetic RNAs encoding the Xenopus subunit combination αβδγ were used as a positive control for current amplitude of an AChR that expresses well in reconstitution experiments (Paradiso and Brehm, 1998). Each oocyte was tested for responsiveness to ACh between two and five days after RNA injection, and the resultant maximum current amplitude was recorded (Figure 5.9A). The shape of the response varied between trials, and experiments. Variability in kinetics reflected differences in the onset and duration of the ACh perfusion in specific experiments. By comparison, variability in the amplitudes was small.

The zebrafish subunit combinations that produced robust currents were αβδ, αβδγ and αβδε. A representative trace from a zebrafish αβδγ injected oocyte is shown in Figure 5.9B. A summary of the maximum current amplitudes produced by all combinations tested is shown in Figure 5.10A. The function of each zebrafish β subunit was tested separately, and no combinations with the β1a subunit functioned to the same extent as combinations with the β subunit. The summary data from Figure 5.10A was also plotted on a semi-logarithmic scale to compare the very small responses associated with most subunit combinations (Figure 5.10B).

Figure 5.9: Macroscopic current recordings from oocytes. A) Three consecutive responses to 30 μM ACh application (black bar) of an oocyte injected with the Xenopus subunit combination αβδγ, at -80 mV. B) Three consecutive responses to ACh application of an oocyte injected with the zebrafish subunit combination αβδγ.

A

Xenopus αβδγ

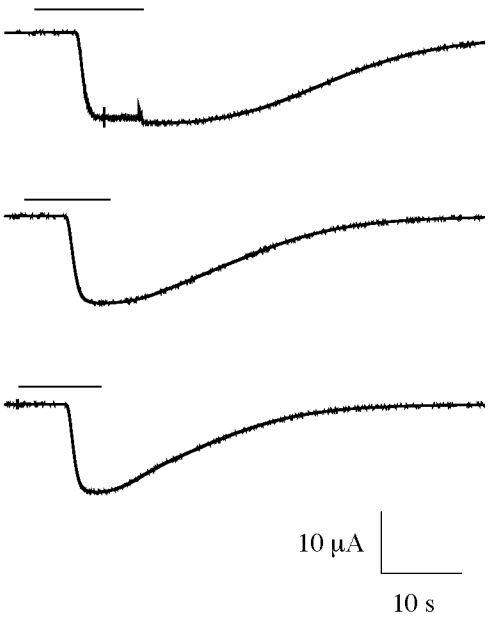

B

Zebrafish αβδγ

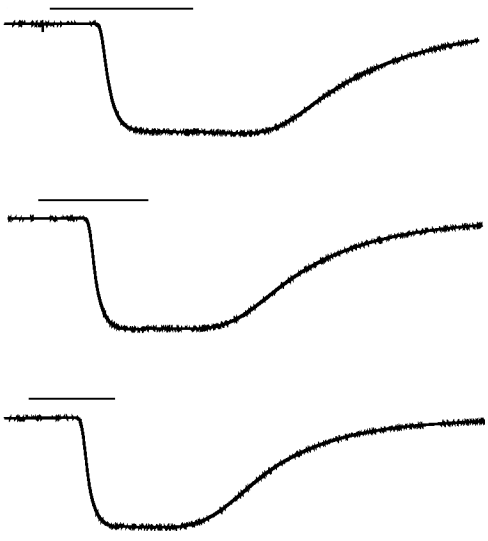

Figure 5.10: Summary of zebrafish AChR subunit combination response to ACh. A) Average maximum ACh-elicited current response ± SD, for each subunit combination tested. All recordings were performed at -80 mV, and the number of oocytes tested is indicated above the error bars. The dashed line indicates a current response of 1 μA. B) Same data as A, plotted on semi-logarithmic scale.

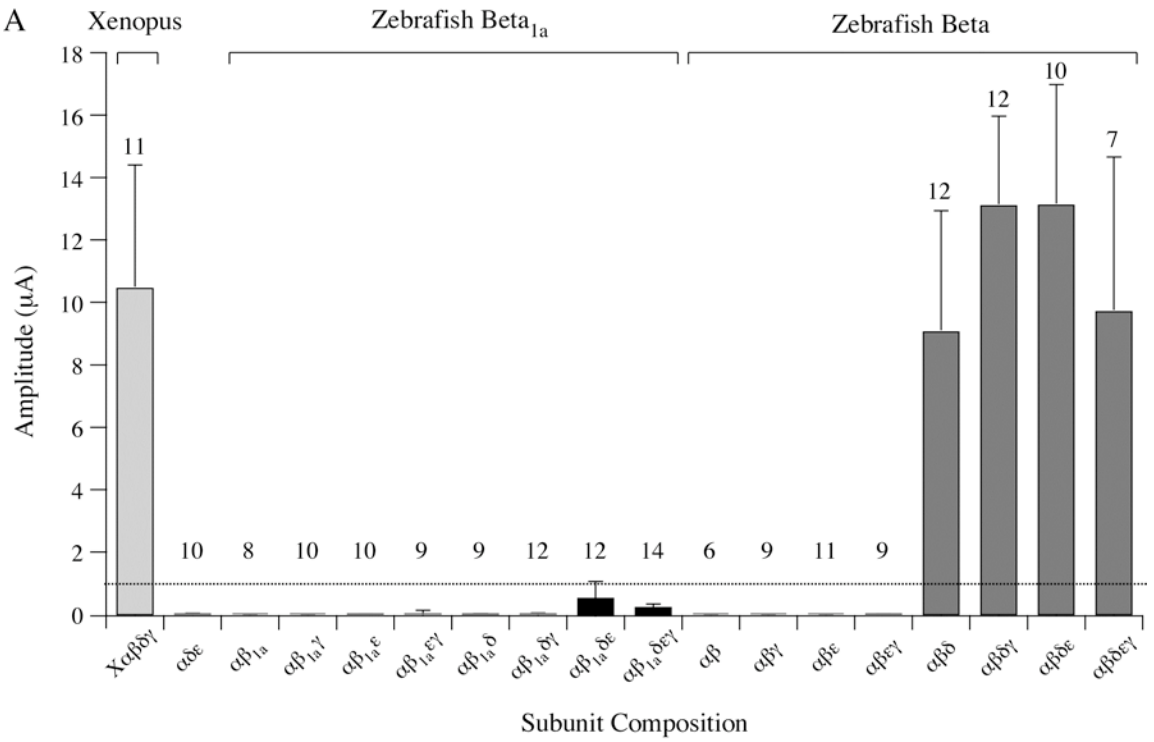
A
Xenopus
Zebrafish Beta1a
Zebrafish Beta
Amplitude (μA)
18
16
14
12
10
8
6
4
2
0
11
10
8
10
10
9
9
12
12
14
6
9
11
9
12
12
10
7
Xαβδγ
αδε
αβ1a
αβ1aγ
αβ1aε
αβ1aεγ
αβ1aδ
αβ1aδγ
αβ1aδε
αβ1aδεγ
αβ
αβγ
αβε
αβεγ
αβδ
αβδγ
αβδε
αβδεγ
Subunit Composition

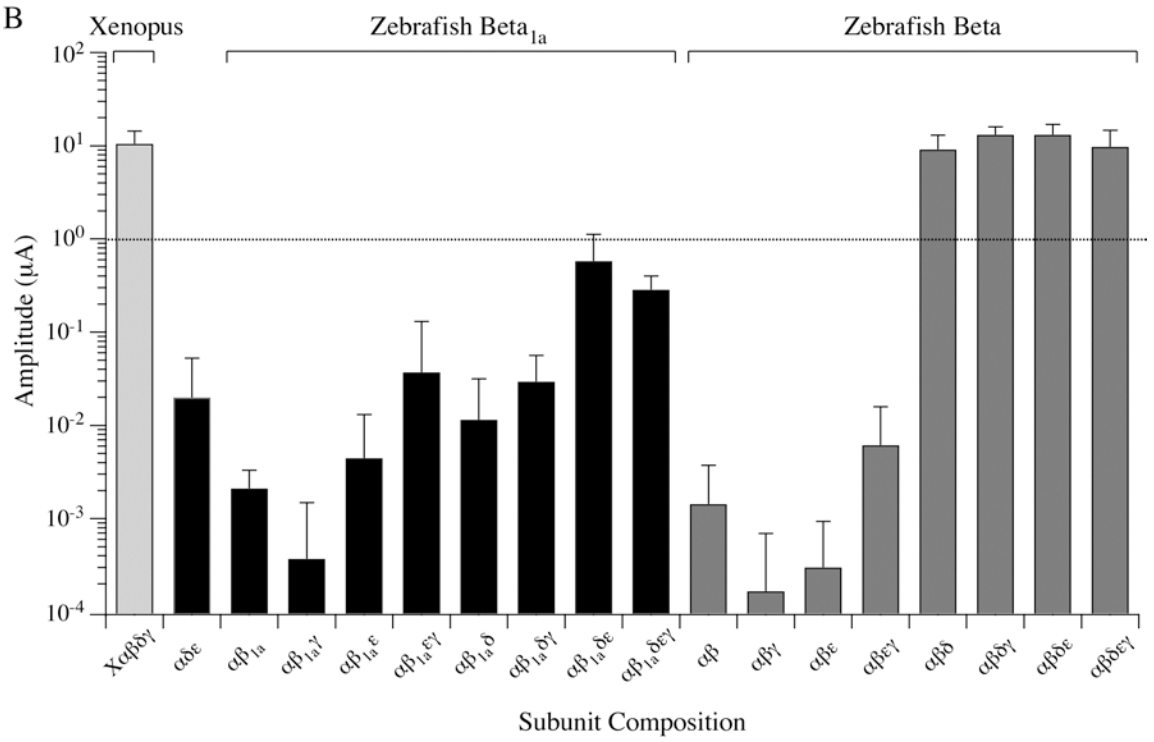
B
Xenopus
Zebrafish Beta1a
Zebrafish Beta
Amplitude (μA)
10^2
10^1
10^0
10^-1
10^-2
10^-3
10^-4
Xαβδγ
αδε
αβ1a
αβ1aγ
αβ1aε
αβ1aεγ
αβ1aδ
αβ1aδγ
αβ1aδε
αβ1aδεγ
αβ
αβγ
αβε
αβεγ
αβδ
αβδγ
αβδε
αβδεγ
Subunit Composition

Efforts to improve β1a channel expression

A minimum current level of 1 μA normally indicates the lower cutoff of expression levels necessary for single-channel analysis. The only combination with β1a that came close to satisfying this criterion was the αβ1aδε combination (0.6 ± 0.4 μA). Because the αβ1aδε combination produced the largest currents of any β1a mixture, I focused on αβ1aδε as a representative combination and made several attempts to increase the expression levels.

I first increased the amount of β1a RNA injected (9 ng per oocyte to 36 ng per oocyte) but more RNA did not result in increased current responses. Next, I injected β1a RNA (36 ng/injection) on sequential days after the first injection of αβ1aδε, in an effort to curb potential β1a RNA degradation. These additional injections also had no effect. Finally, I altered the sequence preceding the initiation codon of β1a, in an effort to optimize translation. I replaced the native sequence (5'TAACACCAACATG3') with the synthetic sequence (5'GAATTCGCCACCATG3') that is identical to that found upstream of the initiation codon of both α and δ subunit sequences. The synthetic sequence better represented a canonical kozak sequence (cgccgccRcc), that is often important for translation efficiency. Changes to the sequence upstream of the initiator codon did not change the current amplitudes for αβ1aδε.

Additional measures were also taken to investigate the integrity of the β1a coding sequence. Inspection of the newly available genomic sequence indicated there was an additional in-frame initiation codon located only 18 nucleotides upstream of the current β1a sequence start codon (…5'ATGTTATGTAACACCAACATG 3'…). To address the possibility that this sequence was missing from the β1a coding sequence, I added these

18 nucleotides to the 5' end, but the additional sequence did not change the current response amplitude. Finally, zebrafish mRNA was re-examined to determine if alternative forms of the β1a transcripts exist. Originally, only a single transcript was detected; however, a second attempt identified a possible alternative splice form. In the alternative form the first exon is omitted, and translation initiates from exon 2. Testing of the alternative β1a sequence in oocytes did not show increased current responses.

The persistently low expression of the αβ1aδε combination indicated that the β1a subunit was not a functional substitute for the β subunit in the AChR, and combinations with β1a were not suitable for single-channel analysis. The basis for the lack of functional expression remains unknown, and thus could reflect the failure of β1a containing receptors to assemble, to traffic to the membrane, or to form functional channels.

Single-channel properties of reconstituted zebrafish AchRs

Oocytes were prepared for single-channel recording, as previously described for the macroscopic current analysis, except that the vitelline membrane was removed just prior to recording. Single-channel currents were examined in the outside-out patch configuration, and thus the membrane potentials reported correspond to the actual transmembrane potential. During outside-out recordings, the bath recording solution contained a low concentration of ACh (300 nM), to elicit single-channel events.

Single-channel properties of the αβδ subunit combination

The first subunit combination studied at the single-channel level was αβδ. Application of a low concentration of ACh (300 nM) elicited single-channel currents throughout the recording (Figure 5.11A). At all potentials tested, the events were described by a single amplitude distribution; for the example patch shown at -100 mV, the Gaussian fit corresponded to a mean amplitude of 8.0 pA (Figure 5.11B). The event amplitude of all recordings from αβδ (n=13) indicated an average amplitude of 7.9 pA, at -100 mV (Figure 5.11B, scatter plot).

Amplitude distributions were fit for each recording at potentials between -130 and -30 mV, in 10 mV increments. The current-voltage relationship was well fit by linear regression, and the fit to the example recording indicated a slope of 71 pS and an estimated reversal potential of -10 mV (Figure 5.11C). Similar current-voltage plots were constructed for each recording, and fit by linear regression (Figure 5.11D). For all αβδ recordings (n=11), the average values correspond to a single-channel conductance of 70 ± 5 pS, and a reversal potential of -8 ± 5 mV (Figure 5.11E). The cumulative current-voltage plot (Figure 5.11F) of the average amplitude for all recordings indicated a conductance of 73 pS and reversal potential of -5 mV.

The burst duration histogram for αβδ events was constructed as previously described for muscle AChRs (Figure 5.12A). Fitting of the burst duration required two exponents for each recording at -100 mV (n=7 recordings). The first component of the fit was extremely brief and corresponded to 0.18 ms in the example histogram. Because this component was too brief to be resolved fully (due to the limitations of the frequency response of the equipment), the mean duration and contribution to the distribution could

Figure 5.11: Single-channel properties of ACh-activated events of the αβδ combination. A) Sample traces indicating single-channel events at -100 mV. B) Amplitude histogram for all events at -100 mV for example recording in A. Scatter plot indicates average amplitude for all recordings (n=13) at -100 mV (filled circles) and overall mean amplitude ± SD. C) Current-voltage relations for a single recording, fit by linear regression. Fit corresponds to a slope conductance of 71 pS, and reversal potential of -10 mV. Dashed line indicates zero current level. D) Current-voltage relations for each of 11 recordings, with linear fit. E) Scatter plot indicating conductance and reversal potential values for the 11 recordings (filled circles) and corresponding average conductance and reversal potential values ± SD (open circles). F) Cumulative current-voltage relations for averaged data of all 11 recordings. Linear fit indicates overall conductance of 73 pS and reversal potential of -5 mV.

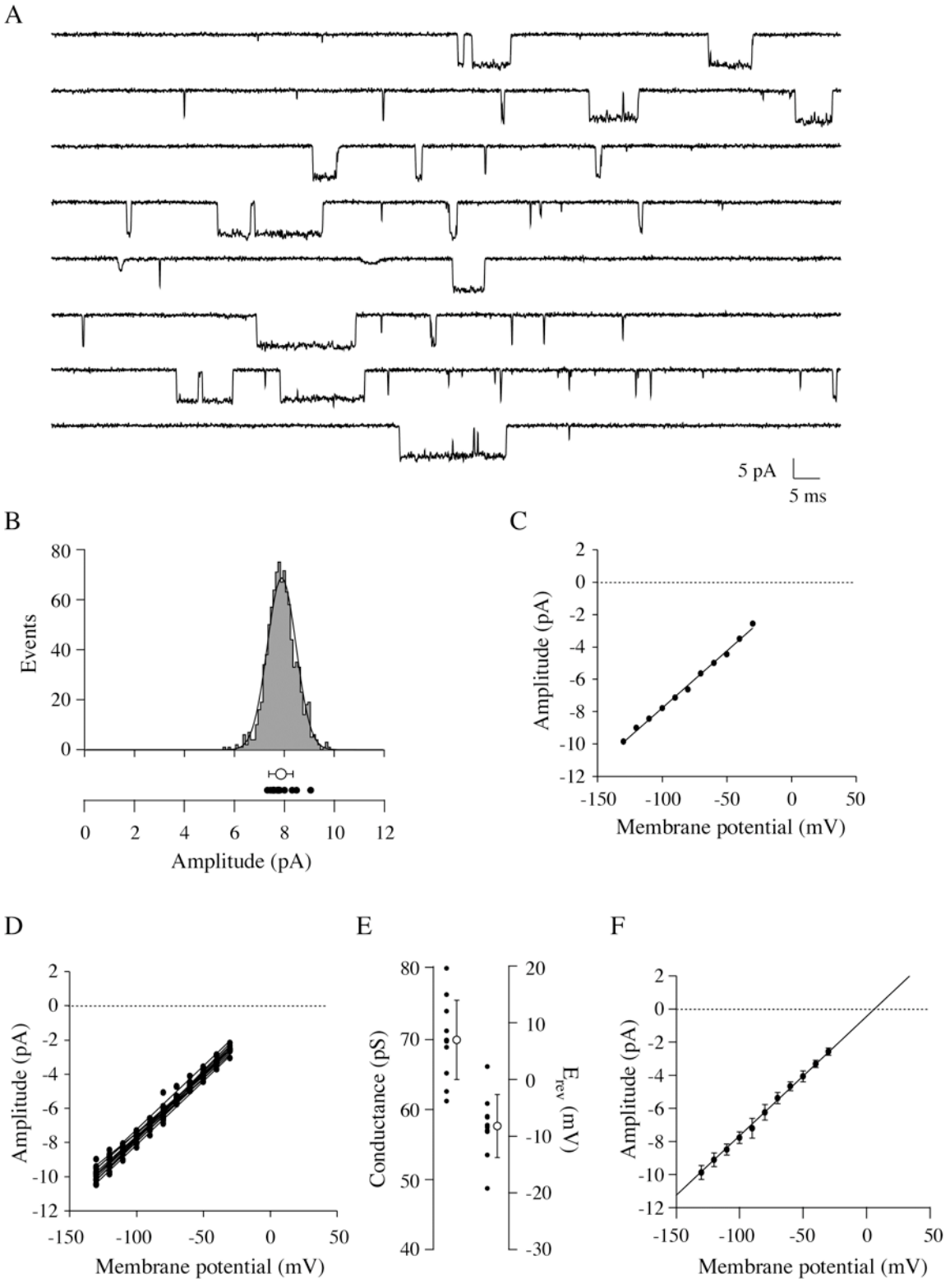
A
5 pA
5 ms
B
Events
Amplitude (pA)
C
Amplitude (pA)
Membrane potential (mV)
D
Amplitude (pA)
Membrane potential (mV)
E
Conductance (pS)
E_{rev} (mV)
F
Amplitude (pA)
Membrane potential (mV)

not be estimated accurately. The second component, however, was well resolved, and corresponded to 5.1 ms in the sample histogram. The burst duration histogram for each recording was fit with two exponents and the average burst duration for the fully resolved component was 4.8 ± 1.1 ms (Figure 5.12A scatter plot).

I also examined the voltage-dependence of the αβδ combination. The burst duration histogram fit required two exponents at each potential, similar to the distribution at -100 mV. The brief component was not well resolved at any potential and was not considered in the voltage-dependence analysis. The average duration of the second component was determined at each potential (n=7 recordings), and the cumulative data plot was fit with an exponential function (Figure 5.12B). The fit to the overall data corresponded to an e-fold change in burst duration with every -769 mV hyperpolarization. These results indicated that the αβδ combination had a very weak voltage-dependence similar to the slow muscle AChR described in Chapter 4.

Single channel properties of the αβδγ combination

I next studied the αβδγ combination at the single channel level. As seen with the αβδ combination, low concentrations of ACh (300 nM) also effectively elicited single-channel events (Figure 5.13A). At -100 mV, however, the amplitude was conspicuously smaller for the αβδγ combination, and most events fell into a single amplitude class (Figure 5.13B). In eight of 10 recordings there was a secondary event class with a larger amplitude (Figure 5.13B). The larger amplitude events occurred infrequently and contributed an average of 3 ± 2% to the total number of events. The fit of the sample amplitude histogram indicated mean amplitudes of 5.5 pA and 8.4 pA for the primary and

Figure 5.12: Single-channel burst duration of the αβδ combination. A) Sample burst duration histogram for αβδ combination recording fit with two exponents at -100 mV. Peak of first exponential component fit corresponds to 0.18 ms, and peak of second exponential component fit corresponds to 5.1 ms. Scatter plot indicates the fit values for each component in 7 recordings at -100 mV (filled circles), and corresponding average value for each component ± SD (open circles). B) Cumulative voltage vs. burst duration plot corresponding to the average burst duration of 7 cells, at each potential, fit with a single exponential corresponding to an e-fold change in burst duration per -769 mV.

A

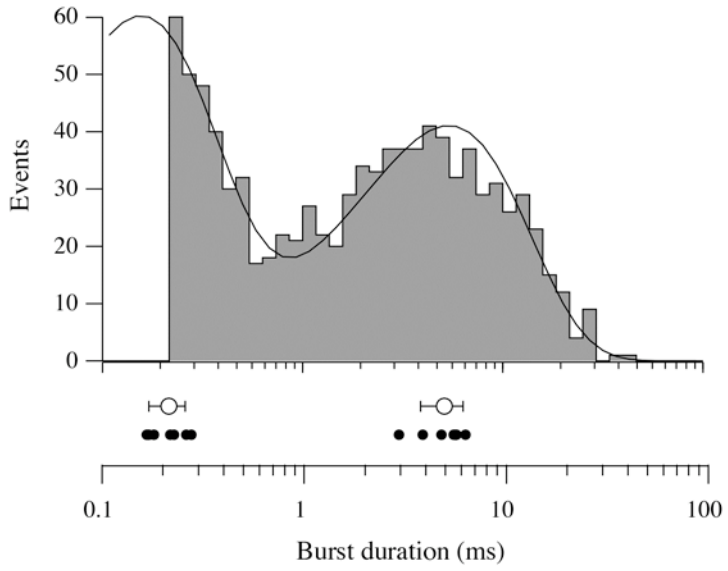
60
50
40
30
20
10
0
Events
0.1
1
10
100
Burst duration (ms)

B

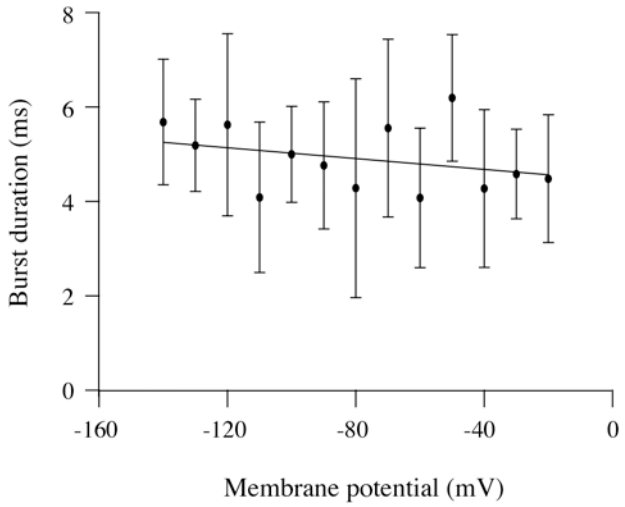
8
6
4
2
0
Burst duration (ms)
-160
-120
-80
-40
0
Membrane potential (mV)

secondary event classes, respectively (Figure 5.13B). The average amplitudes at -100 mV were 5.5 ± 0.2 pA, and 8.2 ± 0.2 pA for the primary and secondary event classes (Figure 5.13B, scatter plot; n=8 recordings).

Only the primary event class of events is thought to reflect function of the αβδγ subunit combination, because analysis of the secondary amplitude class reflected the conductance and burst duration characteristic of the αβδ combination described previously. The small number of events of the secondary class in these recordings suggested that αβδ channels formed infrequently even in the presence of the γ subunit. Examination of the single-channel properties of αβδγ is therefore limited to the primary amplitude class.

Amplitude distributions for the primary event class were constructed and fit for membrane potentials between -130 and -30 mV, in 10 mV increments. The current-voltage plot was fit by linear regression. The sample patch corresponded to a conductance of 51 pS and a reversal potential of -10 mV (Figure 5.13C). Current-voltage plots were constructed and fit for each of eight αβδγ recordings (Figure 5.13D). The channels had an average single-channel conductance of 51 ± 2 pS and a reversal potential of -10 ± 5 mV (Figure 5.13E). A cumulative current-voltage plot was also constructed, showing the average amplitude for all recordings at each potential (Figure 5.13F). The fit of the cumulative plot indicated an average single-channel conductance of 50 pS and a reversal potential of -11 mV.

The burst duration of the αβδγ receptor was determined at -100 mV. The burst duration histogram for each recording was fit to a single exponential function, and the fit of the example distribution in Figure 5.14A corresponded to a mean burst duration of 1.1

Figure 5.13: Single-channel properties of ACh-activated events of the αβδγ combination. A) Example traces indicating single-channel events at -100 mV. B) Amplitude histogram for all events at -100 mV for example recording in A, fit with two Gaussian functions corresponding to primary amplitude (black fit) and secondary amplitude class (red fit). Scatter plot indicates the average amplitude values for the primary class (black circles) and secondary class (red circles) for all recordings (n=10) at -100 mV, and the overall mean amplitude ± SD for each (open circles). C) Example current-voltage relations of the primary class, fit by linear regression. Fit corresponds to a slope conductance of 51 pS, and reversal potential of -10 mV. Dashed line indicates zero current level. D) Current-voltage relations for each of 8 recordings, with linear fit. E) Scatter plot indicating conductance and reversal potential values for the 8 recordings (filled circles) and corresponding average conductance and reversal potential values ± SD (open circles). F) Cumulative current-voltage relations for averaged data of all 8 recordings. Linear fit indicates overall conductance of 50 pS and reversal potential of -11 mV.

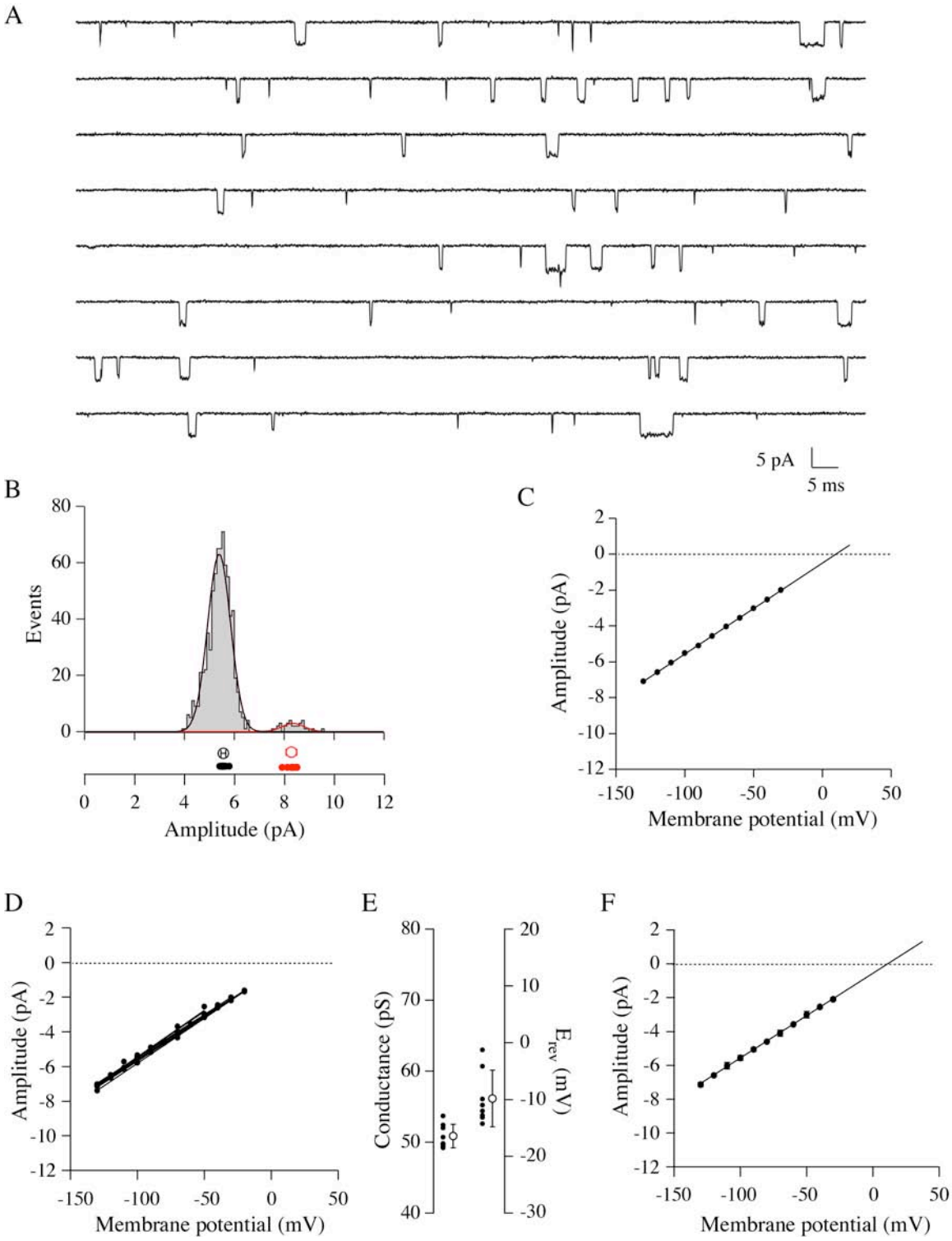
A
5 pA
5 ms
B
Events
Amplitude (pA)
C
Amplitude (pA)
Membrane potential (mV)
D
Amplitude (pA)
Membrane potential (mV)
E
Conductance (pS)
E_rev (mV)
F
Amplitude (pA)
Membrane potential (mV)

ms. The burst duration was fit similarly for each recording (n=11), and the mean burst durations are indicated in Figure 5.14A. When fit to a single exponential, the average burst duration of the αβδγ combination was 1.3 ± 0.4 ms (Figure 5.14A, scatter plot).

Most burst duration histograms for the αβδγ combination, however, were not described adequately by a single exponential, and fitting with two exponentials visually improved the fit (Figure 5.14B). Unlike the αβδ combination, I could resolve both components. In the sample histogram, fits corresponded to a mean burst duration of 0.63 and 1.8 ms, for the first (brief) and second (slow) components, respectively. The contribution of each component to the overall distribution was not equal. Based on the relative amplitudes, the brief component contributed 76% and the slow component only 24%. The burst distribution of each recording was fit to a double exponential and the resulting mean burst durations for both components are shown in Figure 5.14B (scatter plot). The average burst durations were 0.67 ± 0.3 ms for the briefer component and 2.7 ± 1.1 ms for the slower component (Figure 5.14B, scatter plot). The brief component contributed an average of 75 ± 11% of all the events while the second component contributed the remaining 25 ± 11%. A summary of the burst duration values determined by both single and double exponential fits is shown in Figure 5.14C.

The voltage-dependence of the burst duration for the αβδγ receptor was also determined. First, the burst duration distribution was fit with a single exponential for each recording (n=4), representing the overall change of the mean burst duration with voltage (Figure 5.14D). The cumulative burst duration vs. voltage plot was well described by a single exponential, and corresponded to an e-fold increase in burst duration per -141 mV hyperpolarization. Because the burst duration is best described by

Figure 5.14: Single-channel burst duration of the αβδγ combination. A) Sample burst duration histogram for αβδγ combination recording at-100 mV fit with a single exponent corresponding to an average burst duration of 1.1 ms. Scatter plot indicates the average burst duration values determined by a single exponential fit for 10 recordings (filled circles), and the mean burst duration value ± SD (open circle). B) Same distribution as in A, fit with two exponents. The peak of first exponential component fit corresponds to 0.63 ms, and peak of second exponential component fit corresponds to 1.8 ms. Scatter plot indicates the two fit values for each component in 10 recordings at -100 mV (filled circles), and corresponding average value for each component ± SD (open circles). C) Direct comparison of the burst duration values from A and B. Each component of the double exponential fit is plotted, for clarity. D) Cumulative voltage vs. burst duration plot corresponding to the average burst duration of 7 cells, at each potential, fit with a single exponential corresponding to an e-fold change in burst duration per -141 mV. E) Cumulative voltage vs. burst duration plot corresponding to the average burst duration of each of the two components of a double exponential fit, at each potential. Exponential fit indicates an average e-fold change in burst duration for the brief and longer component corresponding to -140, and -131 mV, respectively.

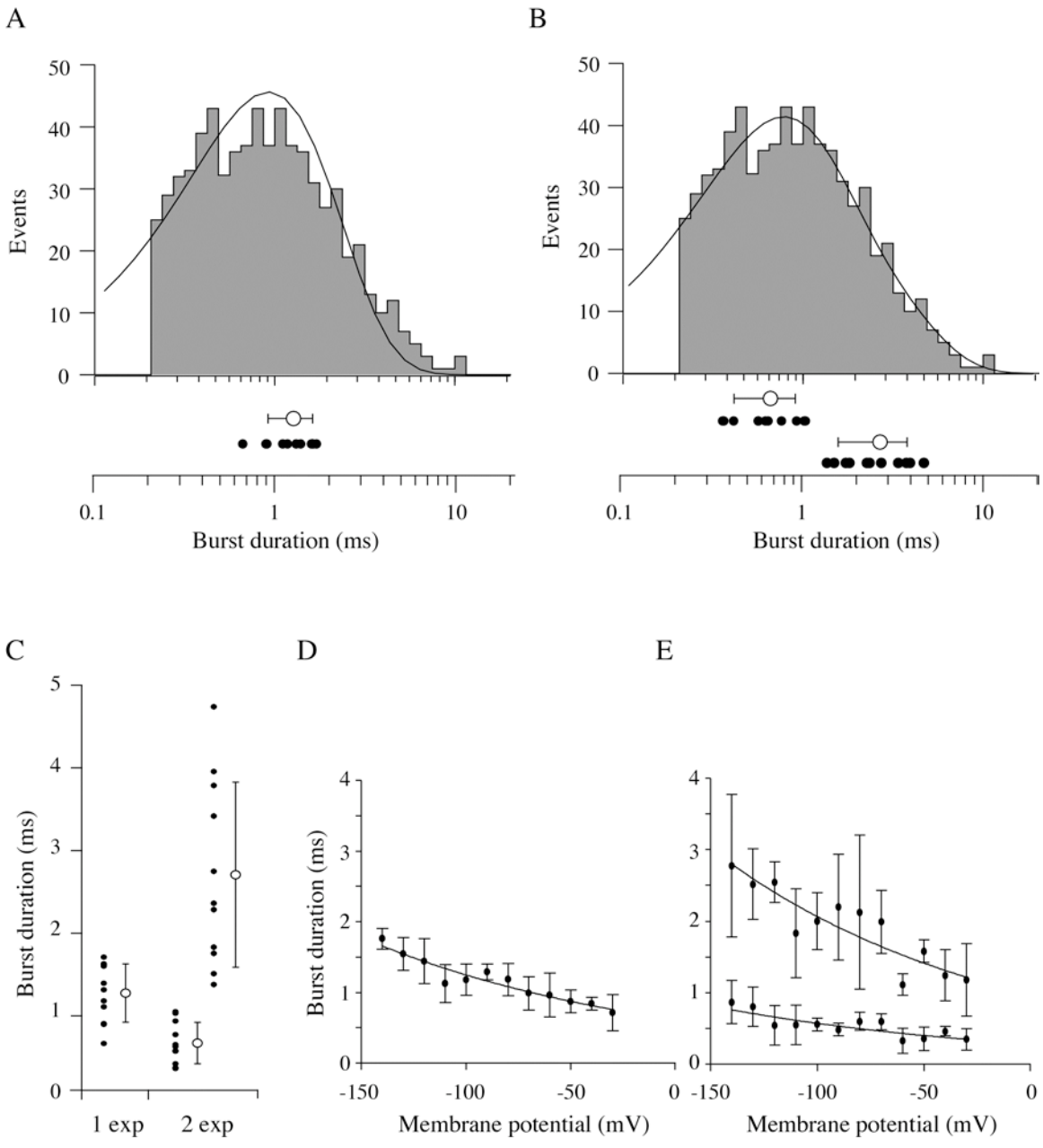
A
B
Events
Burst duration (ms)
C
D
E
Burst duration (ms)
1 exp
2 exp
Membrane potential (mV)

two components, the voltage-dependence of each component was also examined separately. Each burst duration distribution was refit with two exponents, and the cumulative data representing the average value for each component was fit separately (Figure 5.14E). Both the briefer and slower components were well described by an exponential fit corresponding to an e-fold change in burst duration per -140 mV, and -131 mV, respectively.

Single channel properties of the αβδε combination

Sample single-channel events recorded at -100 mV potential from oocytes injected with the αβδε combination are shown in Figure 5.15A. At all potentials tested, events fell into a single amplitude distribution and were fit with a Gaussian function (Figure 5.15B). The fit of the sample distribution in Figure 5.15B indicated an average amplitude of 7.1 pA at -100 mV. There was little variation in the amplitude distributions between recordings, so the average amplitude at -100 mV was 7.0 ± 0.3 pA (n=12 recordings). The amplitude of each recording and the overall average amplitude are shown below the histogram in Figure 5.15B.

Recordings were obtained from αβδε patches at membrane potentials between -160 and -30 mV, in 10 mV increments. The current-voltage plot for the sample events in Figure 5.15A was well fit by linear regression corresponding to a single-channel conductance of 67 pS (Figure 5.15C). Similar current-voltage plots were constructed for each of eight αβδε recordings (Figure 5.15D). The analysis indicated an average single-channel conductance of 66 ± 2 pS with a reversal potential of -6 ± 8 mV (Figure 5.15E, n=8 recordings). A cumulative current-voltage plot was also constructed, reflecting the

Figure 5.15: Single-channel properties of ACh-activated events of the αβδε combination. A) Example traces indicating single-channel events at -100 mV. B) Amplitude histogram for all events at -100 mV for example recording in A, corresponding to a mean amplitude of 7.1 pA. Scatter plot indicates average amplitude for all recordings (n=12) at -100 mV (open circles) and overall mean amplitude ± SD (closed circle). C) Current-voltage relations for a single recording, fit by linear regression. Fit corresponds to a slope conductance of 67 pS, and reversal potential of -4 mV. Dashed line indicates zero current level. D) Current-voltage relations for each of 8 recordings, with linear fit. E) Scatter plot indicating conductance and reversal potential values for the 8 recordings (filled circles) and corresponding average conductance and reversal potential values ± SD (open circles). F) Cumulative current-voltage relations for averaged data of all 9 recordings. Linear fit indicates overall conductance of 67 pS and reversal potential of -5 mV.

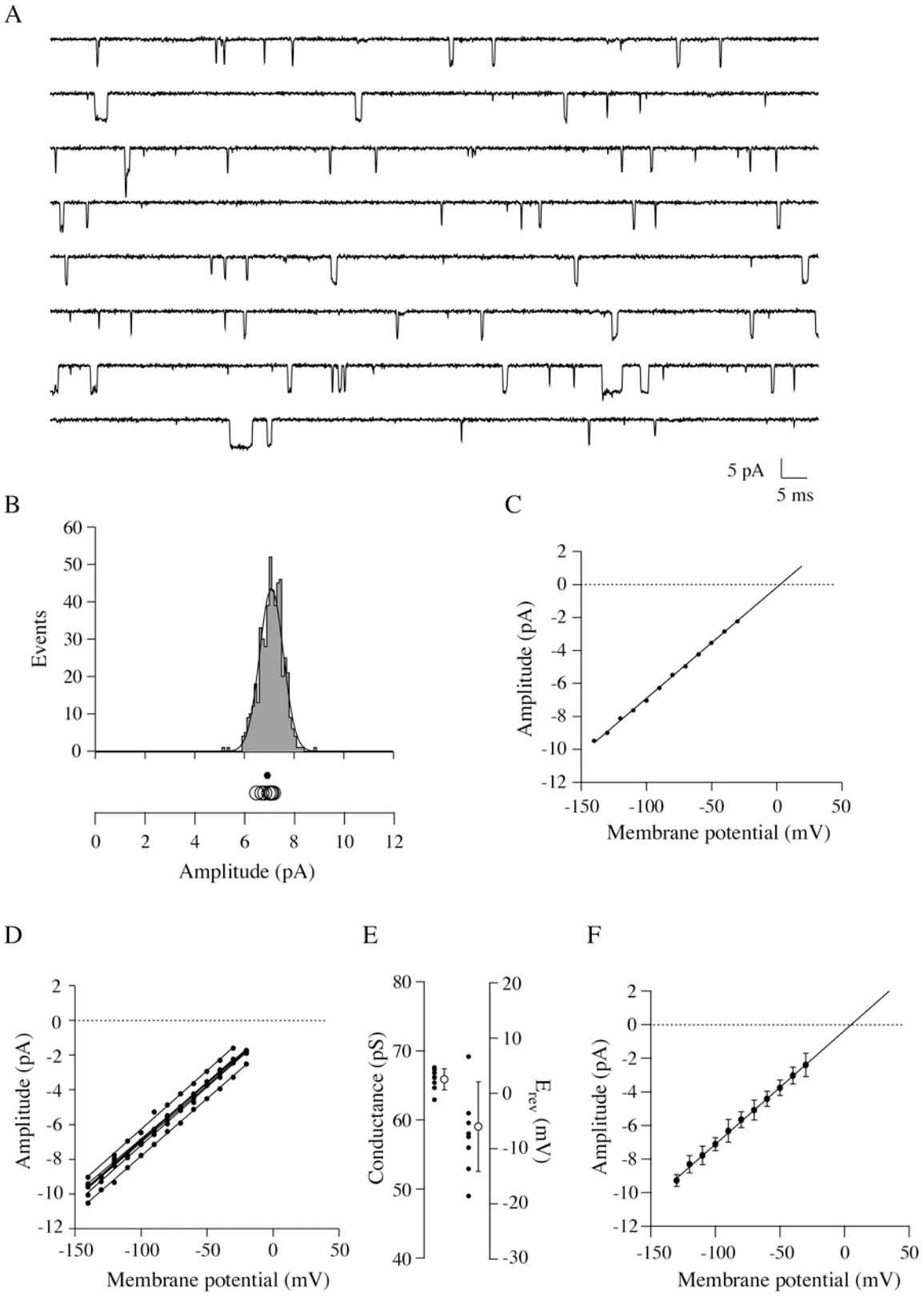
A
5 pA
5 ms
B
Events
Amplitude (pA)
C
Amplitude (pA)
Membrane potential (mV)
D
Amplitude (pA)
Membrane potential (mV)
E
Conductance (pS)
E_{rev} (mV)
F
Amplitude (pA)
Membrane potential (mV)

averaged amplitude of all recordings at each potential (Figure 5.15F). The fit to the cumulative data corresponded to an average single-channel conductance of 67 pS with a reversal potential of -5 mV, and was in good agreement with the values determined by individual recordings.

The burst duration of the αβδε channel was also determined. The burst duration distribution was fit with a single exponential, and corresponded to an average burst duration of 0.36 ms for the sample patch at -100 mV (Figure 5.16A). The mean burst duration values are shown below the sample histogram in Figure 5.16A. The average burst duration corresponded to 0.32 ± 0.05 ms (n=7 recordings).

Inspection of the fit in Figure 5.16A indicated that the distribution was better fit by two exponentials (Figure 5.16B). The two mean burst durations were 0.14 ms and 0.47 ms. The duration histogram for each recording was also fit with two exponentials components, and the component means are plotted below Figure 5.16B. The average duration of the briefest component corresponded to 0.16 ± 0.06 ms, and the longer component corresponded to 0.54 ± 0.2 ms. This indicated that there was a brief component of the distribution that was not well resolved, similar to the brief component seen in the αβδ combination. However, the second component of the αβδε duration histogram was also very brief at 0.54 ms. Because the error associated with fitting increases as the mean duration of the components converge (Sigworth and Sine, 1987), and also because the very brief component was not resolved, these conditions made it difficult to accurately fit the αβδε to two exponentials. The scatter in the values of the second component of the fit likely reflected the error in fitting with two exponents.

Figure 5.16: Single-channel burst duration of the αβδε combination. A) Sample burst duration histogram for αβδε combination recording fit with single exponent at -100 mV, corresponding to an average burst duration of 0.36 ms. Scatter plot indicates average burst duration values determined by single exponential fit for 7 recordings (filled circles), with mean value ± SD (open circle). B) Same distribution as in A, fit with two exponents. The briefest exponential component fit corresponds to 0.14 ms, and peak of second exponential component fit corresponds to 0.47 ms. Scatter plot indicates the two fit values for each component in 7 recordings at -100 mV (filled circles), and corresponding average value for each component ± SD (open circles). C) Scatter plot comparing the single exponential fit, the second component of the double exponential fit and the numerical mean burst time values determined for each recording (filled circles) with corresponding average ± SD values (open circles). D) Cumulative voltage vs. burst duration plot corresponding to the average burst duration of 7 cells, at each potential, determined by a single exponential fit (black) or by the numerical mean burst duration (red). The fit indicates an average e-fold change in burst duration for the exponential estimation corresponding to -156 mV, and an e-fold change per -185 mV for the numerical mean estimation.

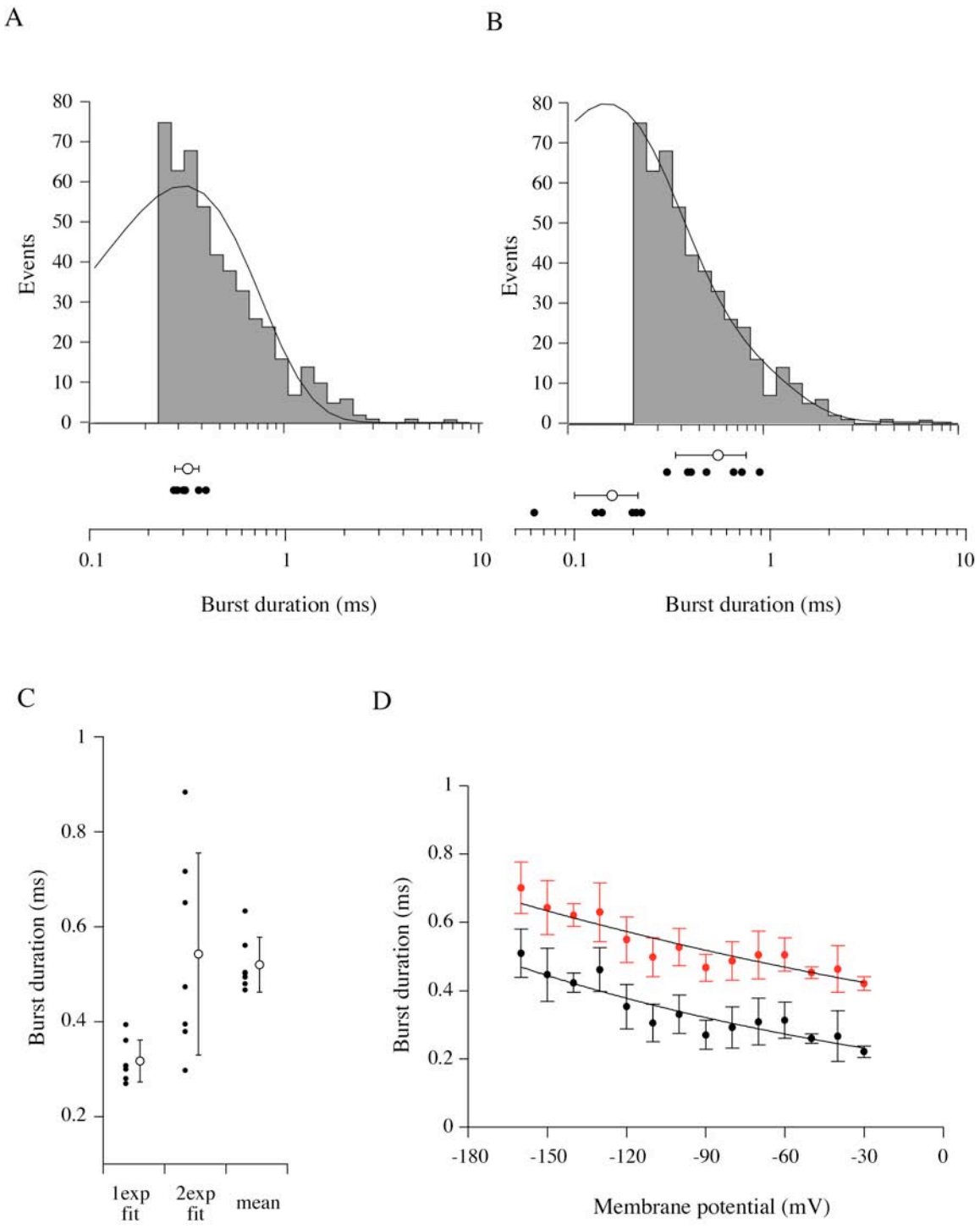
A
B
Events
Burst duration (ms)
C
D
Burst duration (ms)
1exp fit
2exp fit
mean
Membrane potential (mV)

For comparison with the fitted mean, I also determined the numerical average of the burst duration for each recording (Figure 5.16C). In the scatter plot shown, the mean of the distribution fit with a single exponential component is compared to the second component of the double exponential fit and the numerical mean burst duration. The average duration determined by the single exponential fit was left skewed, likely because of the excess brief events. However, the second component of the double exponential fit was relatively variable, likely due to the aforementioned fitting limitations. The numerical mean indicated the duration average was slightly longer than the single exponential fit, was comparable to the average value for the longest component, and was also relatively consistent between recordings. Due to the complications of fitting, I used the numerical average to indicate the average burst duration for the αβδε combination (0.52 ± 0.6 ms).

I was also interested in determining the voltage-dependence of the burst duration of the αβδε combination. Because of the complications with estimating the burst duration, I determined the voltage-dependence in two ways. First, I constructed and fit the burst duration distributions at each potential with a single exponential function, as in Figure 5.16A. The burst duration at each potential was averaged between the seven recordings to construct the cumulative plot in Figure 5.16D. The fit to the cumulative data indicated an e-fold increase in burst duration per -156 mV (n=7 cells) membrane hyperpolarization.

As a second means to estimate the voltage-dependence, I also determined the numerical mean burst duration at each potential for the same dataset. I constructed a cumulative voltage vs. burst duration plot using the average numerical mean burst

duration at each potential (Figure 5.16D). The fit of this relationship indicated an e-fold change in burst duration for every -185 mV. The two methods of voltage-dependence estimation were in reasonable agreement in light of the variability in burst duration values.

β1a subunit influence on αβδ type channel expression

Heterologous expression studies of the β1a subunit indicated that it likely did not function in the channel complex similarly to the β subunit. In all of these studies, however, I was examining β1a subunit function in the absence of the β subunit. I was curious, therefore, as to whether a combination with both the β1a and the β subunit might result in the formation of a previously unidentified AChR with unique single-channel properties. For these experiments, I injected equal amounts of both β subunits, in combination with the α, δ and γ subunits (αββ1aδγ), and used single-channel recordings to determine if a functionally unique channel expressed.

Single-channel events from oocytes injected with both β subunits resulted primarily in events corresponding to the αβδγ composition, with some contribution of αβδ (Figure 5.17A). However, the frequency at which αβδ events occurred, estimated by the percent contribution to the total number of events, was higher in these recordings than in injections of just αβδγ. Specifically, in oocytes also injected with the β1a subunit, the proportion of events belonging to the αβδ class was 23% of the sample frequency histogram shown in Figure 5.17C. For oocytes injected with only the αβδγ combination, the events belonging to the αβδγ amplitude class usually accounted for an average of 96% of the total events, and αβδ amplitude class accounted for the remaining

Figure 5.17: Single-channel properties in oocytes injected with both β subunits. A) Example recording at -100 mV from oocytes, indicating two single-channel event types corresponding to the αβδ channel (asterisks) and αβδγ channels. B) Sample amplitude histogram for a representative recording from the αβδγ combination, fit with two Gaussian functions that corresponding to 5% contribution of openings by the αβδ channel type, and 95% contribution by αβδγ channel type. C) Sample amplitude histogram for one recording at -100 mV from an oocyte injected with an equal ratio of αββ1aδγ subunits. The indicated fit corresponds to a 24% contribution by αβδ single-channel events, and 76% contribution by αβδγ events. D) Sample amplitude histogram for one recording at -100 mV from an oocyte injected with αββ1aδγ, with a 10-fold excess of β1a subunit. The indicated fit corresponds to a contribution of 49% by αβδγ events and 51% by αβδ events. E) Scatter plot indicating the fraction of αβδ single-channel events to the total number of events recorded at -100 mV for each injection type. Individual recordings are indicated by filled circles, alongside their respective mean ± SD values (open circles).

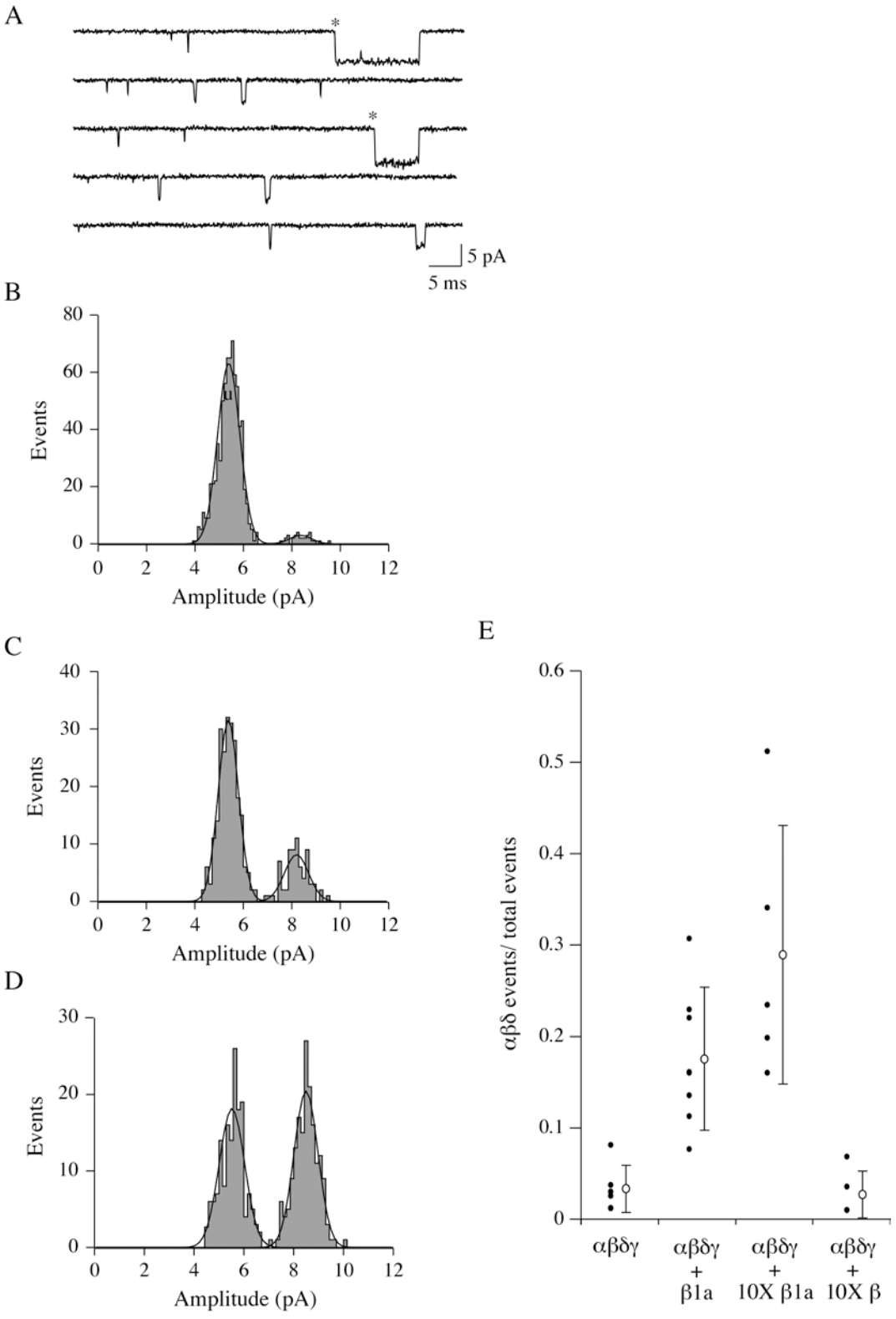
A
5 pA
5 ms
B
Events
Amplitude (pA)
C
Events
Amplitude (pA)
D
Events
Amplitude (pA)
E
αβδ events/ total events
αβδγ
αβδγ + β1a
αβδγ + 10X β1a
αβδγ + 10X β

4% (Figure 5.17B). The average percent contribution of αβδ events was 17 ± 8%, for oocytes co-injected with an equal ratio of β1a and β subunit RNAs.

To follow up on this unexpected finding, I compared the contribution of αβδ events during single-channel recordings of oocytes injected with αβδγ and either a 10-fold excess of β1a, or β RNA to α, β, δ and γ subunits. A sample amplitude histogram from these experiments showed nearly equal contributions of αβδ and αβδγ events (51% and 49%, respectively; Figure 5.17D). Recordings from oocytes injected with an excess of β1a indicated an average contribution of αβδ events of 29 ±14% (n=5 oocytes), while recordings from oocytes injected with a 10-fold excess of the β subunit did not resulted in elevated levels of αβδ events (4 ± 2%, n=5 oocytes). The percent contribution of αβδ in each condition is summarized in Figure 5.17E. In each condition, the overall frequency of events was similar.

These results suggested that the β1a subunit might play a role in promoting the formation of the αβδ receptor in the presence of the γ subunit.

Summary of results from Chapter 3 through Chapter 5

The single-channel properties of the reconstituted AChR combinations and the muscle AChRs are summarized in Table 5.1. The conductance values indicated are those estimated by the average ± SD of the linear fit to individual recordings for both reconstituted and on-cell AChR types. The burst duration values listed for reconstituted AChRs were those estimated by the average ± SD for the individual recordings at -100 mV. For consistency, the burst duration of muscle AChRs are those measured at the applied potential resulting in an estimated transmembrane potential of -100 mV; burst

duration averages at +50 and +40 mV applied potential were included for slow muscle AChRs, and burst duration averages at +20 mV applied potential were included for fast muscle AChRs. The voltage-dependence is summarized as to whether the relations were well described by an exponential function (exponential) or not (atypical).

The subunit composition of the fast muscle primary AChR class was likely αβδε, based on the similarity in conductance and burst duration values ($p=0.08$, and $p=0.07$, respectively). Although the αβδ combination could not be ruled out on the basis of conductance ($p=0.4$), the mean burst duration of the αβδ type was nearly seven-fold longer in duration than the fast muscle AChR ($p<0.0001$). The αβδγ combination represented a poor match for both conductance and burst duration ($p<0.0001$, both). Finally, both the fast muscle AChR and the αβδε combination demonstrated an exponential relationship between the burst duration and the voltage, typical of fast muscle AChRs.

The subunit composition of the slow muscle primary AChR was best represented by the αβδ combination when considering the average burst duration. The long burst duration of the slow muscle AChR cannot be accounted for by either the αβδε (or αβδγ ($p<0.0001$, both). However, the slow muscle AChR conductance estimate is less than that of the αβδ receptor ($p=0.03$). An explanation of this disagreement is presented in Chapter 6 suggesting that estimates of the slow muscle AChR by linear regression are inaccurate due to inward rectification of the channel. As with fast muscle, the αβδγ combination represents a poor match for both conductance and burst duration ($p<0.0001$, both).

Table 5.1: Summary of results from Chapters 3 through 5.

Source	Type	Representation (total events or amplitude)	Conductance	Kinetics (τ_{decay} or burst duration)	Voltage-dependence	
					Burst duration	Conductance
muscle synaptic events	fast	100%	-	brief (~0.5 ms)	-	
	slow	80-100%	-	long (~3 ms)	-	
muscle single channels	fast	90-100%	68 ± 4 pS	brief (~0.5 ms)	exponential	
	slow	80-100%	66 ± 2 pS	long (~3.5 ms)	atypical	
muscle single channels secondary class	fast	0-12%	51 ± 3 pS	intermediate (~1.2 ms)	-	
	slow	0-23%	70 ± 4 pS	brief (~0.5 ms)	-	
reconstituted single channels	αβδε	100%	66 ± 2 pS	brief (~ 0.5 ms)	exponential	
	αβδγ	95%	51 ± 2 pS	intermediate (~1.3 ms)	exponential	
	αβδ	100%	70 ± 5 pS	long (~4.5 ms)	atypical	
MO muscle synaptic events	ε					
	γ					

The reconstituted receptor profiles also provide insight into the possible identity of the infrequently observed secondary AChR classes on fast and slow muscle. For fast muscle, the secondary class is a good match for the αβδγ combination, in both conductance and burst duration. For slow muscle, the secondary AChR class properties are similar to those of both the primary class of AChR on fast muscle and the αβδε subunit combination in oocytes.

In summary, my single-channel studies suggested that each of the three combinations αβδ, αβδε and αβδγ were represented in the single-channel events on muscle. The αβδ and αβδε combinations, however, were responsible for the primary class of AChR on slow and fast muscle, respectively, and represent the channels whose kinetic properties define the synaptic current decay of each muscle type.

CHAPTER 6

Voltage-dependent rectification of zebrafish slow muscle AChRs

Single-channel measurements of AChR function in fast and slow skeletal muscles established that the different synaptic time course resulted from differences in the mean channel burst times. Heterologous expression of reconstituted AChRs of different subunit compositions pointed to likely structural candidates for these functional distinctions. Specifically, the αβδε channel was an excellent candidate for fast muscle AChRs on the basis of the three criteria I have examined: burst duration, conductance, and voltage-dependence of the burst duration.

In the case of the slow muscle AChR the αβδ channel was the best match in two of the three criteria examined: average burst duration, and voltage-dependence of the burst duration. There was an apparent difference, however, between the conductance of the native slow channel and the reconstituted αβδ channel (66 ± 2 pS for slow AChR, 72 ± 5 pS, $p = 0.03$). In this chapter, I provide a likely solution to this apparent difference through study of the current rectification of slow muscle AChRs and αβδ channel.

Rectification of slow muscle synaptic currents

The first indication that slow muscle AChRs might exhibit non-linear current-voltage relations came from study of the synaptic currents. In Chapter 3, I presented

studies of fast and slow muscle synaptic kinetics at a single membrane potential (-90 mV), to describe the difference in τ_{decay} between them. This was the potential at which previous examination of the τ_{decay} of slow and fast muscle was undertaken (Luna and Brehm, 2006). In the course of analyzing the kinetics of synaptic currents at different membrane potentials, I also examined the amplitude over a range of holding potentials. In Figure 6.1A, I have plotted the average amplitude of spontaneous miniature events at membrane potentials between -150 and 80 mV for seven fast muscle cells. At points between -20 mV and 20 mV, synaptic events were usually too small to detect. At positive membrane potentials, the fast synaptic currents reversed direction, and the current-voltage relationship is well described by a linear fit over the entire range of potentials (Figure 6.1A). These results agree with the previously published current-voltage relations for evoked synaptic currents in fast muscle (Wen and Brehm, 2005).

Surprisingly, similar experiments in slow muscle did not yield the expected linear current-voltage relationship for spontaneous synaptic events. The average amplitude for the synaptic events in slow muscle cells (n=10) was determined across a similar range of membrane potentials as for fast muscle (Figure 6.1B). Slow muscle events had a smaller amplitude than fast muscle events at -70 mV ($p=0.015$). However, at more hyperpolarized potentials, such as -150 mV, the events in slow muscle were nearly equal in amplitude to those of fast ($p=0.27$). At positive potentials, the outward currents were small and difficult to detect at potentials less than +60 mV. Overall, the relationship between the current and voltage was highly non-linear, requiring a 2^{nd} order polynomial fit (Figure 6.1B). A non-linear current-voltage relationship such as this one is generally referred to as inwardly rectifying.

Figure 6.1: Slow and fast muscle synaptic current-voltage relations. A) Average amplitude ± SD of synaptic events for 7 fast muscle cells at each potential, with linear fit shown. B) Current-voltage relations for the average amplitude ± SD of synaptic events for 10 slow muscle cells at each potential, with 2nd order polynomial fit shown.

A

Fast muscle

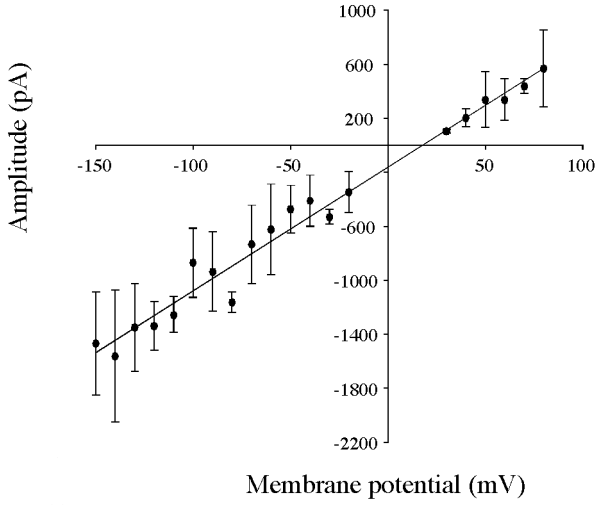

B

Slow muscle

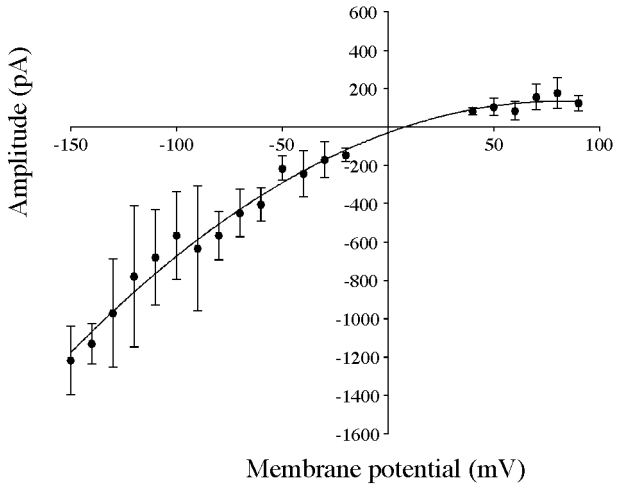

If non-linearity in the synaptic current amplitude reflects the single-channel function of the slow muscle AChR, inward rectification represented an unappreciated and fundamental distinction between the two types of AChRs. I therefore revisited the on-cell single-channel data, to determine if there was any evidence of inward rectification of slow muscle AChRs.

Evidence for slow muscle AChR single-channel rectification

During on-cell recordings from fast muscle, I sometimes attempted to record at very negative applied potentials (-80 to -150), in order to bring the transmembrane potential to positive values where single-channel AChR currents should reverse direction and become outward-going. Attempting to record at these negative applied potentials often resulted in loss of the patch, or entry into the whole-cell configuration. However, in the recordings where patch integrity was maintained, outward-going AChR currents were present in five of six fast muscle recordings (Figure 6.2A). In four of those five recordings, a sufficient number of outward-going events occurred at multiple potentials to construct a current-voltage plot (Figure 6.2B). Each recording was fit by linear regression across the entire range of applied potentials, and the slope indicated an average conductance of 63 ± 3 pS, and estimated V_{rest} of -81 mV. These values were similar to the estimates over the inward current range, and indicated that the current-voltage relations for fast muscle AChRs were linear over all ranges examined.

Similar attempts were made to record outward-going AChR currents from slow muscle at negative applied potentials; as seen with fast muscle, there was a tendency to lose recordings at these potentials. In seven cells, however, I was able to record at

Figure 6.2: Voltage-dependence of single-channel events in slow and fast muscle. A) Sample traces from an on-cell recording of fast muscle at the six applied potentials indicated. Estimated V_m indicates the difference between the applied potential and the estimated V_{rest} (-80 mV), for the each trace. B) Current-voltage relations for four fast muscle recordings where outward-going single-channel currents were present. C) Sample traces from an on-cell recording of slow muscle at the five applied potentials indicated. Estimated V_m calculated using the V_{rest} for this patch (- 40 mV).

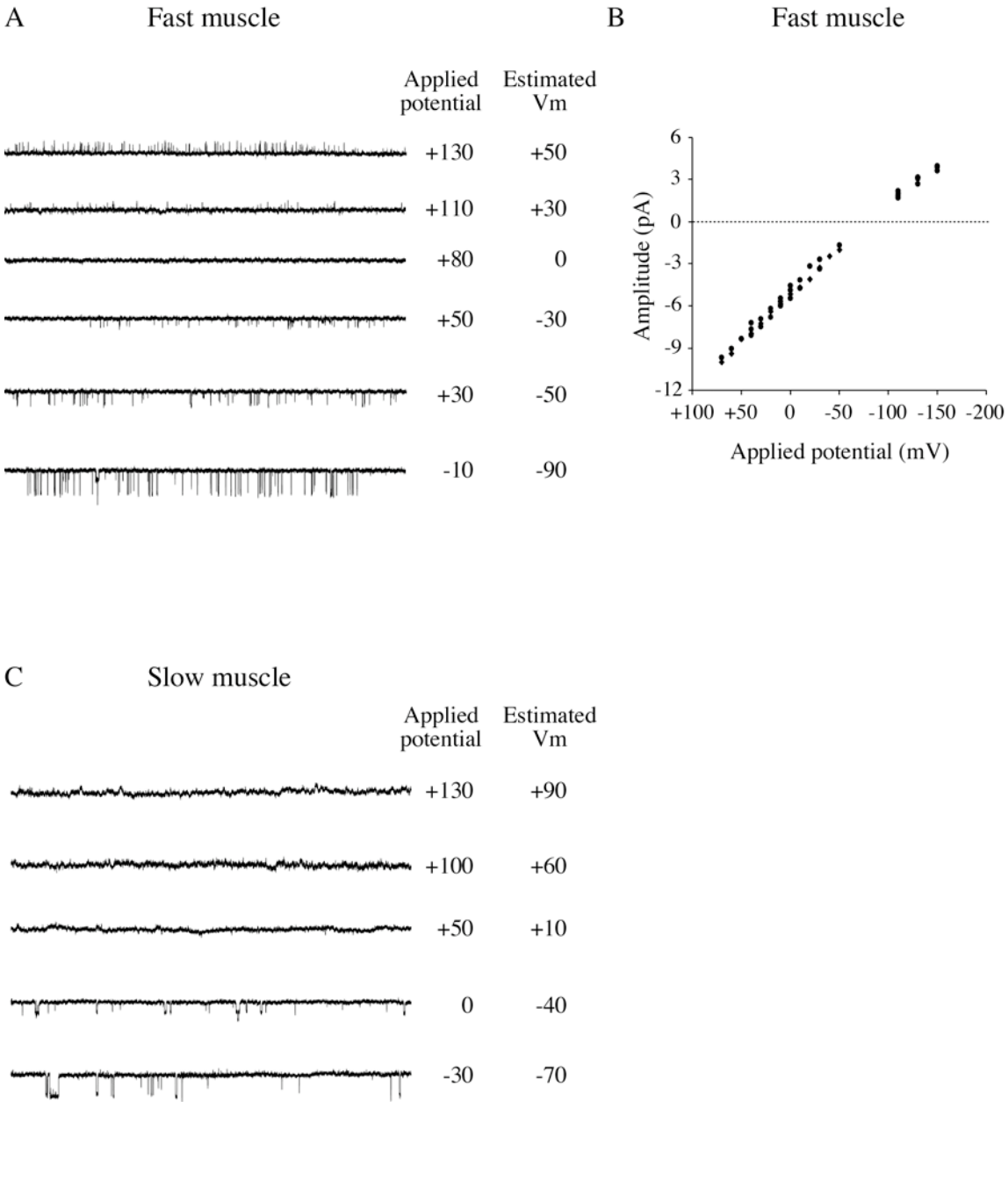
A
Fast muscle
Applied potential
Estimated Vm
+130
+50
+110
+30
+80
0
+50
-30
+30
-50
-10
-90
B
Fast muscle
Amplitude (pA)
6
3
0
-3
-6
-9
-12
+100 +50 0 -50 -100 -150 -200
Applied potential (mV)
C
Slow muscle
Applied potential
Estimated Vm
+130
+90
+100
+60
+50
+10
0
-40
-30
-70

multiple applied potentials between -80 and -130 mV. No evidence of outward-going primary class AChR events was seen at any of these potentials (Figure 6.2C). Based on the average estimates of V_{rest} by the single-channel conductance, slow muscle AChRs should exhibit prominent outward currents at applied potentials more negative than ~-60 mV. Based on the rate at which primary class events were detected at positive applied potentials in each patch (~3 Hz), I expected to detect ≥100 events at each negative applied potential, suggesting that ≥1000 outward-going events were missing from those seven cells. In one recording where both the primary and secondary event classes were present at positive applied potentials, rare outward-going events whose burst duration was extremely brief were detected at -100 mV (13 events). The short duration and infrequency of these events suggested they might belong to the secondary event class, but without two clear amplitude classes it was not conclusive. In two other patches where both event classes were present at positive applied potentials, no outward-going openings were detected at negative applied potentials. Due to the low frequency of the secondary event class in each recording (~0.3 Hz), it is uncertain as to whether the secondary class of slow muscle AChRs was able to pass outward current.

Although the absence of outward-going AChR events on slow muscle was consistent with inward rectification, I also wanted to determine if there was evidence that rectification occurred over the range of voltages where single-channel currents could be seen. Inward rectification can be manifest in two features of single-channel current-voltage relations; inability to pass outward current and a decrease in inward current conductance as the membrane potential approaches the reversal potential. In Chapter 4, I presented evidence that estimates of the V_{rest} for the cumulative current-voltage data for

primary and secondary class of slow muscle did not extrapolate to the same potential (Figure 6.3A). Because AChR subtypes share the same ion selectivity, it seemed unlikely this difference reflected a difference in reversal potential between the two channel types. The predicted differences in V_{rest} were also not attributable to different driving forces because the channel subtypes were in the same patch recording and thus subject to the same membrane potential. The average value indicated that V_{rest} was ~12 ± 4 mV more depolarized when estimated by the primary (-49 ± 4 mV) rather than the secondary class (-61 ± 6 mV; Figure 6.1B). The more depolarized estimates for V_{rest} may have been due to non-linear current-voltage relations of the primary class. To determine if the primary event class current-voltage relations were linear over the range shown, I compared the slope fit of the cumulative current-voltage relationship over the most positive (+110 to +80 mV), and most negative (+10 to -20 mV) applied potentials (Figure 6.3C). If the relationship were linear, the slope of the linear fit through the first four and the last four points should have converged; however, the fits indicated that the single-channel conductance decreased at more negative applied potentials (76 pS vs. 55 pS, ratio = 0.72).

Non-linear current-voltage relations were consistent with inward rectification, and suggested that a linear fit to the entire current-voltage relationship (66 pS) was only an estimate of the single-channel conductance. By contrast, the secondary conductance of slow muscle appeared to be essentially linear over the entire applied potential range (73 vs. 67 pS, ratio = 0.91; Figure 6.3D). The same analysis applied to fast muscle primary AChR events indicated that the current-voltage relations were also essentially linear over the entire applied potential range (71 vs. 64, ratio = 0.9). This analysis was consistent with the idea that the secondary class of AChRs in slow muscle and the primary class of

Figure 6.3: Current-voltage properties of ACh-activated single-channels on slow muscle. A) Cumulative current-voltage plot for primary (black circles) and secondary (red circles) event classes on slow muscle (as shown in Figure 4.4). B) Scatter plot indicating the V_{rest} values determined in each recording for the primary (black filled circles) and secondary (red filled circles), with their respective mean values ± SD (open circles). C) Cumulative current-voltage plot for primary event class, fit separately by linear regression over the most positive and negative holding potentials. The fits indicate 76 pS and 55 pS single-channel conductances, respectively. D) Cumulative current-voltage plot for secondary event class, fit as in C. The fits indicate a conductance of 73 pS over the most positive and 67 pS over the most negative applied potential ranges.

A

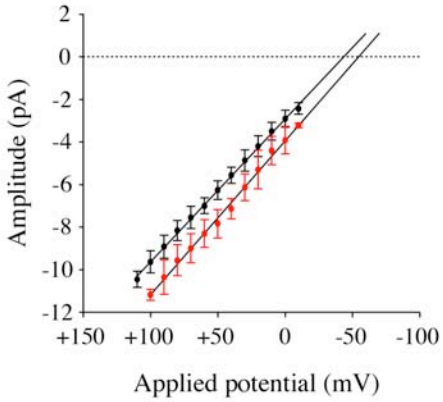
2
0
-2
-4
-6
-8
-10
-12
Amplitude (pA)
+150
+100
+50
0
-50
-100
Applied potential (mV)

B

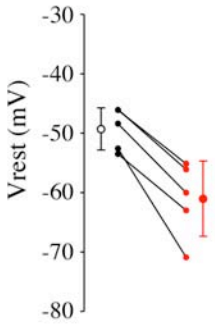
-30
-40
-50
-60
-70
-80
Vrest (mV)

C

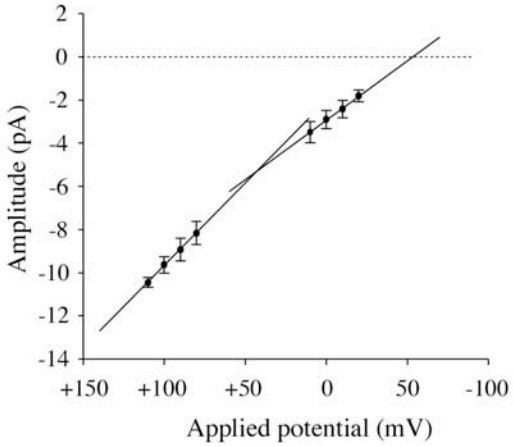
2
0
-2
-4
-6
-8
-10
-12
-14
Amplitude (pA)
+150
+100
+50
0
50
-100
Applied potential (mV)

D

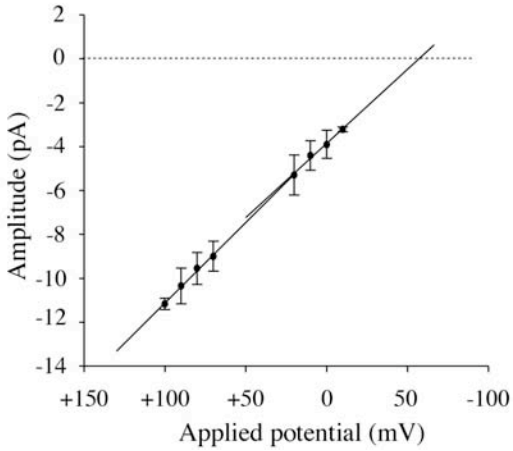
2
0
-2
-4
-6
-8
-10
-12
-14
Amplitude (pA)
+150
+100
+50
0
50
-100
Applied potential (mV)

AChRs in fast muscle were the same. Furthermore, it suggested that the primary class of AChRs on slow muscle was likely the only AChR class for which inward rectification was seen.

The αβδ channel exhibits inward rectification

The evidence from both slow muscle synaptic events and single-channel analysis suggested that the primary class of events on slow muscle AChRs were inwardly rectifying. It was therefore important to determine whether the αβδ subunit combination also exhibited non-linear current-voltage relations, as another point of comparison to the slow muscle AChR function.

For these studies, I returned to two-electrode voltage-clamp analysis of the ACh-activated macroscopic currents in oocytes. To measure the voltage-dependence of the current, I applied a saturating concentration of ACh (30 μM), and after the recording reached a plateau current amplitude, I ramped the membrane potential from -80 to +80 mV, at 80 mV/second. To account for the current generated by leak and voltage-activated conductances, I recorded a voltage ramp before application of ACh, and then subtracted the baseline record from the ACh-activated record. An example of both the baseline ramp, and ACh-activated ramp for the αβδε and αβδ combinations are shown in Figure 6.4A and B. A single leak-subtracted voltage ramp experiment for each combination, αβδ, αβδγ and αβδε, is shown in Figure 6.4C. For each oocyte, a similar peak inward current was produced at -80 mV (~6 μA), but the αβδ combination was the only channel type that did not continue to pass current at the positive potentials.

Figure 6.4: Current-voltage relations of reconstituted AChRs. A) Single voltage-ramp of the αβδε combination before (green) and during (black) ACh application. B) Sample voltage-ramp of the αβδ combination before (green) and during (black) ACh application. C) Leak-subtracted voltage-ramp for oocytes injected with αβδ (red), αβδε (black) and αβδγ (grey) combinations. D) Current-voltage plot of the data acquired during the voltage-ramp shown in C. E) Sample single-channel events from an outside-out patch recording of the αβδ combination, at indicated membrane potentials. F) Current-voltage relations for four recordings where outward and inward single-channel events were measured.

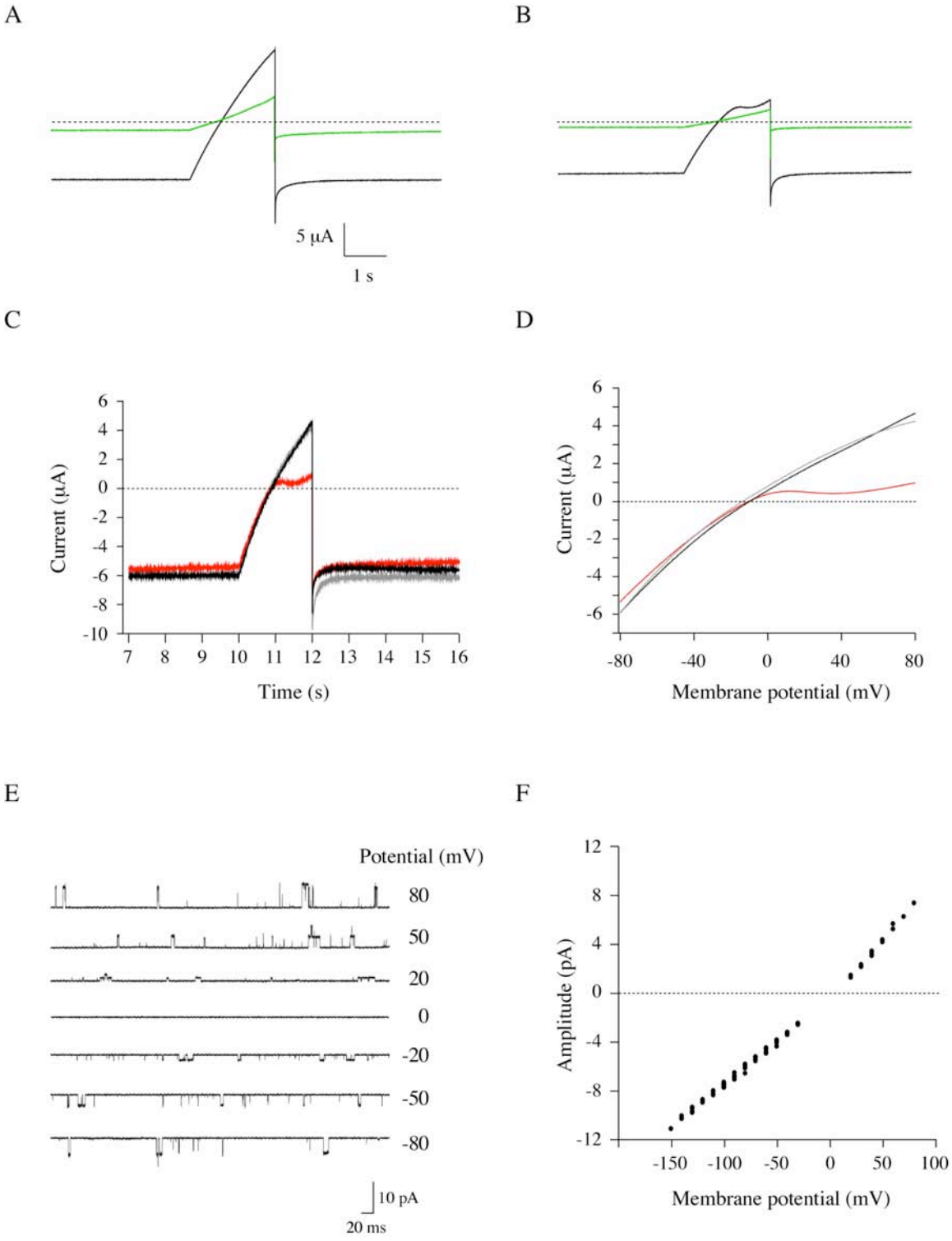
A
B
5 µA
1 s
C
D
Current (µA)
Time (s)
Current (µA)
Membrane potential (mV)
E
F
Potential (mV)
80
50
20
0
-20
-50
-80
10 pA
20 ms
Amplitude (pA)
Membrane potential (mV)

Moreover, the current-voltage plot constructed from the ramp data indicated that the αβδ channel exhibited inwardly rectifying current-voltage relations (Figure 6.4D).

The inward rectification of the αβδ channel did not appear to be an intrinsic property of the receptor; single-channel events recorded from outside-out patches of oocytes expressing the αβδ combination did not show rectification (Figure 6.4E). Current-voltage relations were constructed for the four patches where the αβδ receptor was tested at positive potentials, and fits to the individual recordings indicated that the average single-channel conductance of outward currents (100 ± 8 pS) was greater than the inward conductance (70 ± 1 pS; Figure 6.4F).

Summary of results from Chapter 3 through Chapter 6

The voltage-dependent properties reported in this chapter are summarized In Table 6.1 for comparison with the results obtained in previous chapters.

Table 6.1: Summary of results from Chapters 3 through 6.

Source	Type	Representation (total events or amplitude)	Conductance	Kinetics (τ_{decay} or burst duration)	Voltage-dependence: Burst duration	Voltage-dependence: Conductance
muscle synaptic events	fast	100%	-	brief (~0.5 ms)	-	-
	slow	80-100%	-	long (~3 ms)	-	-
muscle single channels	fast	90-100%	68 ± 4 pS	brief (~0.5 ms)	exponential	linear
	slow	80-100%	66 ± 2 pS	long (~3.5 ms)	atypical	inwardly rectifying
muscle single channels secondary class	fast	0-12%	51 ± 3 pS	intermediate (~1.2 ms)	-	-
	slow	0-23%	70 ± 4 pS	brief (~0.5 ms)	-	linear
reconstituted single channels	αβδε	100%	66 ± 2 pS	brief (~ 0.5 ms)	exponential	linear
	αβδγ	95%	51 ± 2 pS	intermediate (~1.3 ms)	exponential	linear
	αβδ	100%	70 ± 5 pS	long (~4.5 ms)	atypical	inwardly rectifying
MO muscle synaptic events	ε					
	γ					

CHAPTER 7

Molecular identity of fast and slow muscle AChR types

Measurement of AChR subunit RNA abundance in zebrafish

In the previous chapters, comparisons of the characteristics of the native muscle AChRs and the reconstituted AChRs suggested that fast muscle synaptic currents were due primarily to the $\alpha_2\beta\delta\varepsilon$ receptor and that slow muscle currents were primarily due to the $\alpha_2\beta\delta_2$ receptor. To examine whether differences in subunit transcript levels could explain the formation of these two isoforms, I collaborated with Drs. Fumihito Ono and Jason Urban to determine the subunit expression in whole zebrafish embryos throughout development, and then to determine the relative expression in slow and fast muscle cells.

The Ono lab used quantitative PCR measurements of the respective cDNAs to examine the abundance of each subunit transcript in the RNA extracts of whole embryos between the ages of 24 hpf, and 504 hpf (Figure 7.1A). Only the transcripts encoding the four subunits ε, γ, β1a and β were examined, because my data indicated α and δ subunits were requisite subunits for all muscle AChR function. Furthermore, mutants deficient in α and δ subunits indicate that each is requisite for AChR function in both slow and fast muscle (Sepich et al, Ono et al). The qPCR results indicated that all four transcripts were expressed, to varying degrees, throughout the first three weeks of zebrafish development (Figure 7.1A). The transcript levels are indicated as the relative abundance (in copy

Figure 7.1: Developmental pattern of zebrafish AChR subunit expression A) Quantitative PCR measurements from cDNA pools of ~20 zebrafish embryos. Target transcript levels are expressed as copy number relative to an elf1a transcript that should be expressed uniformly throughout development. B) Quantitative PCR measurements of zebrafish subunit cDNAs from RNA purified from adult zebrafish. Average copy number ± SEM for all values.

A

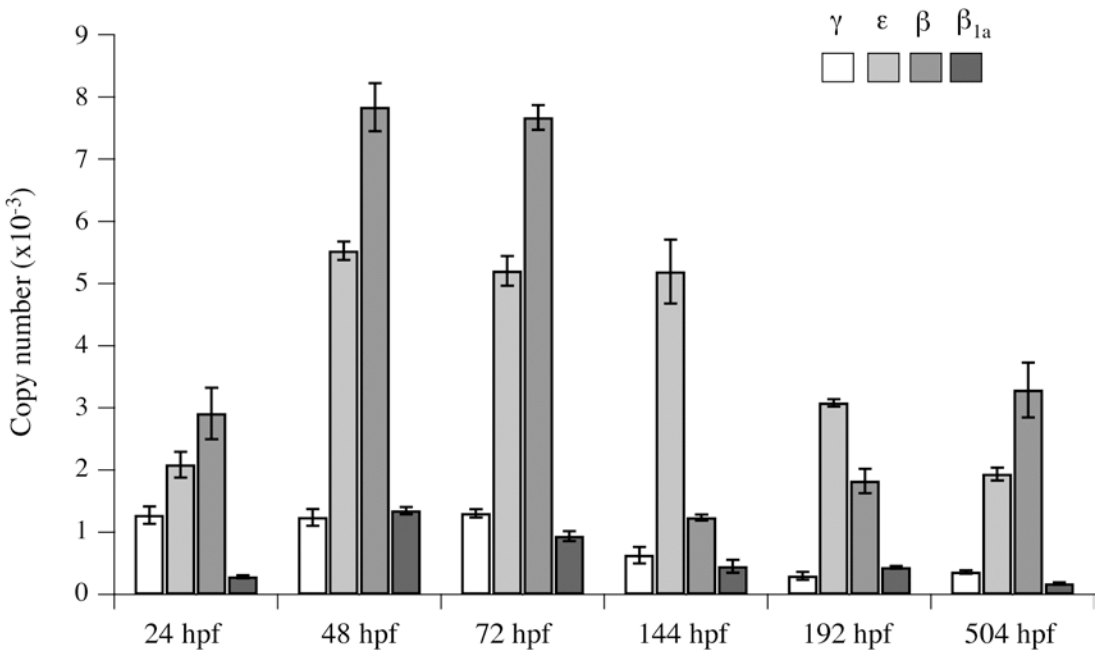
γ ε β β1a
Copy number (x10-3)
0
1
2
3
4
5
6
7
8
9
24 hpf
48 hpf
72 hpf
144 hpf
192 hpf
504 hpf

B

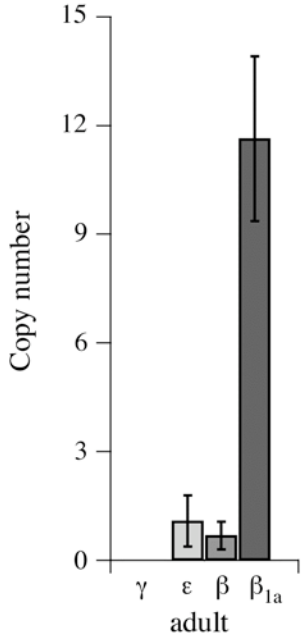
Copy number
0
3
6
9
12
15
γ ε β β1a
adult

number) of the target transcript compared to the copy number of the control transcript elongation factor 1 alpha (elf1a; see Materials and Methods). Elf1a represents a validated reference gene for qPCR analysis of zebrafish tissue (Tang et al, 2007). Although each transcript is most abundant at 48 hpf, the β and ε transcripts were 5-10 fold more abundant than either γ or β1a transcripts. For all subunits, the expression levels gradually declined after 48 hpf over the next three weeks, with β and ε remaining ~10-fold more abundant than either γ or β1a, at each time point. Transcript levels were also measured in adult fish (Figure 7.1B), and only the γ subunit transcript was not detected in the adult animal. Surprisingly, the amount of β1a transcript present in the adult fish was much greater than either ε or β, representing a relationship very different than that seen during development.

Having shown that all of the AChR subunit transcripts could be detected in whole zebrafish through development, I returned to the original question of slow vs. fast muscle. At the single developmental time point of 72 hpf, corresponding to the time at which electrophysiological analysis was performed, slow and fast muscle cells were individually suctioned into glass electrodes. The RNA was extracted from a small number of pooled cells (~10 to 20) and cDNA was generated for quantitative real time PCR (qPCR) measurements using primers specific for γ, ε, β, β1a, and δ subunits. For each experiment (n=5), the average copy number of four replicate reactions was determined by the Ono lab. The copy number for each transcript was normalized to the total copy number for all subunits in each experiment to reduce variability due to differences seen between cell collection experiments (see Materials and Methods).

Figure 7.2: Relative expression levels of zebrafish AChR subunits in fast and slow muscle. A) Fast muscle. B) Slow muscle. C) Relative amounts of slow and fast muscle subunit cDNAs. Average relative copy number ± SEM for all values.

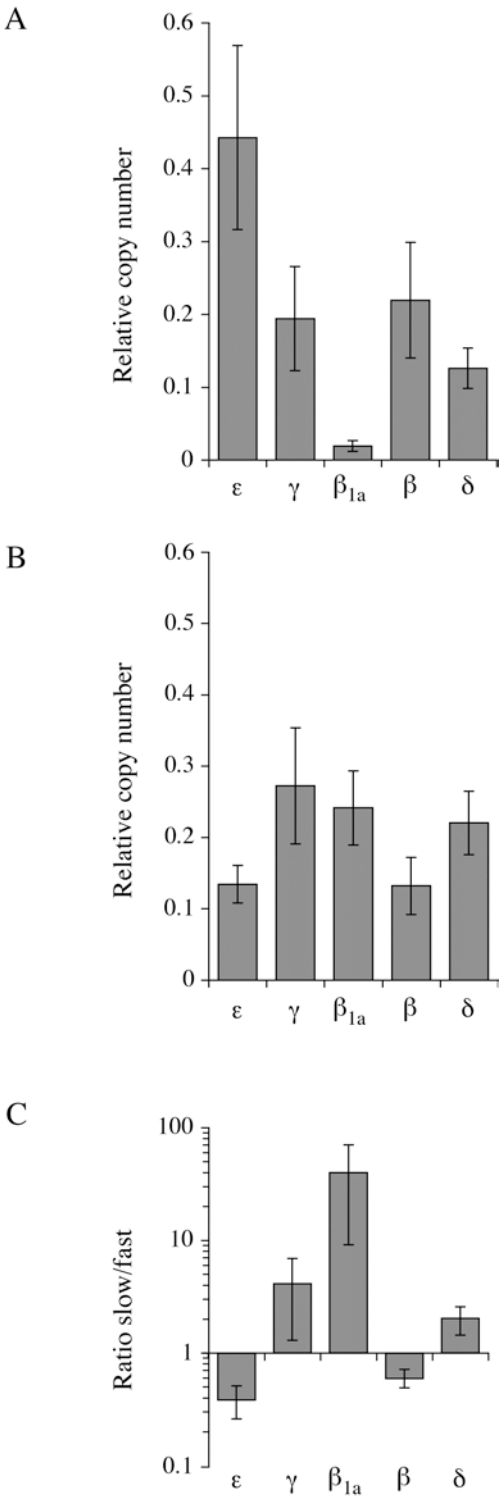
A
Relative copy number
0.6
0.5
0.4
0.3
0.2
0.1
0
ε
γ
β1a
β
δ
B
Relative copy number
0.6
0.5
0.4
0.3
0.2
0.1
0
ε
γ
β1a
β
δ
C
Ratio slow/fast
100
10
1
0.1
ε
γ
β1a
β
δ

Measurements from fast muscle cDNAs revealed all of the transcripts with β1a present at extremely low levels (Figure 7.2A). Similar analysis in slow muscle also indicated the presence of all of the subunit mRNAs, but this time, β1a was expressed to levels equivalent to β, δ, and γ mRNAs (Figure 7.2B). Normalized signals for each subunit cDNA were compared for each experiment (Figure 7.2C). This comparison indicated that β1a transcript was most enriched in slow muscle at a level 40-fold higher than in fast muscle. For comparison, the γ subunit and δ were only four-fold and two-fold more abundant in slow muscle, respectively. The β subunit was nearly equally represented between types, but 1.5-fold more abundant in fast muscle. As expected, the ε subunit was better represented in fast muscle where it was three-fold more abundant than in slow muscle.

Targeted subunit knockdown in vivo

Knockdown of subunit RNA was used to examine the contribution of each subunit to the synaptic current *in vivo*. Morpholinos (MOs) are a commonly used RNA knockdown strategy employed in zebrafish embryos to evaluate the role of gene products during development. MOs are antisense oligonucleotides that bind RNA targets and reduce protein levels by one of two mechanisms. MOs can be designed to bind to a sequence upstream of the ATG initiation site of the mRNA. In this case, the MO blocks protein synthesis through steric hindrance of translational machinery. Alternatively, MOs are designed to bind either splice donor or acceptor sites on the pre-mRNA transcript and interfere with the interaction of the splice machinery with the transcript. Splice-site MOs

often result in transcript degradation of aberrantly spliced products, or in final proteins that are non-functional due to deletions, insertions and frame-shift errors.

For subunit disruption *in vivo,* MOs were designed for either translational disruption or splice disruption, and optimal target sequences were chosen according to the manufacturers suggestion (GeneTools). For reference, the sequence of each MO used is included in the final summary table (Table 7.1).

All embryos were injected with MOs at the one-cell stage, approximately 30 minutes after fertilization. Injected embryos were examined over the first 96 hpf for effects on motor function and embryo morphology. These qualitative observations are also included in the summary in Table 7.1. The amount injected varied for each MO (between 1 and 12 ng per embryo), and in general, the highest amount that still rendered embryos viable for recordings was used. Analysis of the muscle synaptic currents was performed at 72-80 hpf, the same time point for all previous comparisons. WT synaptic currents measurements are also presented for comparison.

MO knockdown of the α subunit in vivo

I first assessed the effect of a translation site MO targeting the α subunit in both slow and fast muscle. Because the α subunit is essential for all AChR function, I expected an effect on synaptic currents in both muscle types, reflecting a reduction in synaptic current amplitude. Both synaptic current decay kinetics and amplitude were determined as previously described, and individual events were well described by a single exponential over 10-90% of the decay phase. Fast muscle synaptic currents were examined first, and the average τ_{decay} (n=7 cells) was similar to the WT average values

Figure 7.3: Fast and slow muscle synaptic current properties in embryos treated with α subunit MO. A) Average synaptic current τ_{decay} values for each fast muscle cell (filled circles), and overall average ± SD (open circles), at -70 mV. B) Average synaptic current amplitude for each fast muscle cell (filled circles), and overall average ± SD (open circles) at -70 mV. C) Average synaptic current τ_{decay} values for each slow muscle cell (filled circles), and overall average ± SD (open circles), at -70 mV. D) Average synaptic current amplitude for each slow muscle cell (filled circles), and overall average ± SD (open circles) at -70 mV.

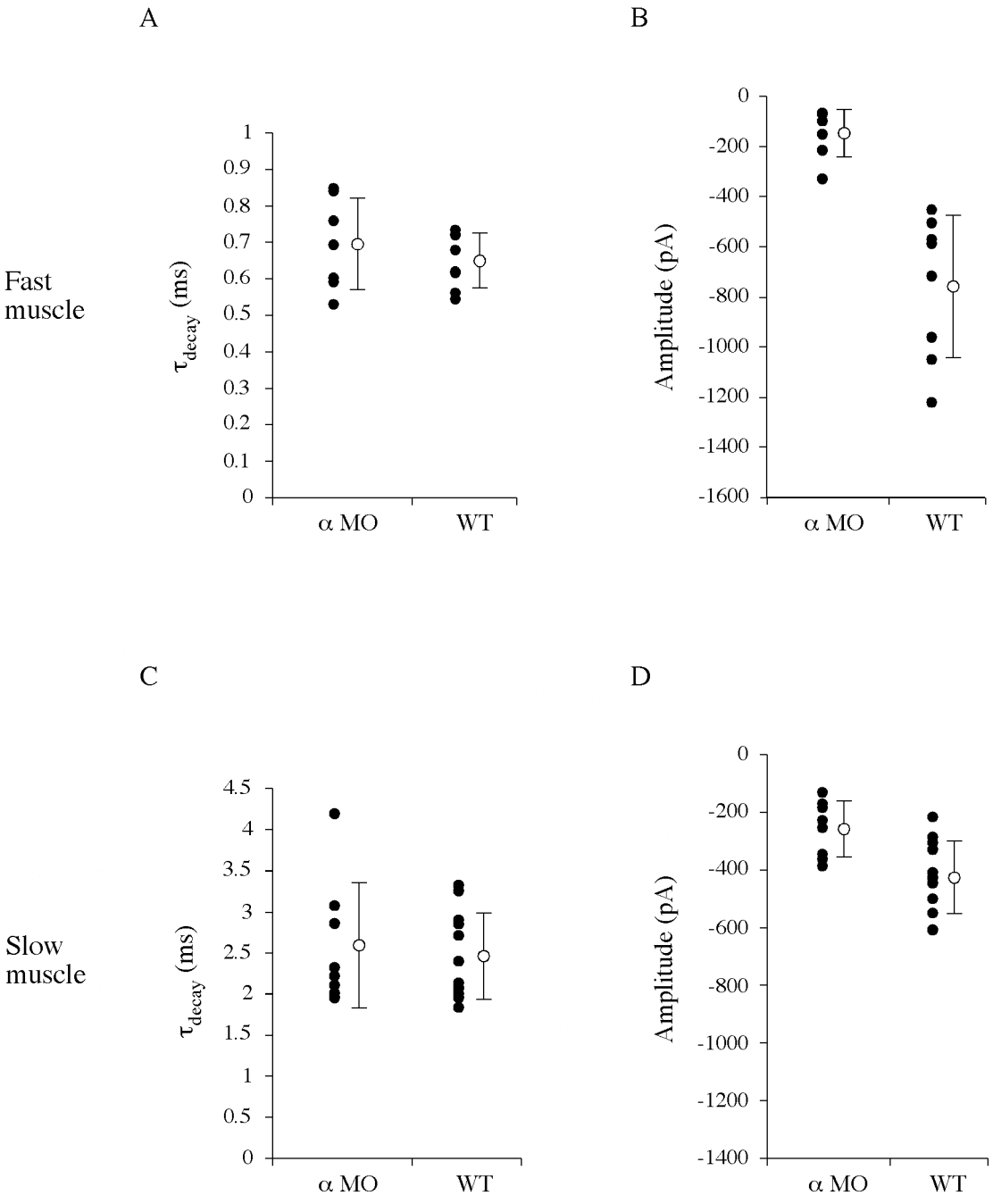
A
B
Fast muscle
τ_{decay} (ms)
Amplitude (pA)
α MO
WT
C
D
Slow muscle
τ_{decay} (ms)
Amplitude (pA)
α MO
WT

(Figure 7.3A). However, as predicted, the amplitude of synaptic currents was significantly decreased (Figure 7.3B, $p<0.001$). Together, these results suggested that reduction of the α subunit resulted in fewer fast muscle AChRs that had unaltered kinetic properties.

Similar analysis was performed for slow muscle. In eight recordings, the τ_{decay} values estimated for slow muscle synaptic currents were unchanged by the α MO (Figure 7.3C). However, as seen for fast muscle, the amplitude of slow muscle synaptic currents in α MO fish was significantly decreased, compared to WT (Figure 7.3D, $p=0.003$). These results are consistent with the hypothesis that the α subunit is required in formation of both fast and slow muscle AChRs but does not impart the kinetic distinction between the AChR types.

MO knockdown of the γ subunit in vivo

The next subunit targeted for knockdown was γ. The αβδγ subunit combination represents the channel type that I originally hypothesized was responsible for slow muscle AChR kinetics, due to its long burst time in other vertebrate systems. Although the single-channel analysis indicated that the reconstituted αβδγ receptor properties did not match those of the slow muscle AChR, it remained possible that the characteristics of the αβδγ channel were altered by post-translational modifications in zebrafish muscle cells. Therefore, MO knockdown was used to investigate whether the γ subunit was necessary to form either slow or fast muscle AChRs *in vivo*.

The first MO tested was a translational site MO (ATG_1). In the eight fast muscle cells examined, the synaptic current τ_{decay} values and the average amplitudes were similar

Figure 7.4: Fast and slow muscle synaptic current properties in embryos treated with γ subunit MOs. A) Average synaptic current τ_{decay} values for each fast muscle cell (filled circles), and overall average ± SD (open circles), at -70 mV. B) Average synaptic current amplitude for each fast muscle cell (filled circles), and overall average ± SD (open circles) at -70 mV. C) Average synaptic current τ_{decay} values for each slow muscle cell (filled circles), and overall average ± SD (open circles), at -70 mV. D) Average synaptic current amplitude for each slow muscle cell (filled circles), and overall average ± SD (open circles) at -70 mV.

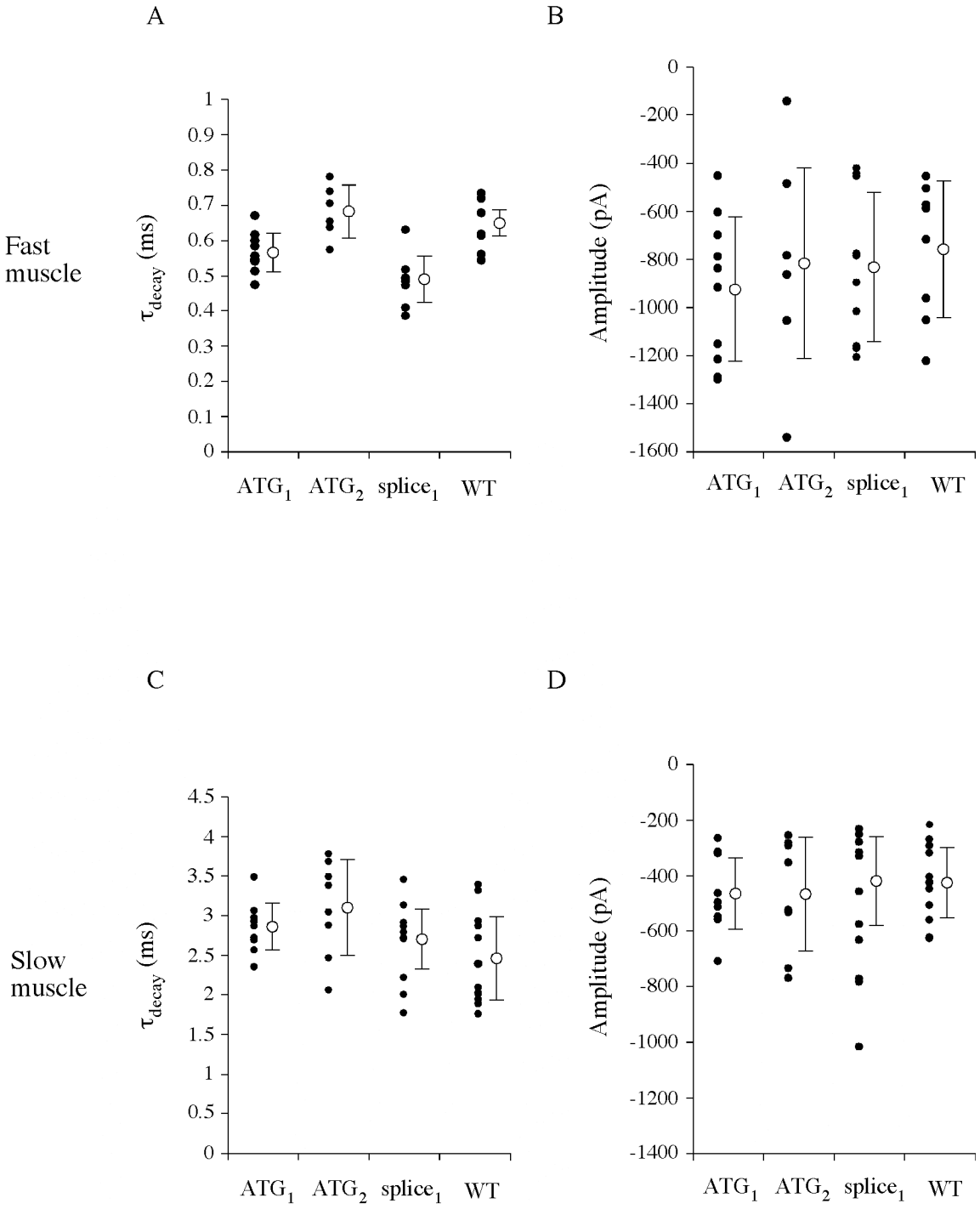
A
B
Fast muscle
τ_{decay} (ms)
Amplitude (pA)
ATG$_1$ ATG$_2$ splice$_1$ WT
C
D
Slow muscle
τ_{decay} (ms)
Amplitude (pA)
ATG$_1$ ATG$_2$ splice$_1$ WT

to those of WT (Figure 7.4A and B, ATG_1). Recordings from slow muscle cells also indicated that synaptic current τ_{decay} and amplitude was unchanged (Figure 7.4C and D, ATG_1).

Because there was no obvious change in the synaptic current properties of γ ATG_1 MO injected fish, I tested another translational site MO (ATG_2) that binds to a non-overlapping sequence further upstream of the ATG_1 site, in order to confirm these results. Analysis of γ ATG_2 injected fish yielded similar results to ATG_1 injections (Figure 7.4A-D, ATG_2). Together, these results suggested that the γ subunit did not play a role in determining the synaptic current properties of either muscle cell type, consistent with the single-channel analysis. However, the effectiveness of the translation site MOs was not confirmed. To address this problem, I also tested two splice site MOs ($splice_1$ and $splice_2$), as an independent measure of γ MO efficacy. Because splice site MOs cause alterations in the sequence of the target transcript, it is possible to assay their effect on γ transcript directly.

As seen for translation site MOs, analysis of the synaptic current properties in $splice_1$ MO injected fish yielded values similar to those in WT fish (Figure 7.4A-D, $splice_1$). To confirm that the $splice_1$ MO was targeting and disrupting the γ transcript, PCR was used to inspect the region of the γ transcript where the $splice_1$ MO was predicted to cause errors. The $splice_1$ MO targeted the junction of exon 8 and intron 8, and so is termed a splice donor site MO. This sequence was chosen because this region of the transcript encodes a transmembrane domain essential to formation of the channel pore (M2 domain), and was therefore necessary for proper function of every AChR subunit. Although the coding sequence in this area was similar between subunits, the

Figure 7.5: PCR analysis of splice$_1$ MO effects on the γ transcript sequence. A) Diagram indicating splice$_1$ γ MO binding location (red bar) on γ primary transcript. The four predicted mis-splice products are indicated (e, exons, i, introns). Arrows indicate reverse and forward primers used for PCR. B) PCR amplicons from splicing reactions. Each lane contains PCR products from one cDNA library created from a pool of 20 WT or 20 MO injected embryos. Brackets indicate bands removed for DNA sequencing and correspond to the indicated products diagrammed in A. C) Densitometry measurements for gel shown in B, where exposure was within linear range of photometer.

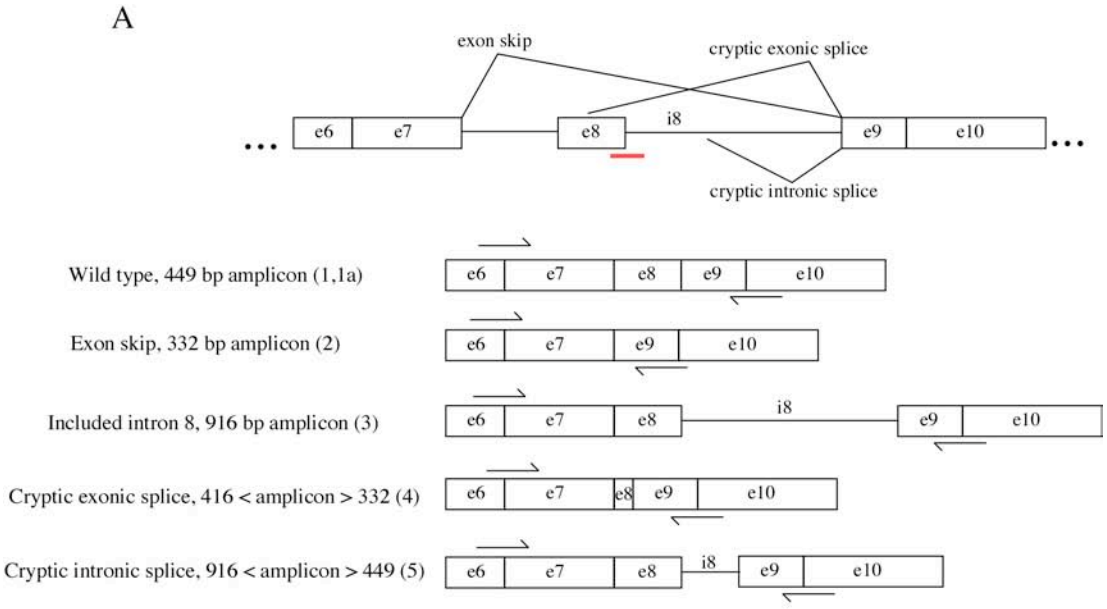
A
exon skip
cryptic exonic splice
e6
e7
e8
i8
e9
e10
cryptic intronic splice
Wild type, 449 bp amplicon (1,1a)
Exon skip, 332 bp amplicon (2)
Included intron 8, 916 bp amplicon (3)
Cryptic exonic splice, 416 < amplicon > 332 (4)
Cryptic intronic splice, 916 < amplicon > 449 (5)

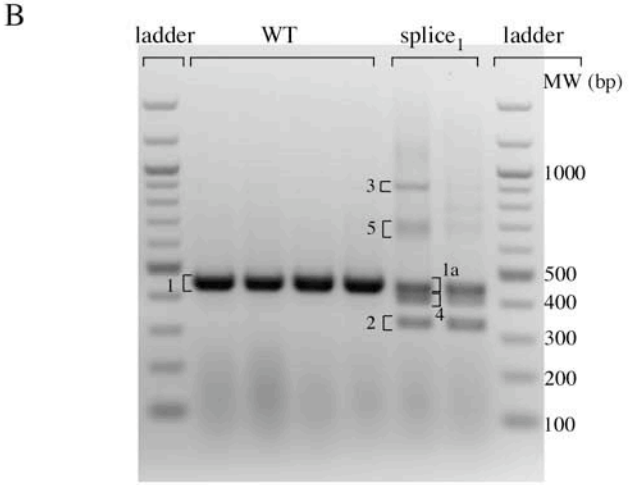
B
ladder
WT
splice1
ladder
MW (bp)
1000
500
400
300
200
100
1
3
5
1a
4
2

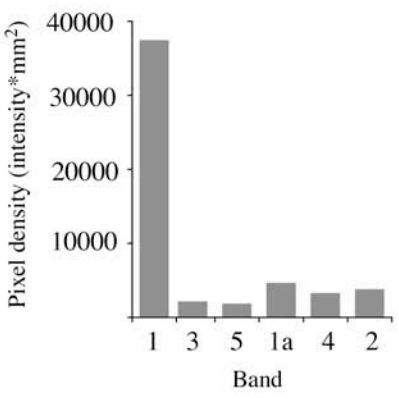
C
Pixel density (intensity*mm2)
40000
30000
20000
10000
1
3
5
1a
4
2
Band

splice$_1$ MO was likely to be specific for the γ subunit because the annealing site was formed primarily by intron sequence that was highly divergent between subunits. The location of the splice$_1$ site on the γ pre-mRNA, the location of the primers for PCR analysis, and the predicted sequence alterations of the γ sequence are all diagrammed in Figure 7.5A. RNA from two pools of embryos injected with splice$_1$ was independently tested by PCR with the primers locations indicated in Figure 7.5A. The resultant PCR products for both WT and splice$_1$ injected embryos are shown together in the agarose gel picture (Figure 7.5B). For WT embryos, PCR resulted in a single band of the predicted size of ~450 bp. For injections with splice$_1$ MO, PCR indicates products consistent in size with each of the predicted mis-splice options shown in Figure 7.5A. A WT band, and each of the bands from the splice$_1$ PCR were excised from the gel, and their identity was confirmed by DNA sequencing (Figure 7.5B). Densitometry was used to estimate the overall intensity of each band shown in the gel indicated that the band corresponding to WT γ transcript was greatly reduced by the splice$_1$ MO (Figure 7.5C). Pixel intensity was compared in an exposure where both bands intensities were within the linear range of the photometer (gel not shown) and was not performed on the over-exposed picture of the gel shown in Figure 7.5B that was taken for illustrative purposes. PCR results indicated that the second MO splice$_2$ had no effect on the γ transcript was not considered further.

Overall, the results from the γ MO injections were consistent with the previous results indicating that the αβδγ channel does not contribute to synaptic current decay kinetics in either muscle cell.

MO knockdown of the ε subunit in vivo

The ε subunit contribution to synaptic current properties was examined using a translational site MO. Fitting the synaptic currents in ε MO fish indicated that the majority of events (114 of 178) in the 17 fast muscle cells examined were well described by a single exponential over 10-90% of the decay. The remaining events, however, required fitting with two exponents to fully describe their decay. These events were present in 13 of 17 cells examined, and represented 36% of the total number of events (64 of 178). Therefore, the best fit was determined visually for each event, and the resultant average for each event type was determined separately for each cell (Figure 7.6A).

The average τ_{decay} for events fit with a single exponential corresponded to 1.7 ± 0.3 ms, and was ~2.5-fold more prolonged than WT fast muscle decays (Figure 7.6A, $p<0.0001$). Although greatly prolonged, the τ_{decay} values remained slightly faster than the τ_{decay} seen for WT slow muscle (1.7 vs. 2.4 ms, $p=0.003$). This finding is consistent with the hypothesis that the ε subunit is responsible for the fast decay kinetics in fast muscle.

The average τ_{decay} for each component of the events described by two exponentials corresponded to 0.52 ± 0.2 and 2.3 ± 0.5 ms (Figure 7.6A). The slow component generally accounted 64 ± 20% of the total decay amplitude, and the fast component accounted for the remaining 37 ± 20%. In cells where a large percentage of events (>60%) required two exponentials, the contribution of the slower component was generally less than the contribution by the fast (47% slow, 53% fast). In the cells that had a low percentage of fits to double exponents (<20%), the contribution of the slower component was generally much higher (>80%). This relationship is consistent with dose-dependent variability in the extent of ε subunit reduction between cells.

Figure 7.6: Fast and slow muscle synaptic current properties in embryos treated with ε subunit MO. A) Average synaptic current τ_{decay} values for each fast muscle cell (filled circles), when events were fit to a single (n=17 cells), and double exponential (n=13 cells) as indicated, and corresponding overall average ± SD (open circles), at -70 mV. WT values for both slow and fast muscle τ_{decay} at -70 mV are included for comparison. B) Average synaptic current amplitude for each fast muscle cell (filled circles), and overall average ± SD (open circles) at -70 mV. C) Average synaptic current τ_{decay} values for each slow muscle cell (filled circles), and overall average ± SD (open circles), at -70 mV. D) Average synaptic current amplitude for each slow muscle cell (filled circles), and overall average ± SD (open circles) at -70 mV.

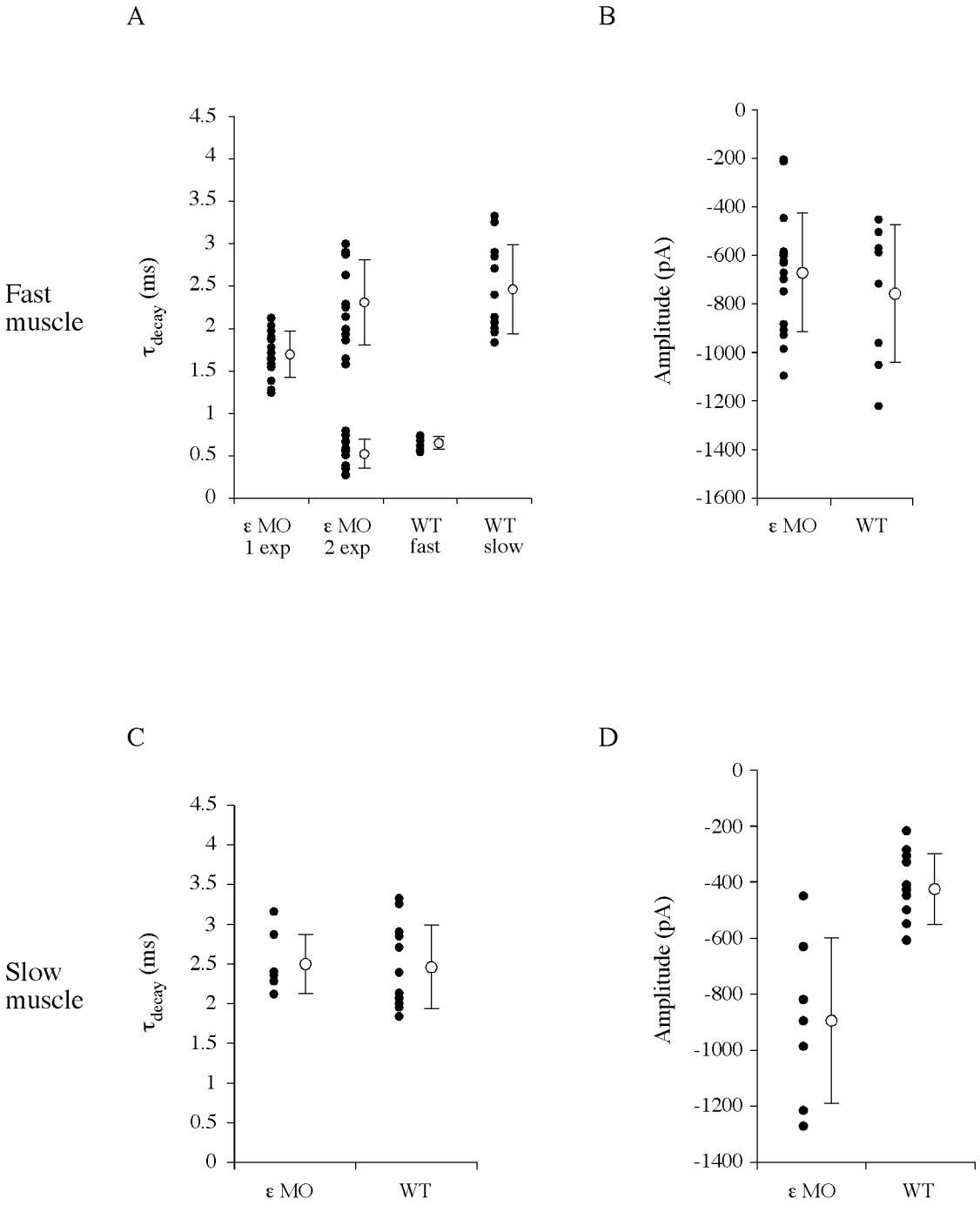
A
B
Fast muscle
τ_{decay} (ms)
4.5
4
3.5
3
2.5
2
1.5
1
0.5
0
ε MO 1 exp
ε MO 2 exp
WT fast
WT slow
Amplitude (pA)
0
-200
-400
-600
-800
-1000
-1200
-1400
-1600
ε MO
WT
C
D
Slow muscle
τ_{decay} (ms)
4.5
4
3.5
3
2.5
2
1.5
1
0.5
0
ε MO
WT
Amplitude (pA)
0
-200
-400
-600
-800
-1000
-1200
-1400
ε MO
WT

The brief component is similar in duration to the WT fast muscle synaptic decay and the slow component is similar to the WT slow muscle synaptic decay (p=0.2 and 0.7, respectively). These values are consistent with a partial reduction of ε subunit leaving a fast kinetic component. Regardless of the fitting required to describe the decay time-course, the average amplitude of the synaptic currents was not different from WT (Figure 7.6B), suggesting that the overall AChR receptor number was similar in fish with reduced ε subunit levels.

The synaptic current properties of ε MO slow muscle were also examined. Synaptic current τ_{decay} was similar to WT in the seven slow muscle cells examined (Figure 7.6C), consistent with the idea that ε is not included in the slow muscle AChR. Synaptic current amplitude, however, was larger in ε MO injected fish than WT (Figure 7.6D). The basis for this effect is not clear, but may represent an enhanced ability of the αβδ receptor to form in the absence of ε subunit.

Knockdown of both γ and ε subunits in vivo

Although the synaptic decay was significantly prolonged in fast muscle by reducing the amount of ε subunit, it remained possible that the slowly decaying currents of fast muscle were due to the αβδγ subunit, rather than the presumed slow muscle AChR, αβδ. Single-channel recordings had suggested that the αβδγ receptor type was present on fast muscle, although to a much lesser extent than the αβδε receptor. I therefore injected fish with MO targeting both γ and ε transcripts (ε ATG_1 + γ $splice_1$), to address whether the slow decay of fast muscle could be accounted for by receptors containing the γ subunit.

Figure 7.7: Fast and slow muscle synaptic current properties in embryos treated with ε and γ subunit MOs. A) Average synaptic current τ_{decay} values for each fast muscle cell events that fit to a single (n=9 cells), and double exponential (n=8 cells) as indicated, and corresponding overall average ± SD (open circles), at -70 mV. WT values for slow muscle τ_{decay} at -70 mV are included for comparison. B) Average synaptic current amplitude for each fast muscle cell (filled circles), and overall average ± SD (open circles) at -70 mV. C) Average synaptic current τ_{decay} values for each slow muscle cell (filled circles), and overall average ± SD (open circles), at -70 mV. D) Average synaptic current amplitude for each slow muscle cell (filled circles), and overall average ± SD (open circles) at -70 mV.

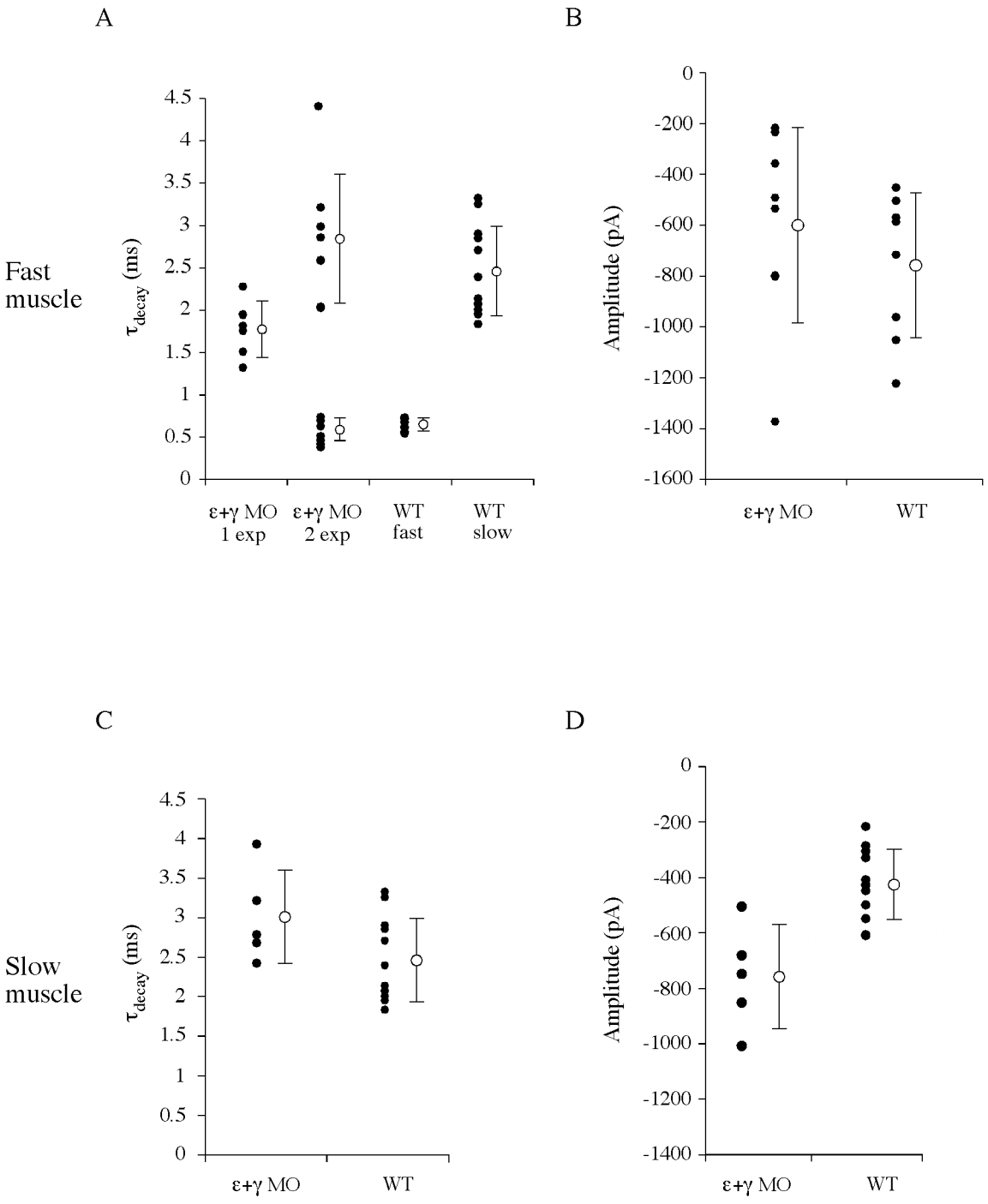
A
B
Fast muscle
τ_{decay} (ms)
Amplitude (pA)
ε+γ MO 1 exp
ε+γ MO 2 exp
WT fast
WT slow
ε+γ MO
WT
C
D
Slow muscle
τ_{decay} (ms)
Amplitude (pA)
ε+γ MO
WT

Overall, the synaptic current kinetics in fast muscle of embryos injected with both ε and γ MOs were similar to those of embryos injected with only the ε MO. The synaptic τ_{decay} was described by a single exponential decay for most events examined in eight cells (40 of 67), resulting in an average τ_{decay} of 1.8 ± 0.3 ms (Figure 7.7A). The remaining events were well described by two exponential components whose average values corresponded to 0.54 ± 0.1 ms, and 2.8 ± 0.8 ms. These two components of the double exponential fit were similar to those estimated in the ε MO fish, and likely correspond to partial reduction of the ε subunit. These results suggested that the γ MO did not alter the slow component of the current present in fast muscle when ε subunit was also reduced, consistent with the idea that αβδγ channel function could not account for slow synaptic current kinetics.

Slow muscle synaptic properties were also examined in the γ and ε double MO injected fish. In the five cells examined, the τ_{decay} was no different than that of WT (Figure 7.7C). However, as seen for the ε MO alone, the amplitude of synaptic currents was increased in MO fish (Figure 7.7D).

MO knockdown of the β1a subunit in vivo

My attempts to reconstitute receptors containing β1a suggested that these receptors did not form functional AChRs, but it was not possible to exclude the possibility that the β1a subunit was modified uniquely during expression in muscle cells, and that this modification did not occur in oocytes. The finding that the β1a subunit increased the expression of αβδ receptors in the presence of the γ subunit, however, raised the possibility that it played a role in maintaining the αβδ AChR type in slow

Figure 7.8: Fast and slow muscle synaptic current properties in embryos treated with β1a subunit MOs. A) Average synaptic current τ_{decay} values for each fast muscle cell (filled circles), and overall average ± SD (open circles), at -70 mV. B) Average synaptic current amplitude for each fast muscle cell (filled circles), and overall average ± SD (open circles) at -70 mV. C) Average synaptic current τ_{decay} values for each slow muscle cell (filled circles), and overall average ± SD (open circles), at -70 mV. D) Average synaptic current amplitude for each slow muscle cell (filled circles), and overall average ± SD (open circles) at -70 mV.

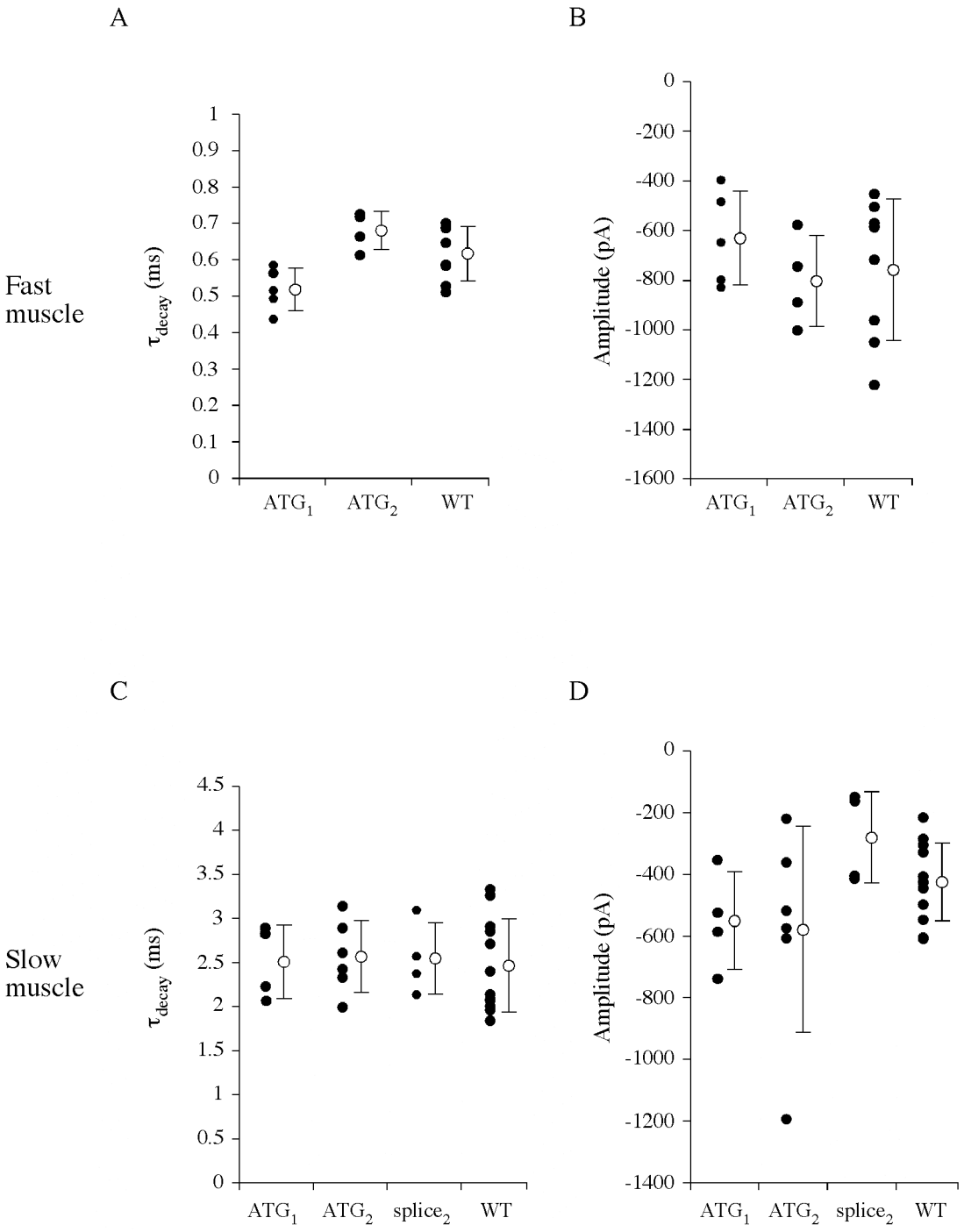
A
B
Fast muscle
τ_{decay} (ms)
Amplitude (pA)
ATG$_1$
ATG$_2$
WT
C
D
Slow muscle
splice$_2$

muscle, even in the presence of low amounts of γ or ε subunits. For these reasons, I tested MOs designed to decrease β1a expression, and examined the synaptic current properties.

The first MO tested against β1a was a translational site MO (ATG_1) designed to anneal to a sequence upstream of both the original β1a initiation codon identified in cloning, and the second initiation codon indicated in the database (Chapter 5). Overall, the kinetics and amplitude synaptic currents in both muscle types (n=5 fast, n=4 slow) were similar to those of WT fish (Figure 7.8A-D).

We had identified, however, a second form of the β1a subunit that indicated an alternative splice form may be expressed that used a different initiation codon. Although this second β1a sequence was also not functional in expression studies, I designed a translation site MO (ATG_2) to test its role *in vivo*. Like ATG_1, the synaptic current properties of fish injected with ATG_3 were similar to WT in both muscle types (n=4 fast, n=6 slow; Figure 7.8A-D, ATG_2).

In general, altered synaptic function among MO injected fish resulted in compromised swimming behavior (Table 7.1). A motility defect, therefore, was generally a good predictor of altered synaptic function, except when MOs resulted in severe morphological defects (Table 7.1, see γ ATG_1). Overall, fish injected with MOs targeting β1a were WT-like in their swimming behavior, consistent with the finding that their synaptic current properties were unaffected.

To verify the results of the translation site MOs, splice site MOs were also tested against β1a. For these experiments, three different splice MOs were designed to disrupt the protein domains that form the transmembrane regions M1 and M2, normally integral

Table 7.1: Summary of AChR subunit morpholino studies.

	Target	Sequence	Amount (ng)	Synaptic Physiology	Morphology	Motility
α	ATG	TTCATTTCTGTTG-ATATGACTGGA	8-12	Decrease in fast and slow muscle current amplitude.	Mild edema, slightly thinner tails.	Very weak shimmy movement.No spontaneous activity. Improved swimming over time .
β	ATG	GTTTCTTCATCAG-CTTATCTTCCAT	4-8	Decrease in fast and slow muscle current amplitude.	Tails shorten and curl, normal head and eyes.	Weak shimmy/buzz movement but rapid, tends to circle.
β_{1a}	ATG 1	CGTAGTTGATTTT-TAGCCACACCAT	12	No effect.	WT	WT
	ATG 2	CACCATGTTGGTG-TTACATAACATC	12	No effect.	WT	WT
	E7I7	TGTAATTAAAGAT-GTCCACCTGCAC	12	Untested	WT	WT
	I7E8	TCACCTGAGTGAA-AGGACAGAAAAC	4	No effect	Edema, bent tail or stubby tail. Normal head and tail thickness.	Rapid and vigorous swimming, but circles.
	E8I8	AATATTTGGTTGT-CGCACCTTGCGC	12	Untested	WT	WT
γ	ATG 1	CATGGTTGAAATC-CTGAGAGAAACA	1-1.5	No effect	Thin tail, brain necrosis, small head and eyes, overall deterioration by 5 dpf.	Weak but rapid shimmy on touch.
	ATG 2	TGTTGAAGGCTCT-CCAGTACCTAGT	8	No effect	Slightly thinner tail.	WT
	I6E7	ATTCTCCATTCTC-TGACCAATCAGA	12	Untested	Thin tail and curled.	WT
	E8I8	TAATTAAGGCACA-TACTCACTTCCC	12	No effect	WT	WT
ε	ATG	TGCCGAATCTCTC-GGCCACGGCCAT	6-10	Increase in fast τ_{decay}. Increase in slow muscle current amplitude	Relatively normal, thinner tails and edema later. Progressive deterioration of tail fast muscle.	Early over-contraction, (24) then weak shimmy/immobile (48-96) with eventual complete paralysis.
	I6E7	GTTTTCTGTGAGA-CCATGTGATTAA	12	Untested	Slight tail kink.	WT

to AChR function. That the transmembrane domains are necessary for β1a subunit function, however is suggested only by comparison to typical AChR function. Injection of $splice_1$ and $splice_3$ resulted in fish that demonstrated WT-like behavior and morphology, and so synaptic currents were not examined. Fish injected with $splice_2$, however, exhibited a mild motility phenotype, so recordings were performed on both types of muscle. Synaptic current properties in $splice_2$ injected fish were similar to those of WT fish (Figure 7.8, $splice_2$). Together, these results suggested that β1a did not play a role in determining synaptic kinetics in fast or slow muscle. However, PCR analysis was not performed on splice injected MOs, so the efficacy of these MOs remains unverified.

Summary of AChR subunit knockdown experiments

Table 7.1 summarizes the results for the synaptic physiology for each MO tested, and provides a brief description of the resultant morphological and swimming characteristics (motility) of each MO tested. The effect of the translational site MO against the β subunit was redundant with those of α, and thus a brief description of those results was included.

Summary of results Chapter 3 through Chapter 7

The findings presented in Chapter 7 are shown in Table 7.2 for comparison to both the synaptic and single-channel characteristics determined in previous chapters.

Table 7.2: Summary of results from Chapters 3 through 7.

Source	Type	Representation (total events or amplitude)	Conductance	Kinetics (τ_{decay} or burst duration)	Voltage-dependence	
					Burst duration	Conductance
muscle synaptic events	fast	100%	-	brief (~0.5 ms)	-	-
	slow	80-100%	-	long (~3 ms)	-	-
muscle single channels	fast	90-100%	68 ± 4 pS	brief (~0.5 ms)	exponential	linear
	slow	80-100%	66 ± 2 pS	long (~3.5 ms)	atypical	inwardly rectifying
muscle single channels secondary class	fast	0-12%	51 ± 3 pS	intermediate (~1.2 ms)	-	-
	slow	0-23%	70 ± 4 pS	brief (~0.5 ms)	-	linear
reconstituted single channels	αβδε	100%	66 ± 2 pS	brief (~ 0.5 ms)	exponential	linear
	αβδγ	95%	51 ± 2 pS	intermediate (~1.3 ms)	exponential	linear
	αβδ	100%	70 ± 5 pS	long (~4.5 ms)	atypical	inwardly rectifying
MO muscle synaptic events ε	fast	50-100%	-	long (~3 ms)	-	-
	slow	-	-	unchanged	-	-
γ	fast	-	-	unchanged	-	-
	slow	-	-	unchnaged	-	-

CHAPTER 8

Discussion

Central premise

My studies were undertaken to identify the basis for the prolonged synaptic decay unique to vertebrate slow skeletal muscle, a feature that has remained unexplained since its first discovery about 50 years ago. Although best described in amphibian muscle (Fedorov et al, 1982; Uchitel and Miledi, 1987), similar observations have been shown for snake muscle (Dionne and Parsons, 1978), fish muscle (Luna and Brehm, 2006) and, where present, mammalian slow muscle (Chiarandini Stefani, 1979; Fedorov, 1987). Slow muscle in fish also conforms to the established pattern of vertebrate slow muscle in its inability to produce action potentials and its ability to maintain contraction in response to prolonged stimulation (Takeuchi, 1959, Hidaka and Toida, 1969, Yamamoto, 1972). In non-physiological conditions, such as denervation, action potentials can be induced in slow muscle cells of fish (Korenaga et al, 1982), frog (Miledi et al, 1971), and mammals (Bondi et al, 1986). Normally, however, cholinergic synaptic transmission, rather than propagated action currents, provides the depolarization needed for slow muscle contraction. Slowly decaying synaptic currents in tonic muscle may depolarize muscle cells to a greater extent than rapidly decaying currents, and therefore may be more efficient in generating slow muscle contraction (Ruff and Spiegel, 1990). In accordance

with this idea, slow muscle fibers generally have a higher input resistance and longer time-constant than their twitch counterparts (Kuffler and Vaughn Williams, 1953a,b), and are well suited for distributing synaptic depolarization throughout the cell membrane. Although the input resistance between muscle fibers is not different at the developmental stage studied here (Buss and Drapeau, 2000), fast muscle fibers in embryonic zebrafish generate action potentials in response to depolarizing current pulses while slow muscle cells do not (Buckingham and Ali, 2001). In adult fish, slow muscle is used during low-intensity movements, such as those of slow swimming, where its position within the body provides maximal efficiency for this purpose and suggests that muscle adaptation plays an important role in energy conservation (Rome et al, 1988).

Neurotransmitter diffusion hypothesis

Two proposals have been put forth to explain the prolonged decay of synaptic currents in slow muscle 1) low levels of acetylcholinesterase (AChE) activity in slow muscle and 2) differences in channel kinetics of acetylcholine receptor (AChR). The proposal that differences in AChE activity explain the different synaptic currents in fast and slow muscle has been formed primarily on the basis of differences in cholinesterase stain in the different muscle types (see Ogata 1988 for review). Briefly, the Karnovsky or silver staining techniques among vertebrate muscles has generally indicated that AChE stains strongly at fast endplates and weakly at slow endplates. The AChE enzyme is present in 72 hpf zebrafish (Downes and Granato, 2004; Ibanez-Tallon et al, 2004) but staining between fast and slow muscle have not been compared.

The role of cholinesterase at mature tonic and twitch types of frog muscle has been examined previously by acute pharmacological inhibition of the enzymatic activity. Federov and colleagues found that the synaptic current decay of both muscle types was affected by AChE inhibition, albeit to different extents (Federov et al, 1982). Specifically, they showed a 1.7-fold and 1.2-fold slowing in decay kinetics, in fast and slow muscle respectively. The authors concluded that the slow muscle decay did not likely reflect the slower clearance of ACh from the cleft, because fast muscle decay times remained significantly faster than slow muscle even in the absence of active clearance. The same conclusion was drawn by another study (Uchitel and Miledi, 1987) that used cold temperatures to reduce AChE activity. In both of these studies, the mechanism of slow muscle synaptic decay was proposed to reside with receptor kinetics.

Using an AChE null mutant line of zebrafish, I directly tested the hypothesis that AChE could account for the difference in kinetics between the two muscle types. This was the first opportunity to examine the role of AChE in any null animal model, and allowed me to avoid the potential complications of species-dependent differences in pharmacological inhibition of AChE (Kullberg et al, 1980). While genetic null AChE animal models are available in both mice and in zebrafish, there is more than one esterase enzyme in mice at the neuromuscular junction. Activity of the enzyme butyrylcholinesterase is sufficient for normal transmission in $AChE^{-/-}$ mice, confounding study of the loss of active clearance in this preparation (Xie et al, 2000). Zebrafish, however, do not have a homolog of the butyrylcholinesterase gene (Downes and Granato, 2004), and thus present an excellent system in which to study the role of AChE.

My findings indicated that fast and slow τ_{decay} values were slowed by 1.7 and 1.1-fold, respectively, similar to that found by Federov et al. Moreover, fast muscle synaptic decay was not slowed to the extent of slow muscle simply by removing clearance mechanisms. Thus, my studies do not support the proposal that differences in decay rate are governed by differences in AChE activity.

Receptor burst duration hypothesis

An alternative proposal for differences in synaptic current kinetics involved AChRs with different burst durations. Precedent for channels with two different burst durations came from developmental studies on fast twitch muscle. Fast muscle in rat undergoes a developmental reduction of synaptic current τ_{decay} shortly after birth (Sakmann and Brenner, 1978, Fischbach and Scheutze, 1980). This change in τ_{decay} was shown to represent a switch in the subunit composition of the AChRs from the γ-containing embryonic form to the ε-containing adult form (Mishina et al, 1986). Interestingly, the resultant 3-fold reduction in τ_{decay} following incorporation of the adult receptor form is similar to the overall difference in τ_{decay} between slow and fast muscle in zebrafish. Based on this correlation, it was possible that expression of the embryonic receptor type of fast muscle might account for the τ_{decay} of slow muscle. In accordance with this notion, immunohistological studies of protein expression in vertebrate slow muscle indicate that adult extraocular muscles remain immunoreactive for embryonic forms of synaptic and contractile proteins, including the γ subunit of the AChR (Khanna et al, 2003; Kaminski, 2006). The embryonic AChR hypothesis is of particular interest in light of the selective deterioration of slow muscle in myasthenia syndromes, and its

selective sparing in dystrophic syndromes and ALS. Thus, the "embryonic" phenotype of extraocular muscle is considered an appealing causal mechanism for these disease state differences (Khanna et al, 2003).

To date, two studies have sought to examine the hypothesis that slow muscle expresses a unique AChR with distinct kinetic properties. In frog interhyoideus muscle, it was shown that the miniature event decay had a similar 3-fold difference seen for other frog slow muscle types. Recordings of single-channel events from each type indicated that fast muscle only had brief open duration receptors, while slow muscle had both long and short open duration receptors (Hendersen and Brehm, 1989). Based on the single-channel properties, the long duration receptor was proposed to be most similar to the reconstituted αβδγ isoform. Analogous studies in snake costocutaneous muscle also indicated the presence of two receptor types in slow muscle. The identity of the slow receptor from snake muscle was not easily attributable to the αβδγ isoform, as reconstitution experiments were not performed for snake subunits (Dionne, 1989). One report in zebrafish also indicated the presence of two distinct channel types on embryonic muscle, but neither had a long open duration (Nguyen et al, 1999). Thus, it was not clear whether different receptor types could account for the different muscle synaptic kinetics in fish.

Receptor burst duration hypothesis in zebrafish

To determine if each muscle expressed a unique channel type in zebrafish, I recorded on-cell single channel currents from both fast and slow muscle cells *in situ*. Recordings from slow muscle cells identified one class of single channel events, with an

average burst duration that matched well to the decay time of the synaptic current. These long duration events were confined to slow muscle cells strongly suggesting that receptor kinetics were the mechanism underlying prolonged synaptic current decay. They were likely missed in the previous single-channel recordings from dissociated muscle cells due to the predominance of fast muscle cells (Nguyen et al, 1999). Although my recordings are likely all extrasynaptic, noise analysis and single-channel studies on Xenopus and mouse skeletal muscle indicate there is no distinction between extrasynaptic and synaptic AChR isoforms (Kullberg et al, 1981; Brehm and Kullberg, 1987; Hendersen et al, 1987).

Recordings from fast muscle indicated that the burst duration of fast muscle receptors was very brief, corresponding well to the τ_{decay} of synaptic events in that muscle type. Overall, the single-channel evidence from slow and fast muscle lent support to the hypothesis that differences in receptor burst duration were responsible for muscle decay kinetics. However, the mechanism causal to these differences in burst duration remained a mystery.

The AChR in fast muscle AChR is αβδε

To determine the molecular equivalents of the native AChRs found on muscle, I reconstituted known zebrafish receptor types in Xenopus oocytes and studied their single-channel characteristics. Of all combinations tested, only the zebrafish subunit combinations αβδ, αβδγ and αβδε receptors expressed well. The reconstituted subunit combination αβδε matched well to the slope conductance, average burst duration and voltage-dependence of the burst duration of the fast muscle primary AChR class. This finding was not surprising, considering that the αβδε isoform has been identified as the

mature fast muscle AChR in mammals (Mishina et al, 1986) and amphibians (Sullivan et al, 1999). However, the zebrafish $\alpha_2\beta\delta\varepsilon$ isoform stands out among vertebrate receptors as having the briefest average burst duration ever recorded. The rapid synaptic kinetics seen in fish have been proposed to result from differences in membrane fluid dynamics specific to the lipid composition of fish membrane (Macdonald and Balnave, 1984; Cox and Macdonald, 2001). However, my findings from single-channel recordings provide a simple explanation wherein the receptor kinetics account for the brevity of synaptic current decay.

Reconstitution of the $\alpha\beta\delta\gamma$ subunit combination resulted in single-channel characteristics very similar to those of the secondary type of AChR in fast muscle. The $\alpha\beta\delta\varepsilon$ and $\alpha\beta\delta\gamma$ isoforms bore a conductance ratio of 1.4-fold, representing a signature characteristic preserved between these isoforms in other vertebrates (Mishina et al, 1986, Sullivan et al, 1999). The primary and secondary AChR classes in muscle also had this characteristic 1.4-fold conductance ratio similar to that seen in previous single-channel studies of fast muscle (Hamill and Sakmann, 1981; Auerbach and Sachs, 1984; Brehm et al, 1984a; Siegelbaum et al, 1984; Owens and Kullberg, 1989a,b). The mean burst duration of the reconstituted $\alpha\beta\delta\gamma$ receptor was approximately two-fold longer than the $\alpha\beta\delta\varepsilon$ receptor, and also corresponded well to the burst duration of the secondary AChR class on fast muscle. The difference in burst duration between the $\alpha\beta\delta\varepsilon$ and $\alpha\beta\delta\gamma$ zebrafish isoforms was less than that measured for other vertebrate receptors, perhaps reflecting the fact that rapid synaptic decay is important for zebrafish fast muscle function even in early development. The relatively small contribution of the $\alpha\beta\delta\gamma$ receptor in the native muscle suggested that by the age studied, 3 days post-fertilization,

most of the receptors have already been replaced by the αβδε type. The overlap of expression of αβδε and αβδγ isoforms reported here is similar to that observed in developing Xenopus tadpole muscle (Kullberg et al, 1981; Owens and Kullberg, 1989a,b). Even as early as 24 hpf, tadpole muscle expresses αβδε receptors, but the ratio of receptor types changes over time so that only α_2βδε is represented (Owens and Kullberg, 1989a,b). Comparatively, the adult receptor in mammalian twitch muscle does not appear at the synapse until several weeks after fertilization, and the αβδγ receptor type is thought to be responsible for proper neuromuscular junction development (Takahashi et al, 2002; Koenan et al, 2005). Although important in early development, the αβδγ receptor is unable to substitute for the αβδε form in mice lacking the ε subunit (Missias et al, 1997). Establishment of the role of γ subunit in synapse formation has only been characterized in mice, and a similar examination in non-mammalian vertebrate muscle is lacking.

The AChR in slow muscle lacks γ and ε

The only heterologously expressed subunit combination to show significant ACh activated current other than αβδγ and αβδε was αβδ. In oocytes, the αβδ combination resulted in currents that were equivalent in amplitude to the traditional combinations. Exclusion of either α or β subunit RNA did not result in ACh-responsive current, indicating that the minimal combination represented a receptor composed of αβδ. Previous studies of αβδ have indicated that, like traditional isoforms, this receptor was formed of five subunits in the stoichiometry of $\alpha_2\beta\delta_2$ (Sine and Claudio, 1991). Thus, I

will refer to this receptor type as $\alpha_2\beta\delta_2$ in the traditional format used for $\alpha_2\beta\delta\varepsilon$ and $\alpha_2\beta\delta\gamma$.

Evidence that the $\alpha_2\beta\delta_2$ receptor is responsible for synaptic transmission in slow muscle derived from much experimental evidence, both molecular and physiological. First, the $\alpha_2\beta\delta_2$ receptor was the only isoform that had a long burst duration similar to that of the slow muscle AChR. Comparatively, the slow muscle AChR burst duration was six-fold longer than $\alpha_2\beta\delta\varepsilon$, and three-fold longer than $\alpha_2\beta\delta\gamma$. Additionally, both the $\alpha_2\beta\delta_2$ receptor and the slow muscle AChR were the only two channel types for which the burst duration showed virtually no dependence on membrane voltage. This agreement provided strong support for the idea that the $\alpha_2\beta\delta_2$ receptor was the principal isoform on slow muscle.

The second line of evidence that the $\alpha_2\beta\delta_2$ receptor represented the slow muscle AChR came from measurements of single-channel conductance. The slow muscle AChR had slightly smaller conductance than $\alpha_2\beta\delta_2$ receptor, but still considerably larger than the $\alpha_2\beta\delta\gamma$ isoform. Initially, I was very concerned about this small but significant difference because single-channel conductance is a key channel characteristic that is typically shared between reconstituted and native receptors. Resolution of this problem led to what may have been the most compelling evidence supporting the role of $\alpha_2\beta\delta_2$ receptor as the slow muscle AChR.

The somewhat non-linear IV relations for slow muscle AChRs suggested that the range over which the conductance was measured could generate different values, potentially contributing to this mismatch. Similarly, the synaptic currents in slow muscle displayed a similar voltage-dependent decrease in conductance, in agreement with the

single-channel properties. Finally, the single-channel currents from slow muscle could not be outwardly directed at very negative applied potentials. Non-linear current-voltage relations for synaptic current and single-channel AChR currents were not observed for fast muscle. The definitive experiment came from measurements of macroscopic ACh-activated currents in Xenopus oocytes. These results indicated that currents associated with either $\alpha_2\beta\delta\gamma$ or $\alpha_2\beta\delta\varepsilon$ were reasonably linear over a large range of potentials, but that $\alpha_2\beta\delta_2$ currents showed pronounced rectification at positive potentials. Armed with this understanding, I determined that the single-channel conductance of $\alpha_2\beta\delta_2$ receptor and the slow muscle AChR were actually very similar at the most negative potentials where rectification was expected to be minimal. Initially, it seemed confusing that the $\alpha_2\beta\delta_2$ receptor did not show inward rectification in single-channel currents recordings from outside-out patches. However, extrinsic regulation of channel function by endogenous intracellular channel blockers is common among nicotinic AChRs, and accounts for the inward rectification of neuronal subtypes (Haghighi and Cooper, 1998).

The final line of evidence that the $\alpha_2\beta\delta_2$ isoform accounted for slow muscle synaptic currents was provided by the morpholino knockdown of AChR receptor subunits. Knockdown of the ε subunit was the critical test of this hypothesis, as my data suggested this subunit was responsible for the functional distinctions between fast and slow muscle AChRs. Consistent with this idea, the ε morpholino significantly prolonged synaptic current decay in fast muscle but had no effect in slow muscle. The synaptic currents from fast muscle of ε morpholino treated fish were often bi-exponential and the two decay time constants corresponded to the burst duration of the $\alpha_2\beta\delta_2$ receptor, and the $\alpha_2\beta\delta\varepsilon$ receptor, as though the knockdown of ε was incomplete. Partial knockdown is

likely to be the case as my experiments with the α subunit morpholino indicated that the current amplitudes were reduced but not eliminated. Of all the morpholinos tested, the synaptic current decay was only altered by the ε morpholino, and this effect was restricted to fast muscle. Knockdown of the γ subunit had no effect on either muscle type, although the morpholino was independently shown to significantly reduce γ transcript levels. These findings provided strong support for my assertion that the $\alpha_2\beta\delta\varepsilon$ receptor governed synaptic currents in fast muscle, and that the $\alpha_2\beta\delta_2$ receptor governed synaptic currents in slow muscle.

Drawing this conclusion was complicated by the question of whether the $\alpha_2\beta\delta_2$ channel would still form in slow muscle in the presence of the ε and γ subunits. PCR measurements of subunit RNA indicated the presence of both γ and ε subunits in both types of muscle cells. However, the variability was large between experiments, and to ensure enough material for PCR it was necessary to pool multiple cells, raising the likelihood of cross contamination during the collection process. The qPCR analysis supported the idea that the ε subunit was necessary in fast muscle as it was the most abundant subunit transcript. In contrast, a very low level of ε transcript was detected in slow muscle, consistent with the extremely low levels of $\alpha_2\beta\delta\varepsilon$ receptor expression as evidenced by both single-channel and synaptic current analysis. Although the γ transcript was relatively abundant in slow muscle, I found no evidence indicating that the $\alpha_2\beta\delta\gamma$ receptor was expressed, leaving me to question how this might occur.

A plausible mechanism by which $\alpha_2\beta\delta_2$ receptor expression may be promoted in the presence of other subunits, and in particular the γ subunit, was identified in my experiments with reconstituted receptors in oocytes. When the $\alpha\beta\delta\gamma$ subunit combination

was injected in oocytes, I observed a small but consistent representation of single-channel events characteristic of $\alpha_2\beta\delta_2$. This observation became particularly relevant during my efforts to determine the function of the β1a subunit, where I co-expressed both β subunit types along with α, δ and γ. Inclusion of β1a subunit RNA significantly increased the relative expression of the $\alpha_2\beta\delta_2$ isoform. These results were totally unexpected. The PCR measurements indicated a 40-fold enrichment of β1a RNA in slow muscle compared to fast muscle. Comparison of the β subunits between muscle types indicated that β transcript was enriched 11-fold compared to β1a transcript in fast muscle, whereas β1a was only two-fold more abundant than β in slow muscle. When I adjusted the ratio of β1a to β RNA in oocytes to reflect the large difference between muscle types, I observed an even greater relative expression of $\alpha_2\beta\delta_2$ receptor. I did not repeat the experiments using the ε subunit. Altering the ε and γ subunit RNA levels to reflect native muscle would be a useful future direction to examine this role of β1a.

These results raised the possibility that the β1a subunit may play a non-traditional role in AChR formation, by helping to direct the formation of other receptor isoforms. For example, β1a could act in a dominant negative manner in that the formation of $\alpha_2\beta1a\delta\varepsilon$ or $\alpha_2\beta1a\delta\gamma$ receptors might be incapable of function or insertion into the plasma membrane. Recent studies of the $GABA_A$ receptor have shown that a single amino acid mutation in the α1 subunit renders it non-functional, but capable of altering the molecular composition of the surface $GABA_A$ receptors in a dominant negative manner. The shift in subunit composition resulted in an altered time course of the GABA mediated synaptic currents in cortical neurons (Ding et al, 2010). In support of this idea, studies in the Ono lab indicated that a β1a-GFP fusion protein expressed transiently in zebrafish muscle was

unable to cluster at the membrane, although GFP was present throughout the cytoplasm. In contrast, the highly related β-GFP fusion protein translocated to the synapse and was co-localized with a presynaptic marker. In both cases, GFP expression was detected in fast muscle, and further experimentation is needed to test if this holds true in slow muscle (Dr. Fumihito Ono, personal communication). In conflict with this hypothetical role for β1a, however, were my results that morpholinos against β1a did not alter the kinetics of slow muscle current decay. Because the efficacy of these morpholinos remains untested, these results are inconclusive.

Expression studies of the $\alpha_2\beta\delta_2$ receptor in other systems

The initial cloning of the skeletal muscle AChR subunits was followed by expression studies to determine the unique characteristics of different functional isoforms. Along with the traditional $\alpha_2\beta\delta\varepsilon$ and $\alpha_2\beta\delta\gamma$ isoforms, two other functional ACh receptor subunit combinations were identified. In studies of mammalian subunits, the first combination identified was $\alpha_2\beta\gamma_2$ (δ-less) which corresponded to an inwardly rectifying receptor with a conductance that was considerably smaller than either $\alpha\beta\delta\varepsilon$ or $\alpha\beta\delta\gamma$ (Kullberg et al, 1990). The $\alpha\beta\gamma$ receptor combination, however, has only been shown to be functional in mouse subunit reconstitution experiments.

The second nontraditional combination shown to be functional was the $\alpha_2\beta\delta_2$ receptor (ε/γ-less) reported here. This receptor has functioned in every vertebrate subunit reconstitution tested. The first functional characterization of the $\alpha_2\beta\delta_2$ receptor composed of bovine subunits indicated the channels bore unique properties, some reminiscent of the zebrafish $\alpha_2\beta\delta_2$ receptor (Jackson et al, 1990). The bovine $\alpha_2\beta\delta_2$

combination opened spontaneously in the absence of ACh, yielding an excess of brief burst duration events. These brief events persisted until high levels of ACh were used (~2 μM), and are similar to the brief duration openings also seen for the zebrafish $\alpha_2\beta\delta_2$ receptor. Although high concentration data was not used for kinetic analysis due to the possibility of open-channel block, it is worth noting that the short duration openings of the zebrafish $\alpha_2\beta\delta_2$ receptor were likewise eliminated in recordings in high ACh. As with zebrafish, the bovine $\alpha_2\beta\delta_2$ receptor isoform was expressed despite the presence of γ subunit RNA. Furthermore, the single-channel studies indicated that the bovine $\alpha_2\beta\delta_2$ receptor channel had a very long burst time and a large conductance that was sensitive to calcium concentration.

Subsequent studies on the murine $\alpha_2\beta\delta_2$ receptor indicated it also formed readily in reconstitution, even in presence of the ε subunit (Charnet et al, 1992). At the single-channel level the $\alpha_2\beta\delta_2$ receptor was difficult to distinguish from the $\alpha_2\beta\delta\gamma$ receptor, in terms of conductance and long burst duration (Charnet et al, 1992; Liu and Brehm, 1993). Studies using Xenopus laevis subunits also indicated that the $\alpha_2\beta\delta_2$ receptor expresses well, but the single-channel properties remain undetermined (Paradiso and Brehm, 1998). Studies of the torpedo $\alpha_2\beta\delta_2$ receptors indicate that they express to a lesser extent compared to the traditional isoforms. Similar to zebrafish, the single channel conductance of the torpedo $\alpha_2\beta\delta_2$ receptor resembles the $\alpha\beta\delta\varepsilon$ receptors; however, the burst duration of torpedo $\alpha_2\beta\delta_2$ is also brief, setting it apart from zebrafish (Golino and Hamill, 1992).

Although readily formed in reconstitution, the function of a nontraditional subunit isoform has never been identified in a physiological context. This is the first study that

has assigned a physiological role of a γ/ε-less receptor to skeletal muscle synaptic function. AChRs composed of minimal subunit combinations (ie. α or αβ) form the basis of all neuronal nicotinic AChR isoforms. Comparable studies in skeletal muscle have not been published.

Properties of the αβδ receptor relating to slow muscle function in zebrafish

The muscle AChR isoforms $\alpha_2\beta\delta\varepsilon$ and $\alpha_2\beta\delta\gamma$ have linear current-voltage relations, and inward rectification is a property normally reserved for neuronal AChR isoforms. Inward rectification in neuronal nicotinic receptors is due to block by endogenous polyamines (Haghighi and Cooper, 1998) and represents a regulatory mechanism common to both nicotinic, and glutamatergic receptor channel function (Bowie and Mayer, 1995). Inward rectification is invariably linked to increased calcium permeability among both nicotinic and glutamatergic receptor types, and mutational studies indicate that both properties are conferred by specific charged residues (Hume et al, 1991; Haghighi and Cooper, 2000,). Although the calcium permeability of the $\alpha_2\beta\delta_2$ receptor was not determined, the charged residue associated with neuronal nicotinic receptor rectification and calcium permeation is conserved in the δ subunits, but not in γ or ε (Haghighi and Cooper, 2000). If more permeable to calcium, the $\alpha_2\beta\delta_2$ receptor may represent another means by which slow muscle obtains calcium needed for contraction. Although frog fast and slow muscle types are both able to initiate contraction in the absence of extracellular calcium (Gilly and Hui, 1980), prolonged contraction in slow muscle required external calcium (Huerta et al, 1986). The extent to which zebrafish slow muscle contraction depends on extracellular sources of calcium is not known. Thus,

the unique properties of the $\alpha_2\beta\delta_2$ may represent a dual role specific to the function of slow muscle; first to provide prolonged currents that promote membrane depolarization and secondly, to direct calcium entry supporting contraction.

Chapter 9

Summary and Conclusions

1. Neuromuscular synaptic currents of larval zebrafish slow muscle cells decay along a time course that was 5-fold slower than fast muscle, reflecting a difference common to other vertebrate species.
2. Measurements of synaptic currents in an acetylcholinesterase null line of zebrafish indicated that the prolonged current time course of slow muscle could not be attributed to differences in transmitter clearance rate. Fast muscle synaptic decay remained 3-fold briefer than slow muscle current decay in the absence of active neurotransmitter clearance.
3. On-cell single-channel recordings of ACh-activated channels from both muscle types indicated that a 5-fold difference in the average burst duration fully accounted for the difference in synaptic current decay.
4. The single-channel kinetics, conductance, and voltage-dependence of the burst time of reconstituted zebrafish AChR subunits indicated that the $\alpha_2\beta\delta\varepsilon$ isoform likely accounted for the fast muscle AChR channel. The $\alpha_2\beta\delta\gamma$ receptor isoform likely accounted for an infrequently observed secondary class of events seen exclusively in fast muscle cells.

5. The single-channel kinetics and voltage-dependence of the burst duration indicated that $\alpha_2\beta\delta_2$ channel likely accounted for the slow muscle AChR channel. Additionally, both channels were the only to exhibit inwardly rectifying current-voltage relations, a characteristic only otherwise reported for neuronal AChRs. Study of the reconstituted $\alpha_2\beta\delta_2$ receptor indicated rectification was not an intrinsic channel property, but likely depended on extrinsic factors similar to that of neuronal AChRs.
6. Reduction of ε subunit by RNA knockdown *in vivo* was sufficient to prolong the decay of fast muscle currents to those of slow muscle, without reducing the current amplitude. Reduction of the γ subunit resulted in WT-like synaptic current properties of both muscle types. These results supported the hypothesis that the $\alpha_2\beta\delta_2$ receptor was sufficient to account for slow muscle current kinetics, while the $\alpha_2\beta\delta\varepsilon$ receptor was necessary for fast muscle current kinetics.
7. Evaluation of transcript levels in fast and slow muscle indicated all receptor subunits are present in each muscle type. A possible mechanism for expression of $\alpha_2\beta\delta_2$ receptors in the presence of γ and ε subunits was suggested by the role of the non-functional β1a subunit in promoting $\alpha_2\beta\delta_2$ expression.
8. The unique functional characteristics of the $\alpha_2\beta\delta_2$ receptor may play a dual role in slow muscle function through its ability to generate prolonged currents and possibly to increase calcium entry in response to neuronal activity.

REFERENCES

Anderson CR and Stevens CF. 1973. Voltage clamp analysis of acetylcholine produced end-plate current fluctuations at frog neuromuscular junction. Journal of Physiology 235:655-91.

Auerbach A and Lingle CJ. 1986. Heterogeneous kinetic properties of acetylcholine receptor channels in Xenopus myocytes. Journal of Physiology 378:119-40.

Auerbach A and Sachs F. 1984. Single-channel currents from acetylcholine receptors in embryonic chick muscle. Kinetic and conductance properties of gaps within bursts. Biophysical Journal 45(1):187-98.

Bertrand C, Chatonnet A, Takke C, Yan Y, Postlethwait J, Toutant JP and Cousin X. 2001. Zebrafish acetylcholinesterase is encoded by a single gene localized on linkage group 7. Journal of Biological Chemistry 276 (1): 464-74.

Bondi AY, Chiarandini DJ and Jacoby J. 1986. Induction of action potentials by denervation of tonic fibres in rat extraocular muscles. Journal of Physiology 374:165-78.

Bowie D and Mayer ML. 1995. Inward rectification of both AMPA and kainate subtype glutamate receptors generated by polyamine-mediated ion channel block. Neuron 15(2):453-62.

Brehm P, Kidokoro Y and Moody-Corbett F. 1984a. Acetylcholine receptor channel properties during development of Xenopus muscle cells in culture. Journal of Physiology 357:203-17.

Brehm P and Kullberg R. 1987. Acetylcholine receptor channels on adult mouse skeletal muscle are functionally identical in synaptic and nonsynaptic membrane. Proceedings of the National Academy of Sciences of the United States of America 84(8):2550-4.

Brehm P, Kullberg R and Moody-Corbett F. 1984b. Properties of non-junctional acetylcholine receptor channels on innervated muscle of Xenopus laevis. Journal of Physiology 350:631-48.

Brehm P, Steinbach JH and Kidokoro Y. 1982. Channel open time of acetylcholine receptors on Xenopus muscle cells in dissociated cell culture. Developmental Biology 91(1):93-102.

Buckingham SD and Ali DW. 2004. Sodium and potassium currents of larval zebrafish muscle fibres. Journal of Experimental Biology 207(Pt 5):841-52.

Buss RR and Drapeau P. 2000. Physiological properties of zebrafish embryonic red and white muscle fibers during early development. Journal of Neurophysiology 84(3):1545-57.

Charnet P, Labarca C and Lester HA. 1992. Structure of the gamma-less nicotinic acetylcholine receptor: learning from omission. Molecular Pharmacology 41(4):708-17.

Chiarandini DJ and Stefani E. 1979. Electrophysiological identification of two types of fibres in rat extraocular muscles. Journal of Physiology 290(2):453-65.

Colquhoun D and Sakmann B. 1981. Fluctuations in the microsecond time range of the current through single acetylcholine receptor ion channels. Nature 294:464-6.

Colquhoun D and Sakmann B. 1985. Fast events in single-channel currents activated by acetylcholine and its analogues at the frog muscle end-plate. Journal of Physiology 369:501-57.

Cox SL and Macdonald JA. 2001. Temperature Compensation of postsynaptic currents for the extraocular muscle of temperate teleost fishes. Journal of Comparative Physiology A 187:197-203

Ding L, Feng HJ, Macdonald RL, Botzolakis EJ, Hu N, and Gallagher MJ. 2010. $GABA_A$ receptor $\alpha 1$ subunit mutation A322D associated with autosomal dominant juvenile myoclonic epilepsy reduces the expression and alters the composition of wild type $GABA_A$ receptors. Journal of Biological Chemistry 285(34):26390-405.

Dionne VE. 1989. Two types of nicotinic acetylcholine receptor channels at slow fibre end-plates of the garter snake. Journal of Physiology 409:313-31.

Dionne VE and Parsons RL. 1978. Synaptic channel gating differences at snake twitch and slow neuromuscular junctions. Nature 1274(5674):902-4.

Dionne VE and Parsons RL. 1981. Characteristics of the acetylcholine-operated channel at twitch and slow fibre neuromuscular junctions of the garter snake. Journal of Physiology 310:145-58.

Downes GB and Granato M. 2004. Acetylcholinesterase function is dispensible for sensory neurite growth but is critical for neuromuscular synapse stability. Developmental Biology 270: 232-45.

Drapeau P, Buss RR, Ali DW, Legendre P and Rotundo RL. 2001. Limits to the development of fast neuromuscular transmission in zebrafish. Journal of Neurophysiology 86(6):2951-6.

Fatt P and Katz B. 1951. An analysis of the end-plate potential recorded with an intra-cellular electrode. Journal of Physiology 115:320-70.

Fedorov, VV. 1987. Analysis of postsynaptic currents in the phasic and tonic muscle fibers of the extraocular muscles of the rat. Neirofiziologiia 19(1):120-9.

Fedorov VV, Magazanik LG, Snetkov, VA and Zefirov AL. 1982. Postsynaptic currents in different types of frog muscle fibre. Pflugers Archiv: European Journal of Physiology 394: 202-10.

Fernand VS and Hess A. 1969. The occurrence, structure and innervation of slow and twitch muscle fibres in the tensor tympani and stapedius of the cat. Journal of Physiology 200(2):547-54

Fischbach GD and Schuetze SM. 1980. A post-natal decrease in acetylcholine channel open time at rat end-plates. Journal of Physiology 303:125-37.

Floyd K. Small multiple nerve endings in sheep oesphoageal muscle (abstr). 1971. Journal of Physiology 216:37-8P.

Gilly WF and Hui CS. 1980. Mechanical activation in slow and twitch skeletal muscle fibres of the frog. Journal of Physiology 301:137-56.

Golino MD and Hamill OP. 1992. Subunit requirements for Torpedo AChR channel expression: a specific role for the delta-subunit in voltage-dependent gating. Journal of Membrane Biology 129(3):297-309.

Granato M, van Eeden FJ, Schach U, Trowe T, Brand M, Furutani-Seiki M, Haffter P, Hammerschmidt M, Heisengerg CP, Jiang YJ, Kane DA, Keish RN, Mullins MC, Odenthal J and Nusslein-Volhard C. 1996. Genes controlling and mediating locomotion behavior of the zebrafish embryo and larva. Development 123:399-413.

Grosman C and Auerbach A. 2001. The dissociation of acetylcholine from open nicotinic receptor channels. Proceedings of the National Academy of Sciences 98:14102-7.

Gu Y and Hall ZW. 1988. Immunological evidence for a change in subunits of the acetylcholine receptor in developing and denervated rat muscle. Neuron 1(2):117-25.

Haghighi AP and Cooper E. 1998. Neuronal nicotinic acetylcholine receptors are blocked by intracellular spermine in a voltage-dependent manner. Journal of Neuroscience 18(11):4050-62.

Haghighi AP and Cooper E. 2000. A molecular link between inward rectification and calcium permeability of neuronal nicotinic acetylcholine alpha3beta4 and alpha4beta2 receptors. Journal of Neuroscience 20(2):529-41.

Hamill OP and Sakmann B. 1981. Multiple conductance states of single acetylcholine receptor channels in embryonic muscle cells. Nature 294(5840):462-4.

Henderson LP and Brehm P. 1989. The single-channel basis for the slow kinetics of synaptic currents in vertebrate slow muscle fibers. Neuron 2(4):1399-405.

Henderson LP, Lechleiter JD and Brehm P. 1987. Single channel properties of newly synthesized acetylcholine receptors following denervation of mammalian skeletal muscle. Journal of General Physiology 89(6):999-1014.

Hess A. 1960. The structure of extrafusal muscle fibers in the frog and their innervation studied by the cholinesterase technique. American Journal of Anatomy 107:129-51.

Hess A. 1970. Vertebrate slow muscle fibers. Physiological Reveiws 50:40-62.

Hidaka T and Toida N. 1969. Biophysical and mechanical properties of red and white muscle fibres in fish. Journal of Physiology 201(1):49-59.

Hodgkin AL, Huxley AF and Katz B. 1952. Measurement of current-voltage relations in the membrane of the giant axon of loligo. Journal of Physiology 116:424-48.

Huerta M, Muñiz J and Stefani E. 1986. Effects of external calcium on potassium contractures in tonic muscle fibers of the frog (Rana pipiens). Journal of Physiology 376:219-30.

Hume RI, Dingledine R and Heinemann SF. 1991. Identification of a site in glutamate receptor subunits that controls calcium permeability. Science 253(5023):1028-31.

Ibañez-Tallon I, Wen H, Miwa JM, Xing J, Tekinay AB, Ono F, Brehm P and Heintz N. 2004. Tethering naturally occurring peptide toxins for cell-autonomous modulation of ion channels and receptors in vivo. Neuron 43(3):305-11.

Jackson M, Imoto K, Mishina M, Konno T, Numa S and Sakmann B. 1990. Spontaneous and agonist-induced openings of an acetylcholine receptor channel composed of bovine muscle alpha, beta and delta subunits. Pflugers Archiv: European Journal of Physiology 417:129-35.

Jaramillo F, Vicini S and Schuetze SM. 1988. Embryonic acetylcholine receptors guarantee spontaneous contractions in rat developing muscle. Nature 335(6185):66-8.

Jones AK, Elgar G and Sattelle DB. 2003. The nicotinic acetylcholine receptor gene family of the pufferfish, Fugu rubripes. Genomics 82(4):441-51.

Kaminski HJ, Kusner LL, Richmonds C, Medof ME and Lin F. 2006. Deficiency of decay accelerating factor and CD59 leads to crisis in experimental myasthenia. Experimental Neurology 202(2):287-93.

Karlin, A. 2002. Emerging structure of the nicotinic acetylcholine receptors. Nature Reviews Neuroscience 3(2):102-14.

Katz B and Miledi R. 1971. Further observations on acetylcholine noise. Nature New Biology 232:124-6.

Katz B and Miledi R. 1972. The statistical nature of the acetycholine potential and its molecular components. Journal of Physiology 224(3):665-99.

Katz B and Miledi R. 1973. The binding of acetylcholine to receptors and its removal from the synaptic cleft. Journal of Physiology 231(3):549-74.

Khanna S, Richmonds CR, Kaminski HJ and Porter JD. 2003. Molecular organization of the extraocular muscle neuromuscular junction: partial conservation of and divergence from the skeletal muscle prototype. Investigative Ophthalmology & Visual Science 44(5):1918-26.

Kim MJ, Liu IH, Song Y, Lee JA, Halfter W, Balice-Gordon RJ, Linney E and Cole GJ. 2007. Agrin is required for posterior development and motor axon outgrowth and branching in embryonic zebrafish. Glycobiology 17(2):231-47.

Koenen M, Peter C, Villarroel A, Witzemann V and Sakmann B. 2005. Acetylcholine receptor channel subtype directs the innervation pattern of skeletal muscle. EMBO Reports 6(6):570-6.

Kordas M. 1969. The effect of membrane polarization on the time course of the end-plate current in frog sartorius muscle. Journal of Physiology 204(2):493-502.

Korenaga S, Kou K and Ito Y. 1982. Induction of action potentials in fish red muscle by denervation. Proceedings of the Royal Society of London. Series B, Containing papers of a Biological character. 217(1206):89-99.

Krüger P. 1949. Die Innervation der tetanischen und tonischen fasern der quergestreiften skelettmuskulatur der wirbeltiere Anatomischer Anzeiger, 97:169-75.

Kuffler SW and Gerard RW. 1947. The small-nerve motor system to skeletal muscle. Journal of Neurophysiology 10:383-94.

Kuffler SW, Laporte Y and Ramsmeier RE. 1947. The function of the frog's small nerve motor system. Journal of Neurophysiology 10:395-408.

Kuffler SW and Vaughn Williams EM. 1953a. Small-nerve junctional potentials. The distribution of small motor nerves to frog skeletal muscle, and the membrane characteristics of the fibres they innervate. Journal of Physiology 121:289-317.

Kuffler SW and Vaughn Williams EM. 1953b. Properties of the 'slow' skeletal muscle fibres of the frog. Journal of Physiology 121:318-40.

Kullberg RW, Brehm P and Steinbach JH. 1981. Nonjunctional acetylcholine receptor channel open time decreases during development of Xenopus muscle. Nature 289(5796):411-3.

Kullberg RW, Mikelberg FS and Cohen MW. 1980. Contribution of cholinesterase to developmental decreases in the time course of synaptic potentials at an amphibian neuromuscular junction. Developmental Biology 75(2):255-67.

Kullberg R and Owens JL. 1986. Comparative development of end-plate currents in two muscles of Xenopus laevis. Journal of Physiology 374:413-27.

Kullberg RW, Owens JL, Camacho P, Mandel G and Brehm P. 1990. Multiple conductance classes of mouse nicotinic acetylcholine receptors expressed in Xenopus oocytes. Proceedings of the National Academy of Sciences 87(6):2067-71.

Kummer TT, Misgeld T and Sanes JR. 2006. Assembly of the postsynaptic membrane at the neuromuscular junction: paradigm lost. Current Opinion in Neurobiology 16(1):74-82.

Kurosaki T, Fukuda K, Konno T, Mori Y, Tanaka K, Mishina M and Numa S. 1987. Functional properties of nicotinic acetylcholine receptor subunits expressed in various combinations. Federation of European Biochemical Societies Letters 214 (2):253-58.

Ling G and Gerard RW. 1949. The normal membrane potential of frog sartorius fibres. Journal of Cellular and Comparative Physiology 34:383-96.

Liu DW and Westerfield M. 1992. Clustering of muscle acetylcholine receptors requires motoneurons in live embryos, but not in cell culture. Journal of Neuroscience 12(5):1859-66.

Liu Y and Brehm P. 1993. Expression of subunit-omitted mouse nicotinic acetylcholine receptors in Xenopus laevis oocytes. Journal of Physiology 470:349-63.

Luna VM and Brehm P. 2006. An electrically coupled network of skeletal muscle in zebrafish distributes synaptic current. Journal of General Physiology 128 (1): 89-102.

Macdonald JA and Balnave RJ. 1984. Miniature end plate currents from telost extraocular muscle. Journal of Comparative Physiology A 155:649-59

Magleby KL and Stevens CF. 1972a. The effect of voltage on the time course of end-plate currents. Journal of Physiology 223:151-71.

Martinou JC and Merlie JP. 1991. Nerve-dependent modulation of acetylcholine receptor

epsilon-subunit gene expression. Journal of Neuroscience 11(5):1291-9.

Michler A and Sakmann B. 1980. Receptor stability and channel conversion in the subsynaptic membrane of the developing mammalian neuromuscular junction. Devopmental Biology 80(1):1-17.

Miledi R and Stefani E, Steinbach AB. 1971. Induction of the action potential mechanism in slow muscle fibres of the frog. Journal of Physiology 217(3):737-54.

Miledi R and Uchitel OD. 1981. Properties of postsynaptic channels induced by acetylcholine in different frog muscle fibres. Nature 291:162-5.

Mishina M, Takai T, Imoto K, Noda M, Takahashi T, Numa S, Methfessel C and Sakmann B. 1986. Molecular distinction between fetal and adult forms of muscle acetylcholine receptor. Nature 321(6068):406-11.

Missias AC, Chu GC, Klocke BJ, Sanes JR and Merlie JP. 1996. Maturation of the acetylcholine receptor in skeletal muscle: regulation of the AChR gamma-to-epsilon switch. Developmental Biology 179(1):223-38.

Missias AC, Mudd J, Cunningham JM, Steinbach JH, Merlie JP and Sanes JR. 1997. Deficient development and maintenance of postsynaptic specializations in mutant mice lacking an 'adult' acetylcholine receptor subunit. Development 124(24):5075-86.

Morgan DL and Proske U. 1984. Vertebrate slow muscle: Its structure, pattern of innervation, and mechanical properties. Physiological Reviews 64:103-69.

Mos W, Maslam S, van Raamsdonk W, Kilarski W and de Jager S. 1983. Acetylcholinesterase and acetylcholine receptor histochemistry on end plate regions, myotendinous junctions, and sarcolemma in the axial musculature of three teleost fish species. Acta Histochemica 72(1):39-53.

Neher E and Sakmann B. 1976. Single-channel currents recorded from membrane of denervated frog muscle fibres. Nature 260:799-802.

Nguyen PV, Aniksztejn L, Catarsi S and Drapeau P. 1999. Maturation of neuromuscular transmission during early development in zebrafish. Journal of Neurophysiology 81(6):2852-61.

Ogata T. 1988. Structure of motor endplates in the different fiber types of vertebrate skeletal muscles. Archives of Histology and Cytology 51(5):385-424.

Ono F, Higashijima S, Shcherbatko A, Fetcho JR and Brehm P. 2001. Paralytic zebrafish lacking acetylcholine receptors fail to localize rapsyn clusters to the synapse. Journal of Neuroscience 21(15):5439-48.

Ono F, Mandel G and Brehm P. 2004. Acetylcholine receptors direct rapsyn clusters to the neuromuscular synapse in zebrafish. Journal of Neuroscience 24:5475-81.

Ono F, Shcherbatko A, Higashijima S, Mandel G and Brehm P. 2002. The Zebrafish motility mutant twitch once reveals new roles for rapsyn in synaptic function. Journal of Neuroscience 22(15):6491-8.

Oomura Y and Tomita T. 1960. Analysis of the junction potential of a small nerve. Nature 188:416-7.

Owens JL and Kullberg R. 1989a. In vivo development of nicotinic acetylcholine receptor channels in Xenopus myotomal muscle. Journal of Neuroscience 9(3):1018-28.

Owens JL and Kullberg R. 1989b. Three conductance classes of nicotinic acetylcholine receptors are expressed in developing amphibian skeletal muscle. Journal of Neuroscience 9(7):2575-80.

Panzer JA, Gibbs SM, Dosch R, Wagner D, Mullins MC, Granato M and Balice-Gordon RJ. 2005. Neuromuscular synaptogenesis in wild-type and mutant zebrafish. Developmental Biology 285(2):340-57.

Paradiso K and Brehm P. 1998. Long-term desensitization of nicotinic acetylcholine receptors is regulated via protein kinase A-mediated phosphorylation. Journal of Neuroscience 18(22):9227-37.

Rome LC, Funke RP, Alexander RM, Lutz G, Aldridge H, Scott F and Freadman M. 1988. Why animals have different muscle fibre types. Nature 335 (27):824-7.

Ruff RL and Spiegel P. 1990. Ca sensitivity and acetylcholine receptor currents of twitch and tonic snake muscle fibers. American Journal of Physiology 259(6 Pt 1):C911-9.

Sakmann B and Brenner HR. 1978. Change in synaptic channel gating during neuromuscular development. Nature 276:401-2.

Sakmann B, Patlak J and Neher E. 1980. Single acetylcholine-activated channels show burst-kinetics in presence of desensitizing concentrations of agonist. Nature 286(5768):71-3.

Sanger AM and Stoiber W. 2001. Muscle Fiber Diversity and Plasticity. Muscle Development and Growth 18(7):187-250

Scheutze SM, Frank EF and Fischbach GD. 1978. Channel open time and metabolic stability of synaptic and extrasynaptic acetylcholine receptors on cultured chick myotubes. Proceedings of the National Academy of Sciences of the United States of America 75:520-3.

Sepich DS, Wegner J, O'Shea S, and Westerfield M. 1998. An altered intron inhibits synthesis of the acetylcholine receptor alpha-subunit in the paralyzed zebrafish mutant nic1. Genetics 148:361-72.

Siegelbaum SA, Trautman A and Koenig J. 1984. Single acetylcholine-activated channel currents in developing muscle cells. Developmental Biology 104:366-79.

Sigworth FJ and Sine SM. 1987. Data transformations for improved display and fitting of single-channel dwell time histograms. Biophysical Journal 52:1047-54.

Sine SM and Claudio T. 1991. Gamma- and delta-subunits regulate the affinity and the cooperativity of ligand binding to the acetylcholine receptor. Journal of Biological Chemistry 266(29):19369-77.

Sine SM and Steinbach JH. 1984. Activation of a nicotinic acetylcholine receptor. Biophysical Journal 45:175-85.

Sommerkamp H. 1928. Das substrat der dauerverkurzung am froschmuskel. (Physiologische und pharmakologische sonderstellung bestimmer muskelfarsern). Archiv für experimentelle Pathologie und Pharmakologie 128:99-115.

Sullivan MP, Owens JL and Kullberg RW. 1999. Role of M2 domain residues in conductance and gating of acetylcholine receptors in developing Xenopus muscle. Journal of Physiology 515 (Pt 1):31-9.

Sumanas S and Larson JD. 2002. Morpholino phosphorodiamidate oligonucleotides in zebrafish: a recipe for functional genomics? Briefings in Functional Genomics and Proteomics 1(3):239-56.

Takahashi M, Kubo T, Mizoguchi A, Carlson CG, Endo K and Ohnishi K. 2002. Spontaneous muscle action potentials fail to develop without fetal-type acetylcholine receptors. EMBO Reports 3(7):674-81.

Takeuchi A. 1959. Neuromuscular transmission of fish skeletal muscles investigated with intracellular microelectrode. Journal of Cellular and Comparative Physiology 54:211-20.

Takeuchi A and Takeuchi N. 1959. Active phase of frog's end-plate potential. Journal of Neurophysiology 22:395-411.

Takeuchi N and Takeuchi A. 1958. Direct determination of the active phase of endplate potential. Nature 181:779.

Tang R, Dodd A, Lai D, McNabb WC and Love DR. 2007. Validation of zebrafish (Danio rerio) reference genes for quantitative real-time RT-PCR normalization. Acta biochimica et biophysica Sinica 39(5):384-90.

Uchitel, OD and Miledi R. 1987. Characteristics of synaptic currents in frog muscle fibers of different types. Journal of Neuroscience Research 17:189-198.

van Raamsdonk W, Pool CW and Te Kronnie G. 1978. Differentiation of muscle fiber types in the teleost Brachydanio rerio. Anatomy and embryology 153(2):137-55.

van Raamsdonk W, Van't Veer L, Veeken K, Heyting C and Pool CW. 1982. Differentiation of muscle fiber types in the teleost Brachydanio rerio, the zebrafish. Posthatching development. Anatomy and embryology 164(1):51-62.

Wen H and Brehm P. 2005. Paired motor neuron-muscle recordings in zebrafish test the receptor blockade model for shaping synaptic current. Journal of Neuroscience 25(35):8104-11.

Westerfield M, Liu DW, Kimmel CB and Walker C. 1990. Pathfinding and synapse formation in a zebrafish mutant lacking functional acetylcholine receptors. Neuron 4(6):867-74.

White MM, Mayne KM, Lester HA and Davidson N. 1985. Mouse-Torpedo hybrid acetylcholine receptors: functional homology does not equal sequence homology. Proceedings of the National Academy of Sciences of the United States of America 82(14):4852-6.

Witzemann V, Barg B, Nishikawa Y, Sakmann B and Numa S. 1987. Differential regulation of muscle acetylcholine receptor gamma- and epsilon-subunit mRNAs. FEBS Letters 223(1):104-12.

Xie W, Stribley JA, Chatonnet A, Wilder PJ, Rizzino A, McComb RD, Taylor P, Hinrichs SH and Lockridge O. 2000. Postnatal developmental delay and supersensitivity to organophosphate in gene-targeted mice lacking acetylcholinesterase. Journal of Pharmacology and Experimental Therapeutics 293(3):896-902.

Yamamoto T. 1972. Electrical and mechanical properties of the red and white muscles in the silver carp. Journal of Experimental Biology 57(2):551-67.

Yoshii K, Yu L, Mayne KM, Davidson N and Lester HA. 1987. Equilibrium properties of mouse-Torpedo acetylcholine receptor hybrids expressed in Xenopus oocytes. Journal of General Physiology 90(4):553-73.

APPENDIX

The data suggesting that zebrafish AChRs may be sensitive to open channel block by ACh at relatively low concentrations (10 μM) is presented in the figures shown in Appendix 1 and Appendix 2. Comparison of the burst duration of zebrafish AChRs indicated that at 10 μM ACh, the mean burst duration was invariably longer than the burst duration at 300 nM ACh for both reconstituted, and native AChRs (Appendix 1). For this analysis each burst duration histogram was constructed by pooling several recordings and thus the fit represents an overall mean burst duration for the cumulative data. The number of recordings pooled for each histogram is indicated in the corresponding legend. For reconstituted single-channel data, all recordings were taken at -100 mV membrane potential. For on-cell data, all recordings were taken at +50 mV applied potential. For each histogram, the minimum duration was set to 180 μs, and the amplitudes were restricted to the amplitude class of interest (as previously defined). For each histogram, the number of events, fit time constants, and contribution of the time constants are indicated in the text above the graphics. For completion, the closed duration histograms at 10 μM are also shown, although the interpretation of the closed duration is complicated (due to the possibility of open-channel block).

In each case, the single-channel burst duration of reconstituted receptor types was longer at 300 nM than at 10 μM (Appendix 1A-C). The fold change in burst duration was on average 1.4-fold (αβδε 1.2-fold; αβδγ 1.2-fold and 1.7-fold; αβδ 1.6-fold). Although relatively subtle, the reduction of burst duration was consistent across all

receptor types and experiments. The same effect was more apparent on slow muscle AChR duration, where events were 3.7-fold longer at 300 nM ACh than at 10 μM (Appendix 1D). Together, these results precluded my ability to use high concentrations of ACh for analysis of receptor kinetics for reconstituted or native receptor types.

An even more conspicuous effect of ACh on burst duration was seen using 100 μM ACh (Appendix 2). Visual inspection of the αβδγ events indicated that the openings were irregularly shaped, frequently interrupted by closures and remained at the peak amplitude only briefly (Appendix 2A, left). These aspects are consistent with open-channel block. The burst duration histogram was fit with a single exponential that indicated that application of 100 μM ACh dramatically reduced the mean burst duration (Appendix 2A, right). For comparison, sample events recorded using 10 μM and 300 nM ACh are also shown in Appendix 2, alongside their respective burst duration histograms. Overall, the burst duration of the αβδγ receptor was 3.8-fold longer at 300 nM ACh than at 100 μM ACh when estimated using a single exponential fit (1.3 ms vs. 0.34 ms). Furthermore, the obvious effect of 100 μM ACh supported my concern that the single-channel kinetics obtained at 10 μM ACh also may have been influenced by block.

Appendix 1: Kinetic properties of zebrafish AChRs at different ACh concentrations. All fit values are indicated above histograms. A) Single-channel burst duration of the αβδε receptor at 300 nM (n=8 recordings) and 10 μM ACh (n=7 recordings) at -100 mV. B) Single-channel burst duration of the αβδγ receptor at 300 nM (n=10 recordings) and 10 μM ACh (n=9 recordings) at -100 mV. C) Single-channel burst duration of the αβδ receptor at 300 nM (n=6 recordings) and 10 μM ACh (n=7 recordings) at -100 mV. D) Single-channel burst duration of the slow muscle AChR at 300 nM (n=10 recordings) and 10 μM ACh (n=4 recordings) at +50 mV applied potential.

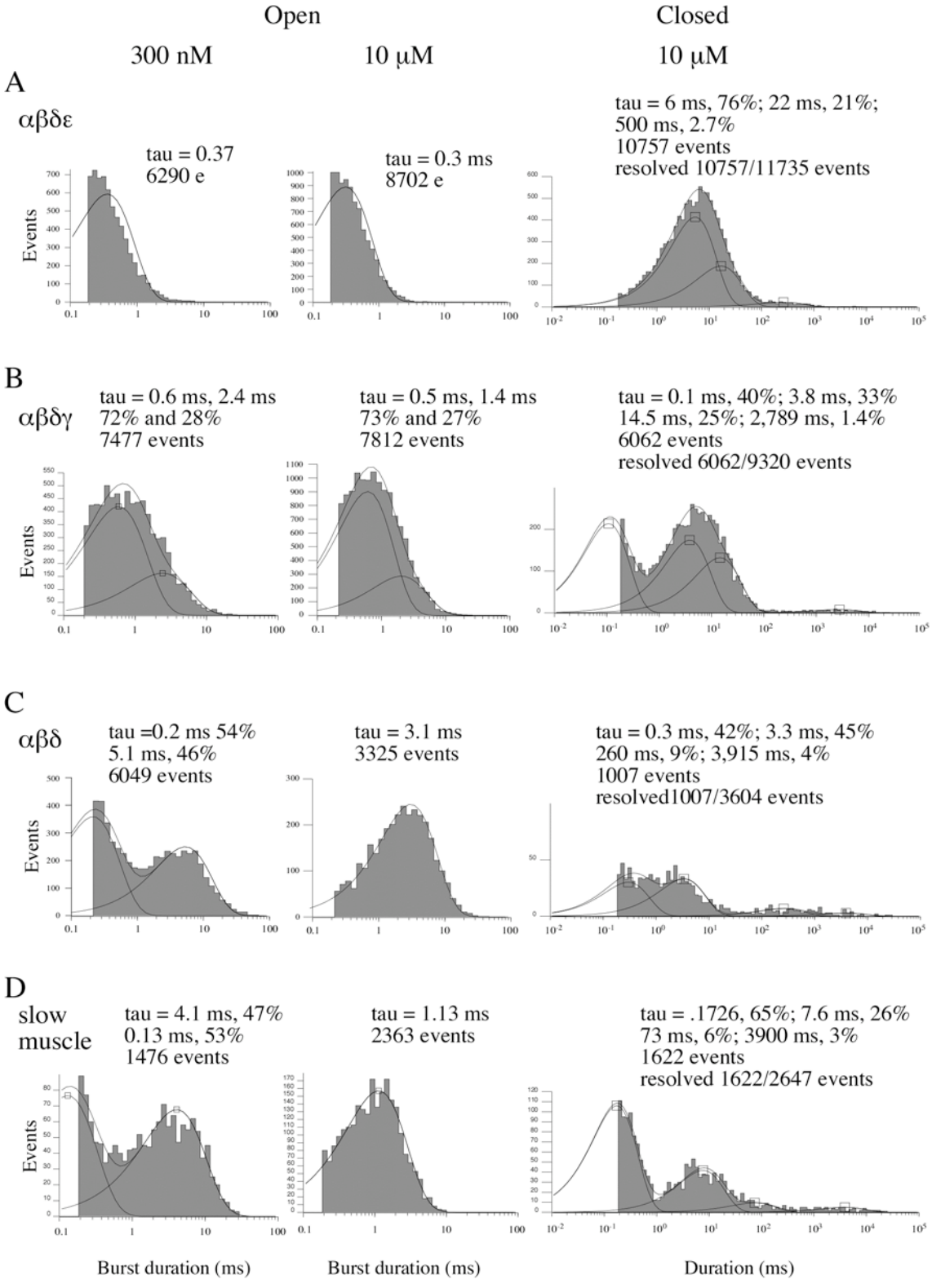
Open
Closed
300 nM
10 μM
10 μM
A
αβδε
tau = 0.37
6290 e
tau = 0.3 ms
8702 e
tau = 6 ms, 76%; 22 ms, 21%;
500 ms, 2.7%
10757 events
resolved 10757/11735 events
Events
B
αβδγ
tau = 0.6 ms, 2.4 ms
72% and 28%
7477 events
tau = 0.5 ms, 1.4 ms
73% and 27%
7812 events
tau = 0.1 ms, 40%; 3.8 ms, 33%
14.5 ms, 25%; 2,789 ms, 1.4%
6062 events
resolved 6062/9320 events
Events
C
αβδ
tau =0.2 ms 54%
5.1 ms, 46%
6049 events
tau = 3.1 ms
3325 events
tau = 0.3 ms, 42%; 3.3 ms, 45%
260 ms, 9%; 3,915 ms, 4%
1007 events
resolved1007/3604 events
Events
D
slow
muscle
tau = 4.1 ms, 47%
0.13 ms, 53%
1476 events
tau = 1.13 ms
2363 events
tau = .1726, 65%; 7.6 ms, 26%
73 ms, 6%; 3900 ms, 3%
1622 events
resolved 1622/2647 events
Events
Burst duration (ms)
Burst duration (ms)
Duration (ms)

Appendix 2: Burst duration of the αβδγ receptor at three concentrations of ACh. The fit values and event count are indicated in text above each histogram, and all recordings were performed at -100 mV. A) Sample single-channel events and burst duration histogram using 100 μM ACh. B) Sample single-channel events and burst duration histogram using 10 μM ACh. C) Sample single-channel events and burst duration histogram using 300 nM ACh.

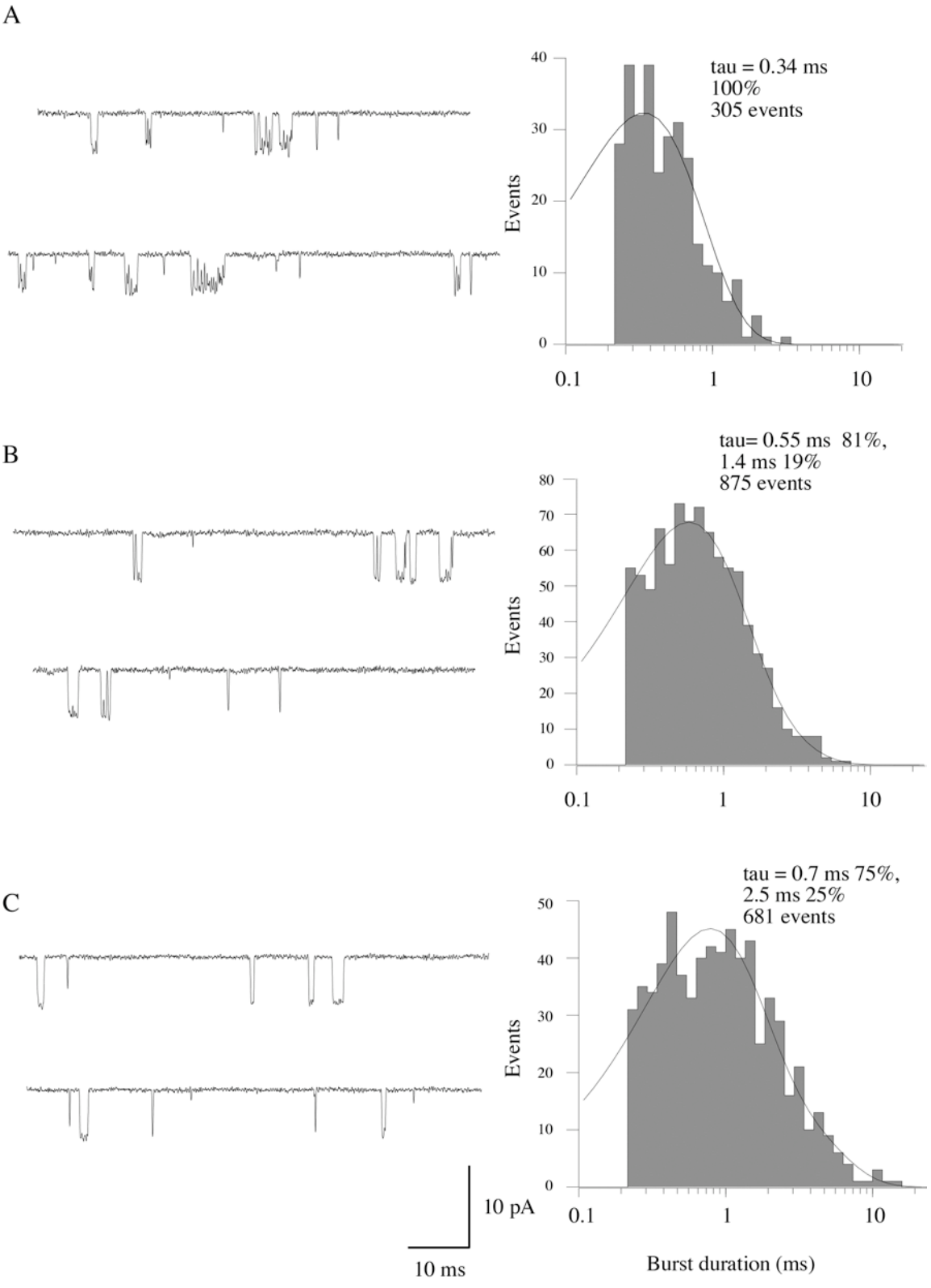
A
tau = 0.34 ms
100%
305 events
Events
40
30
20
10
0
0.1
1
10
B
tau= 0.55 ms 81%,
1.4 ms 19%
875 events
Events
80
70
60
50
40
30
20
10
0
0.1
1
10
C
tau = 0.7 ms 75%,
2.5 ms 25%
681 events
Events
50
40
30
20
10
0
0.1
1
10
10 pA
10 ms
Burst duration (ms)